RENAN PIRES LORETO

TOPOLOGICAL STATES APPLIED TO SPINTRONICS DEVICES

Thesis presented at the *Universidade Federal de Viçosa* in partial fulfillment of the requirements of the doctoral physics program for the degree of *Doctor Scientiae*.

VIÇOSA
MINAS GERAIS – BRAZIL
2018

Ficha catalográfica preparada pela Biblioteca Central da Universidade Federal de Viçosa - Câmpus Viçosa

T
L869t
2018

Loreto, Renan Pires, 1989-
Topological states applied to spintronics devices / Renan Pires Loreto. – Viçosa, MG, 2018.
x, 134 f. : il. (algumas color.) ; 29 cm.

Texto em inglês.
Orientador: Clodoaldo Irineu Levartoski de Araujo.
Tese (doutorado) - Universidade Federal de Viçosa.
Referências bibliográficas: f. 120-134.

1. Spintrônicos. 2. Nanotecnologia. 3. Magnetismo. 4. Topologia. I. Universidade Federal de Viçosa. Departamento de Física. Programa de Pós-Graduação em Física. II. Título.

CDD 22. ed. 539.725

RENAN PIRES LORETO

TOPOLOGICAL STATES APPLIED TO SPINTRONICS DEVICES

Thesis presented at the *Universidade Federal de Viçosa* in partial fulfillment of the requirements of the doctoral physics program for the degree of *Doctor Scientiae*.

APPROVED: April 24^{th}, 2018.

Antônio Ribeiro de Moura

João Paulo Sinnecker

Leandro Gutierrez Rizzi

Luiz Carlos Sampaio Lima

Clodoaldo Irineu Levartoski de Araújo
(Adviser)

Acknowledgments

First of all, I want to apologize in advance if i forget the name of someone here, don't take it personal...

I would like to thank...

- Clodoaldo for all this years of support, by teaching me almost everything I know today, for the trust and faith in me and in my capabilities. And for giving me more work than I thought I could tolerate;

- Dr. Moodera, for one of the most intense years of knowledge i've ever had, and for the opportunity to work in a place like MIT. I would like to thank also Cui-zu, Peng, Yota, Juan, Atilgan, and all postdocs at MIT for the patience with me;

- my mother, for hear me complaining about something everyday and always hearing me with patience. To my father, for all (specially financial) support in this years in Viçosa and also during my undergrad. And to my family who I can always count with;

- Rafael (according to our agreement made in 2008 to thank each other) to... something ;

- the "meia bomba" friends I made in Boston, Ana, Sarah, Felipe and Fabio who made one of the most difficult years of my life much easier, i love you all;

- all the friends I made in Viçosa, specially the ones that put up with me in the grad student's room;

  To the ones that are not with us anymore like Zé for sharing low quality memes with me, to Luana for judging me all the time, to Ana Paula for having someone to complain about life;

  the ones that are still here...like Carlos and Sylvestre for all stories we had in this city (most of them based in alcohol), to Cesar for all the incomprehensible talks we had on our way to lunch and coffee time, to Cacilhas for teaching me the 'don't worry' phylosophy (a.k.a. *Cacilhism*), to Leandro for all... (wait, i'm thinking), to the other PhD students

in our group (Hamilton, Oscar, Teonis, João, Carol, Igor, etc) and for the others in the student's room;

to the ones outside physics department like Elisson, who chose to be an engineer (poor guy), Lucas who I had the pleasure to teach in high school and now is a friend, and for everyone i've ever ran up with someday (or some night...);

- the friends I left behind in Belo Horizonte who understood (mostly doesn't) my choice to move to Viçosa and achieve this moment. Special thank to Fred, Raissa, Barroca, Marcos Tadeu, Peixe, Roger, Rick...
- I would also like to acknowledge all professors and employees of the Physics Department of Univerisdade Federal de Viçosa for all the knowledge I got in all this years;
- and to Capes and CNPq for the scholarship and also Fapemig for the laboratory financial support.

Thanks for all your encouragement!

Contents

Abstract

LORETO, Renan Pires, D.Sc., Universidade Federal de Viçosa, April, 2018. **Topological states applied to spintronics devices**. Adviser: Clodoaldo Irineu Levartoski de Araújo.

In this work we study three important magnetic systems extensively researched in the past decades. In the first part, the recent proposition of the use of magnetic skyrmions, which are topological particle-like excitations in ferromagnets, in racetrack memories, have attracted a lot of attention recently opening up a new field of study called skyrmionics which is an attempt to use those magnetic structures as information carriers in next generation of spintronic devices. For usage of magnetic skyrmions, in some systems is necessary to include the Dzyaloshinskii-Moriya interaction (DMI) and the out-of-plane magnetic field into the system. In this work, we explore a system without these requirements. First, we propose a controlled way for the creation of magnetic skyrmions and skyrmioniums imprinted in a perpendicular magnetized ferromagnetic nanotrack. Then we investigate the detachment of the imprinted spin textures from the underneath of the nanodisk, the transport by the spin-transfer torque imposed by spin-polarized current pulses applied in the nanotrack and the detection by Tunnel Magnetoresistance (TMR). We notice that the moving structure is not a skyrmion after is detached, and by calculating how the topological charge behaves, we have called it the resonant magnetic soliton (RMS).
The second part covers the generation of spin currents by Spin Pumping and Spin Seebeck effects and the conversion of this spin current to charge current in $(Bi_{0.22}Sb_{0.78})_2Te_3$ topological insulators at room temperature. The spin-to-charge current conversion is attributed to the inverse Edelstein effect (IEE) made possible by the spin-momentum locking in the electron Fermi contours due to the Rashba field. The measurements by the two techniques yield the same value for the IEE parameter, showing that those methods can be an efficient way to the spin to charge current in topological insulators.
In the third part, arrays of nanomagnets designed to resemble spin ice materials (disordered magnetic states) are known as artificial spin ices (ASI). Here we study, both theoretically and experimentally the thermodynamic effects on streched arrays of spin ices. The rectangular artificial spin ices (RASI) is expected do show different phase transitions by changing the geometry

of the system. This geometrically driven dynamics in ASI can open up the panorama of exploring distinct ground states and thermally generated magnetic monopole excitations. Here, it is shown that a particular RASI lattice experience less restriction to flip precisely in a kind of rhombic lattice and by comparing the impact of thermal effects on the spin flips in these three appropriate different RASI arrays, it is possible to find the phenomenon that we call ASI geometrothermodynamics.

Resumo

LORETO, Renan Pires, D.Sc., Universidade Federal de Viçosa, Abril de 2018. **Estados Topológicos aplicados a dispositivos spintrônicos**. Orientador: Clodoaldo Irineu Levartoski de Araújo.

Neste trabalho estudamos tres importantes sisstemas magnéticos extensamente pesquisados nas últimas décadas. Na primeira parte, a proposta recente da utilização de skyrmions magnéticos, que são excitações topológicas tipo quasi-partícula em ferromagnetos, em memórias tipo racetrack, tem atraído a atenção de pesquisadores nos últimos anos abrind um novo campo de estudo chamado *skyrmionics*, que é uma tentativa de utilizar estas estruuras magnéticas como transportadores de informação na próxima geração de de dispositivos spintrônicos. Para a utilização de skyrmions magnéticos, em alguns sistemas é necessário a inclusão de interação Dzyaloshinskii-Moriya e campos magnéticos externos no sistema. Neste trabalho, nós exploramos um sistema sem estes requisitos. Primeiro, propusemos um modo controlado de criação de skyrmions e *skyrmioniums* impressos em em uma nanofita de material ferromagnético com magnetização fora do plano. Após isso, investigamos o destacamento da estrutura da região abaixo de um nanodisco, responsável por imprimir esta estrutura. O transporte é feito por *spin transfer torque* devido a pulsos de corrente elétrica spin polarizada aplicadas na nanofita. A detecção da estrutura é feita por magnetoresistência túnel. Esta estrutura que se move, após deixar a região abaixo do disco, não é mais considerada um skyrmion e, calculando como a carga topológica evolui, a estrutura foi chamada de sóliton magnético ressonante. A segunda parte cobre os efeitos de geração de correntes puras de spin por *Spin Pumping* e efeito Seebeck de Spin e a conversão dessas correntes de spin em correntes de carga em isolantes topológicos a temperatura ambiente. A conversão de corrente de spin em corrente de carga é devido ao efeito Edelstein Inverso (IEE) que é possivel devido ao *'spin-momentum locking'* do elétron no nível de Fermi devido ao campo de Rashba. As medidas nas duas técnicas levaram ao mesmo valor do parâmetro IEE, mostrando que ambos os resultados são maneiras eficientes de converão de corrente de spin em corrente de carga. Na terceira parte, redes de nanomagnetos projetados para assemelhar-se a gelos de spin (estados magnéticos desordenados) e são conhecidos como gelos de spin artificiais e, estudos teóricos e experimentais da termodinâmica nestas redes. Nas re-

des retangulares de gelos de spin artificiais espera-se que mostrem diferentes transições de fase mudando a geometria do sistema. Esta dinâmica gerada por efeitos geométricos abrem uma possibilidade de explorar diferentes estados fundamentais e geração de monopolos magnéticos por efeitos térmicos. Aqui, mostramos que uma rede particular de gelos de spin artificiais se mostram com menos restrições para que as nanoilhas mudem magnetização em uma rede em particular e, comparndo o impacto de efeitos térmicos em mudanças de magnetização em diferentes sistemas, é possível encontrar o fenÃť meno chamado geometrotermodinâmica.

Publications

PUBLICATIONS RELATED TO THIS WORK:

R. P. Loreto, W. A. Moura-Melo, A. R. Pereira, X. Zhang, Y. Zhou. M. Ezawa, C. I. L. de Araujo. *Creation, transport and detection of imprinted magnetic solitons stabilized by spin-polarized current*. Journal of Magnetism and Magnetic Materials **455**, 25-31, 2018. in "Magnetic skyrmions as future information carriers" special issue.

J. B. S. Mendes, O. Alves Santos, J. Holanda, R. P. Loreto, C. I. L. de Araujo, Cui-Zu Chang, J. S. Moodera, A. Azevedo, and S. M. Rezende. *Dirac-surface-state-dominated spin to charge current conversion in the topological insulator* $(\mathrm{Bi}_{0.22}\mathrm{Sb}_{0.78})_2\mathrm{Te}_3$ *films at room temperature*. Physical Review B **96**, 180415(R), 2017.

SUBMITTED PAPERS:

R. P. Loreto, F.S. Nascimento, J. Borme, J. C. Cezar, C. Nisoli, A. R. Pereira, C.I.L. de Araujo. *Geometrothermodynamics in planar artificial spin ices*. arXiv:1710.03058.

1 - Introduction

Since its discovery, magnetism have been applied in our daily life and nowadays many devices are based on it, for example the magnetic storage in hard disk drives (HDD) that increases every year the amount of information that can be stored. The search for even smaller devices, with more processing and storage capacity is the main incentive for researches in new materials, effects and devices around the world

In the past decades, condensed matter physics became one of the most intensely researched and promising fields of study, with the possibility of control the fabrication of micro and nano-sized structures and also the study of its properties.

The most outstanding discoveries over the past years, that opened many doors to new researches that led to faster, smaller, and cheaper devices we use today, include the development of spin valves (SV) [1], the discovery of Giant Magnetoresistance (GMR) [2, 3] in 1988 and in large Tunnel magnetoresistance at room temperature in 1993 [4]. Those effects brought a huge boost in the development of spintronics and data storage devices, starting in 1997 when IBM released the first reading head based on the GMR effect and this quickly became the standard technology for hard disks used in almost all devices. The biggest improvement of magnetoresistance effect came from the magnetic tunnel junction, that increased the storage capacity by allowing more information to be stored in smaller area of a HDD.

From those past discoveries, recent significant researches in spintronics field include Magnetoresistive Random Access Memory (MRAM) that offers large capability, nanosecond switching speed and storage power compared to other types of silicon based solid-state memory such as SRAM and DRAM, and having the advantage of being non volatile [5, 6].

Slonczewski [7] and Berger [8] in 1996 suggested that the magnetization in a layered structure can also be manipulated by the electrical current. Their theory led to great research interest in the spin-transfer (ST) phenomena, where the magnetization can be manipulated without magnetic fields. The study of ST has become a very attractive field [9–12] due to its huge potential to high density memory structures once in such technology it is not necessary the presence of bit lines to generate magnetic fields, as in MRAMs.

In the past years, topology is becoming more present in condensed matter physics. By definition, topology is a mathematical concept that deals with properties of spaces that are invariant under smooth continuous deformations [13]. The history of topology starts with Leonhard Euler and his topological solution to the Königsberg bridge puzzle, in which he proved that crossing all seven bridges of the town requires you to cross at least one bridge twice, and he did it by reducing the problem knowing just the number of land masses and the number of bridges, the topological invariants. The solution would be the same for any city with the same number of land masses and bridges, they are topologically equivalent [14]. Topology leads to the classification of spaces into different families, for example, a cube and a sphere belongs to the same family because they can be transformed into each other, so they are topologically equivalent; a doughnut (torus shape) is not, because the creation of the hole on it is not allowed. Instead, it belongs to a different topological family along with mugs, for example, as one can be smoothly transformed into an another [15]. The same can be thought for the Hamiltonian that describe the band theory of solids, where exists a band gap between ground and excited states, the deformation of this gap can be done smoothly by changing the Hamiltonian where the gap is not destroyed. In topological states of matter, the states can be defined with certain quantities that are topologically invariant [16].

The first topologically nontrivial state of matter, the quantum Hall effect (see chapter 10), was reported in 1980, with Klaus von Klitzing winning the 1985 Nobel Prize in Physics for its experimental observation. These topologically nontrivial materials are characterized by the existence of topologically protected points or nodes where the valence and conduction bands touch at the Fermi energy, enabling the existence of excitations that behave as fermions with unique properties [15].

In magnetism, topological numbers are attributed to structures that can not be that changed by a continuous deformation of the field configuration, leading to excitations that can be stabilized in chiral magnets, like vortex, antivortex or skyrmions. They exhibit a variety of unique topological phenomena, which can be described by the emergent electromagnetic field (EEMF) associated with the spin configuration [17, 18].

Materials presenting some of the properties described above are know as quantum materials including superconductors, graphene, topological insulators, Weyl semimetals, spin ices, nanomagnets, multiferroics and others [19]. This new generation of materials lies in “basically” two pillars: the first are electronic correlations, that are cooperative behaviours not being predicted by the properties of individual electrons, like emergent excitations such as monopoles and skyrmions, and the second is the topological order which include dissipationless transport and

emergent particles with fractional charge [20]. This thesis focus on the outcome of three novel topological states in magnetics systems researched over the past decade and it is organized as follows.

In the Part I we propose an alternative to the racetrack memory devices, first proposed by Stuart Parkin [21] with the information being carried by Domain Walls (DW) and later proposed by Albert Fert [22] using magnetic skyrmions as the information carrier. By a simplified device without Dzyaloshinskii-Moriya interaction and external fields, we show that by using a magnetic soliton stabilized by electrical current (spin-transfer torque), the device construction turned out to be simpler than the others proposed so far and the information can be carried faster, mainly if compared with in plane domain walls and with more stability compared to the out of plane walls.

In the Part II we report the spin to charge current in topological insulators by two methods, the spin pumping and spin Seebeck effects. Quantum Hall insulators, also known as topological insulators constitute a novel state of matter, which have been the subject of intensive investigations in condensed matter physics, specially in the last decade for spintronic applications [23–28].

In the Part III we explore the thermal effects on frustrated systems, called 'spin ices', a set of magnetic nanoislands that, among other things can emerge topological magnetic charges [29] between its vertices due to magnetic frustration, leading to investigation of possible circuits based in *magnetricity*, an analogue of electricity. In this part we explore the experimental and theoretical thermodynamics of those systems realizing geometry dependent phase transitions.

2 - Basic Concepts of Magnetism

Any material, when submited to an external magnetic field, acquires a magnetic moment. This magnetic dipole moment per unit of volume is defined by the magnetization $\vec{M}$. The response of the magnetization to the external field $\vec{H}$ is given by [30]:

$$\vec{M} = \chi \vec{H} \tag{2.1}$$

with χ defined as the magnetic susceptibility.

By applying a field in a material, its response will be defined by the magnetic induction vector $\vec{B}$ inside the material. The Maxwell equations are usually described in terms of this induction vector.

$$\vec{B} = \mu_0(\vec{H} + \vec{M}) \tag{2.2}$$

where μ_0 is the magnetic permeability in vacuum. For a given material, the permeability is defined:

$$\mu = \mu_0(1 + \chi) \tag{2.3}$$

A material can be classified as **paramagnetic** if $\chi > 0$ and **diamagnetic** for $\chi < 0$. Some materials does not have a linear relation between $\vec{H}$ and $\vec{M}$, called materials with collective magnetism (ferromagnetic, ferrimagnetics and antiferromagnetics). This is caused by the strong interaction between consecutive individual magnetic moments, rather than just the interaction between the magnetic moment and the external field.

Diamagnetism is present in all materials, but is relevant only in the absence of paramagnetism or the collective magnetism. Diamagnetic materials are characterized for a small, negative susceptibility and temperature-independent, this means the magnetization induced by an external field is proportional and opposite to the applied field. The magnetic flux variation inside the material generates an induced electromotive force that, according to the Lenz's law acts in order to eliminate the changes in the flux.

Paramagnetism occurs from the alignment of some unpaired magnetic moments with the magnetic field, causing a small increase in the induction field of the material. This induced magnetization is proportional and parallel to the applied field and have a certain temperature-dependence. These materials are characterized for a positive susceptibility and constant, for small fields.

The materials with collective magnetism do not have a direct relation between $\vec{H}$ and $\vec{M}$, where even for zero field, it is possible to observe a remanent magnetization (M_r). The ferromagnetic state is the most common and important collective magnetism. For a strong enough magnetic field, when all magnetic moments are aligned, the material reaches the maximum magnetization, where, even increasing the field, the magnetization can't be increased anymore, this maximum value is called the saturation magnetization (M_s). The magnetization changes direction for a certain strength of magnetic field where, in some points, the magnetization and field can be opposite, for values smaller than the coercive field H_c. Figure 2.1 shows the behaviour of the magnetization in the presence of a magnetic field. This curve is obtained by applying a magnetic field bigger than H_c in order to align all magnetic moments, where magnetization is at maximum. The field is then decreased to zero, where the curve shows the remanent magnetization, that can be different of zero. The field changes direction and reaches maximum at the opposite direction, returning to the initial point, completing the hysteresis cycle. For materials with collective magnetism the spontaneous magnetization of a ferromagnet is observed to vanish above an ordering temperature called the Curie temperature T_c, because thermal energy given to the system is large enough to overcome the mutual relations of the magnetic moments. This temperature phenomena was first explained by Pierre Weiss in 1907, assuming the presence of a "molecular field" inside the ferromagnetic material that tends to align the magnetic moments against thermal fluctuations. The Curie-Weiss Law, that explains the temperature dependence, is plotted in Figure 2.2 [31].

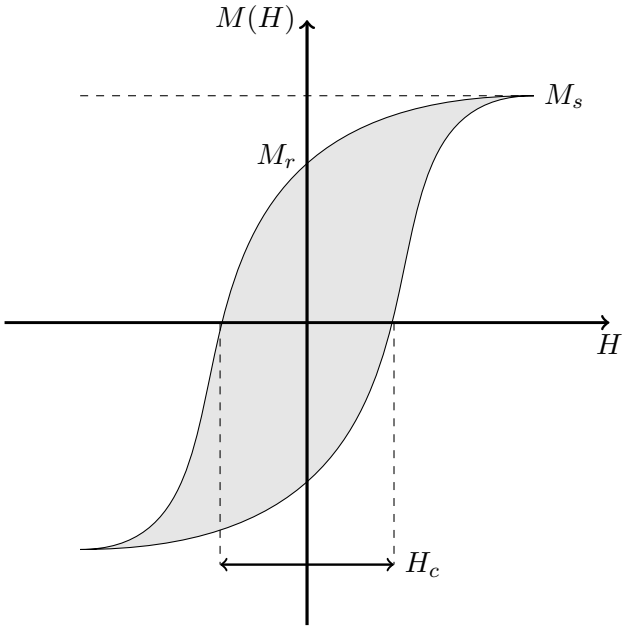

Figure 2.1: Schematic of a hysteresis curve with the saturation magnetization M_s, the remanent magnetization M_r and coercive field H_c.

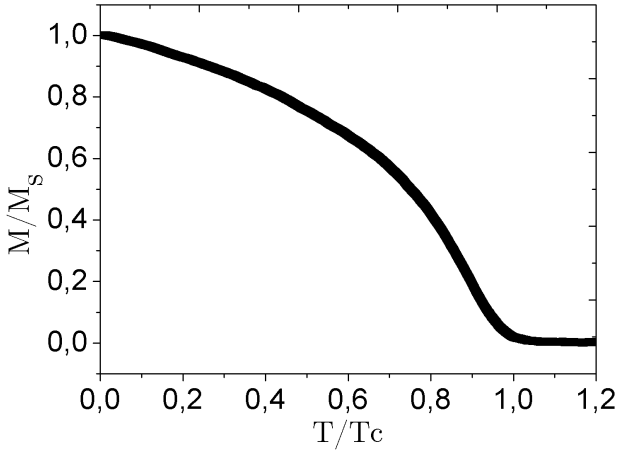

Figure 2.2: Normalized magnetization in function of temperature, normalized to the Curie temperature.

In some special compounds, like αFe_2O_4 (α being Ni, Co, Fe, Mn or Zn), there are two contributions for the total magnetization, with two ferromagnetic sublattices opposite to each other. Those are called ferrimagnetics if the sum of the magnetization of those sublattices are different of zero, below T_c. In a particular case, where the sublattices magnetization cancel each other below a critical temperature, the material is called antiferromagnetic.

2.1 The Exchange Interaction

In contratst to paramagnetic materials, which magnetic moments interact only with external fields, the electronic spins from ferromagnetic materials interact with each other and tends to align its neighbours in their direction. In a ferromagnetic material, the alignment of the magnetic moments in respect to its residual spin is governed by the exchange interaction, described with the Heisenberg Hamiltonian [32],

$$\mathcal{H} = -\sum_{i \neq j} J_{ij} \vec{S_i} \cdot \vec{S_j} \tag{2.4}$$

or using more complex equations capable to taking account of anisotropy effects. In Equation 2.4, J_{ij} is the exchange integral that represents the superposition of the electrons eigenfunctions (a good deduction of the exchange integral can be found in [33, 34]) and $\vec{S_i}$, $\vec{S_j}$ are two neighbour spins. Note that, if $J_{ij} > 0$, the lower energy alignment is ferromagnetic while $J_{ij} < 0$ indicates antiferromagnetic alignment. Heisenberg model is valid for small distances and finite temperatures, different from zero [35].

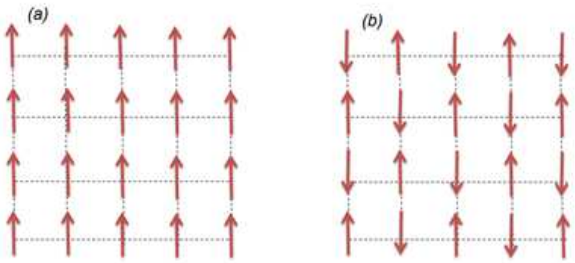

Figure 2.3: a. Ferromagnetic alignment **b.** Antiferromagnetic alignment

The Heisenberg direct exchange is an isotropic relation and can have anisotropy terms depending on the system considered, then the (Equation 2.4) becomes.

$$\mathcal{H} = -\sum_{i \neq j} J_{ij} (\vec{S_i} \cdot \vec{S_j} - \lambda \vec{S_i^z} \cdot \vec{S_j^z}) \tag{2.5}$$

where λ is an anisotropic constant. If λ is zero, Equation 2.5 returns to the isotropic system. If it assume values between 0 and 1, the model have an easy plane anisotropy and in case of negative λ, the system is in the easy axis anisotropy regime, where the z axis is the easy one.

2.2 The Dzyaloshinskii-Moriya Interaction

In 1958, Igor Dzyaloshinskii [36] introduced an antisymmetric term in the exchange interaction when studying a model for weak ferromagnetism. Toru Moriya em 1960 [37] found an explanation for the mechanism under this interaction based on the spin-orbit coupling. The Hamiltonian for the Dzyaloshinskii-Moriya interaction (DMI) is written:

$$\mathcal{H}_{dm} = -\vec{D_{ij}} \cdot (\vec{S_i} \times \vec{S_j}) \tag{2.6}$$

where $\vec{D_{ij}}$ is the Dzyaloshinskii vector (a good deduction of the DM hamiltonian can be found in [33, 38, 39]).

While the direct exchange interaction benefits the parallel or antiparallel alignment between spins, the DM interaction occurs when an inversion symmetry breaking is present. The competition between the exchange and DM interaction leads to a minimal energy state that favours non-collinear spin ordering resulting in chiral configurations, like spirals, where neighbouring spins are always slightly turned. This configurations depends of the direction of the $\vec{D_{ij}}$ vector and it is the main cause of the formation of magnetic skyrmions.

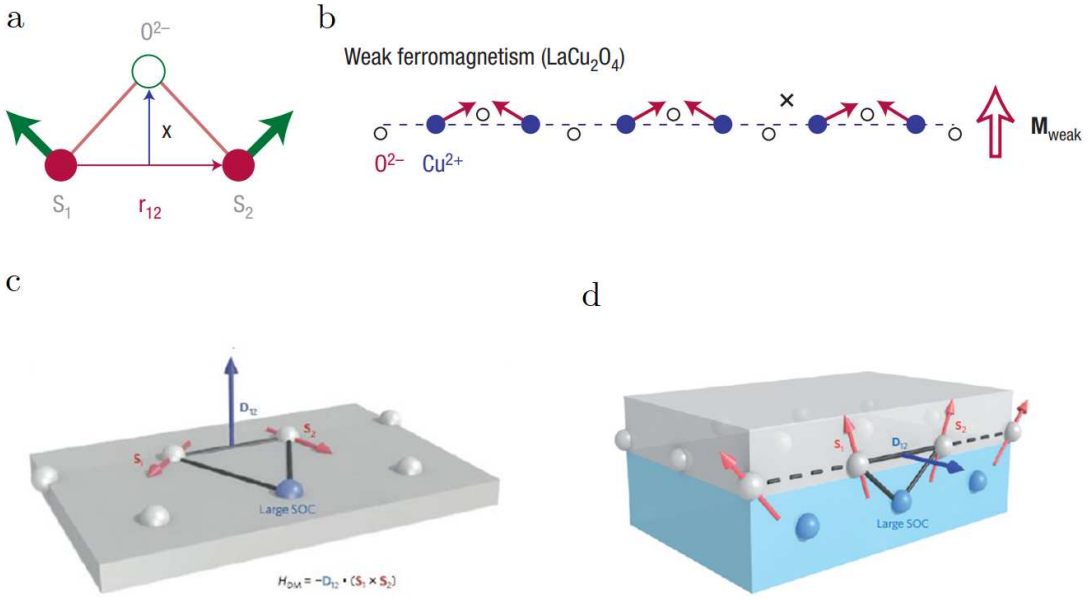

Figure 2.4: a. Symmetry breaking scheme and **b.** rotation of neighbouring spins due to the symmetry breakig in $LaCu_2O_4$. Extracted from [40]. **c.** Schematic of a DMI for a triangle composed of two atomic spins and an atom with a strong SOC. **d.** Scheme of a DMI at the interface between a strong SOC material (blue) and ferromagnetic metal (grey). The vector $\vec{D_{ij}}$ is perpendicular to the plane of the triangle. Extracted from [22]

Figure 2.4a shows the invesion symmetry breaking in $LaCu_2O_4$ [40]. The $\vec{D_{ij}}$ vector is

proportional to $x\hat{x} \times \vec{r}_{ij}$, for $\vec{r}_{ij}$ the vector connecting two neighbours spins and $x\hat{x}$ is the displacement of the Oxygen ion from this line. The energy of the DMI increases with increasing x, that represents the degree of the inversion symmetry breaking. The product $\vec{S_i} \times \vec{S_j}$ pushes the oxygen ion in a direction perpendicular to the chain formed by positive Cu ions (Figure 2.4b).

2.3 Magnetic Anisotropy

When a property of a material is dependent of shape or any specific direction, this material is called anisotropic. In magnetic materials, this anisotropy can be associated to shape, crystalline structure, changes in the lattice parameters and others. This means that the energy required to align the magnetic moments of a ferromagnet crystal depends on the direction of the applied field relative to the crystal axis [41].

Shape anisotropy is dependent of the aspect of the sample. Defining an anisotropic field $H_{anis} = M\Delta N$, for N a demagnetization tensor that depends on the shape of the sample. For example, in a needle, the easy magnetization is favoured along the needle long axis and in a thin film (bi dimensional geometry), this anisotropic field favours the magnetization in the plane of the sample.

One of the most common present kinds of anisotropy is the magnetocrystalline, mainly due to spin-orbit interaction. In this case, the exchange interaction is affected and "easy axis" of magnetization appear. For some materials the magnetocrystalline energy is small compared to the exchange energy, affecting only the direction of the magnetization, not the value, since the exchange model is isotropic.

For example, in a body-centred cubic structure of Iron, there is a higher density of atoms in the [111] direction, making this the hard axis. Magnetization curves below show that the saturation magnetization in [100] direction requires significantly lower field than in the [111], as shown in Figure 2.5.

For hexagonal close-packed (hcp) Co, the [0001] (perpendicular to the close-packed plane) is the easy axis. The [1000] is the close-packed direction and it corresponds to the hard axis.

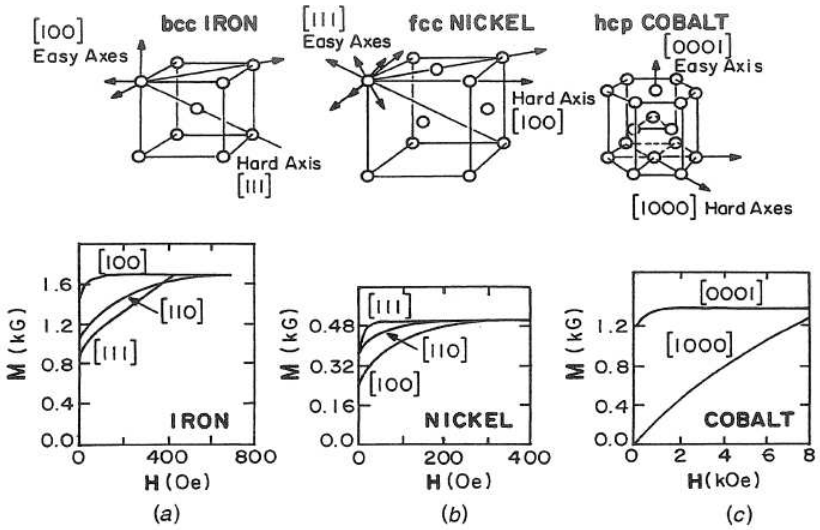

Figure 2.5: Crystalline structure of **a** Iron (body-centred cubic) and **b** Nickel (face-centred cubic) and **c** Cobalt (hexagonal), describing the easy and hard magnetization axes according to their structures and the respective magnetization curve for each crystal axis. Extracted from [30].

A measure for the intensity of the magnetocrystalline anisotropy (or another source of anisotropy) can be done from the field needed to completely saturate all dipole moments of a material (H_{ani}, in this case). The energy density to saturate a sample with anisotropy is:

$$u = \mu_0 \int_0^{M_s} \vec{H}(\vec{M}) d\vec{M} \quad \xrightarrow{\text{1st order approx.}} \quad \frac{\mu_0}{2} M_s H_{anis} \tag{2.7}$$

and can be expanded in a power series [30]

$$u = \sum_n K_{un}\, sin^{2n}\theta \;=\; K_{u0} + K_{u1}\, sin^2\theta + K_{u2}\, sin^4\theta \,+\, ... \tag{2.8}$$

where θ is the angle between $\vec{M}$ and $\vec{B}$. K_{u0} is an isotropic term, since it does not depend on the angle and can be neglected. The first order anisotropy constant K_{u1} defines if the material have easy ($K_{u1} > 0$) or hard ($K_{u1} < 0$) axis magnetization.

If the energy u is the Zeeman energy by volume, ($-\mu_0 \vec{M} \cdot \vec{H} = -\mu_0 M_s H sin\theta$), for a magnetized material immersed in a magnetic field, and using a zero-torque condition on Equation 2.8 to describe the hard-axis magnetization ($-\partial u/\partial\theta = 0$):

$$2K_{u1}\, sin\theta\, cos\theta + 2K_{u2}\, sin^3\theta\, cos\theta \;=\; M_s H\, cos\theta \tag{2.9}$$

In the saturation, we can write $\vec{m} = \vec{M}/M_s = sen\theta$, the magnetization parallel to the magnetic field, Equation 2.9 can be written as:

$$\vec{M} \cdot \vec{H} \;=\; 2K_{u1}\,\vec{m} + 2K_{u2}\,\vec{m}^{3} \tag{2.10}$$

by dividing both sides of Equation 2.9 by $cos\theta$ (since below saturation, $cos\theta > 0$). Equation 2.10 describes the magnetization with a high order term and a second order K_{u2}, usually smaller than K_{u1}

Considering all anisotropies present in a system and the exchange interaction, the description of the energy density for an applied magnetic field perpendicular to the easy axis is written [30]:

$$f = K_u\, cos^2\theta \;- M_s H\, cos\theta\;, \qquad for\;\; K_u > 0 \tag{2.11}$$

This energy is minimized if the first derivative is zero and the second derivative is bigger than zero.

$$(-2K_u\, cos\theta \;+ M_s H)\; sen\theta = 0 \tag{2.12}$$

$$-\,K_u\, cos^2\theta \;+ M_s H\, cos\theta \;> 0 \tag{2.13}$$

The condition 2.12 is for zero torque of $\vec{M}$, when the magnetization is stable and aligned to the magnetic field and have two solutions. First when $sin\theta = 0$, leading to $\theta = 0, \pi, ...$ which indicates a saturated state or when

$$2K_u\, cos\theta \;= M_s H \tag{2.14}$$

For an external applied field large enough to saturate all moments of a given sample, the field is the coercive field $H = H_c$ and $cos\theta = 1$, K_u can be defined:

$$K_u = \frac{M_s H_s}{2} \tag{2.15}$$

In multilayer structure, the physical origin of the perpendicular magnetic anisotropy energy is the interaction of the mean exchange field and the orbital angular momenta of the atoms (ions) in the lattice. This interaction is referred to as spin-orbit coupling. For example, in a usual (Platinum or Palladium)/Cobalt bilayer structure, the out of plane anisotropy is due to the strong spin-orbit interaction from the heavy metal to the magnetic material [42]. For Co layers, having a hcp structure, magnetocrystalline anisotropy can be considerable. The effective anisotropy constant is given by a volumetric K_v and a interfacial K_s contribution for an effective anisotropy constant, written as

$$K_{ef} = K_v + \frac{2K_s}{t}, \quad fort \neq 0 \tag{2.16}$$

plotted in Figure 2.6. The perpendicular magnetic anisotropy (PMA) is a result of a magnetic anisotropy at the interface which considerably differs from the magnetic anisotropy in the bulk. For those materials, the perpendicular anisotropy vanishes for Cobalt thickness more than 13Å. The strong demagnetizing fields which are created by the spin-orbit when turning the magnetization out of the film plane is bigger than the effect responsible for the orientation of the magnetization parallel to the film plane.

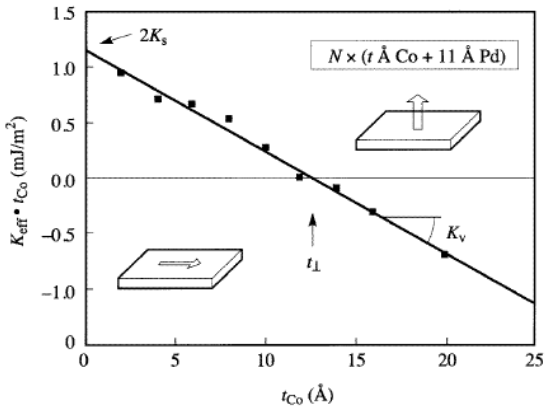

Figure 2.6: K_{ef} in function of Cobalt thickness in Co/Pd bilayer. Extracted from [41].

Part I

The Ressonant Magnetic Soliton

3 - Introduction

In 1965, an Intel co-founder Gordon Moore observed that transistors size were diminishing so fast that every year twice as many could fit onto a chip, in other words, the density of processing devices was doubling every year. In 1975 the pace was adjusted to the density doubling in every two years. This is known as Moore's law (although it's not a law, but a prediction).

The capacity of processing devices increased and the cost decreased exponentially from $228/GB in 1998 to $0.06/GB in 2010 [43]. For comparison, between 2000 and 2009, the number of transistors in a chip increased from 37.5 million per chip in 2000 to 904 million in 2009 [44]. This law does have a limit, once the transistors reach the atom size, it will be impossible to keep increasing the density.

Data storage capacity also increases in time [45], but haven't grown in the same pace as Moore's law, causing a performance gap between processing (CPU) and storage (HDD - hard drive disks) units. In ten years, the magnetic recording spinning disk used in hard drive disks came from 10K rpm up to 20K rpm. The bit size is getting smaller, but the velocity isn't getting faster due to mechanical limitations.

In the recent researches, Magnetic Random Access Memories $MRAM$ [5,6,46] have pointed out to be promising to overwhelm the limits of actual Dynamic Random Access Memories $DRAM$ used in commercial devices nowadays. The most usual $MRAM$s consists in a matrix of Magnetic Tunnel Junctions (MTJ) where a bit is defined by the magnetic orientation of one of the layers in the junction. Magnetic vortex can also be used in the $MRAM$ technology. Stable vortex-states can exist in magnetic nanostructures, like disk-shaped nanodots, owing to the competition between the exchange and the magnetic dipole - dipole interaction. The usage of a magnetic vortex to realize is done by one bit having a few possible states according to the chirality and polarity of a vortex, and thus can carry more information [47, 48]

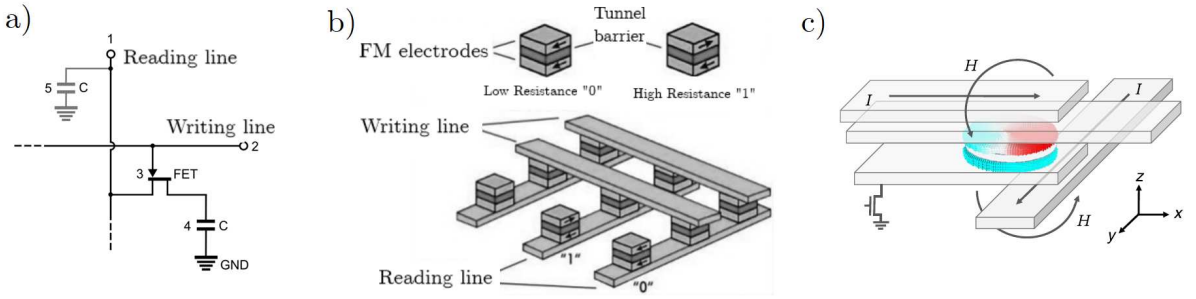

Figure 3.1: Scheme of a **a.** DRAM and **b.** MRAM. The first uses a capacitor and a transistor to define the 0 and 1 states, depending on which the capacitor is charged or not. The second defines a bit by the high or low resistance in the MTJ. **c.** Vortex-MRAM, the upper disk represents the storage layer and the lower disk represents the reference layer in a single domain.

An alternative to the $MRAM$ are the Racetrack Memories (RM), proposed by Stuart Parkin [21]. Here, the information are transported by magnetic domains, separated by domain walls (DW) in a stripe of ferromagnetic material. To tansport those magnetic domais, pulses of electrical currents are applied. Those domains are generated by an Oersted field and read by a magnetoresistive signal in vertical MTJ structures [49]. The low energy consumption for transport and the stability against thermal fluctuation are the advantages of DW-based RM [50]. However, the domain walls are highly sensitive to defects due to fabrication, that can lead to fixation points and stop, slow down or destroy the magnetic domains.

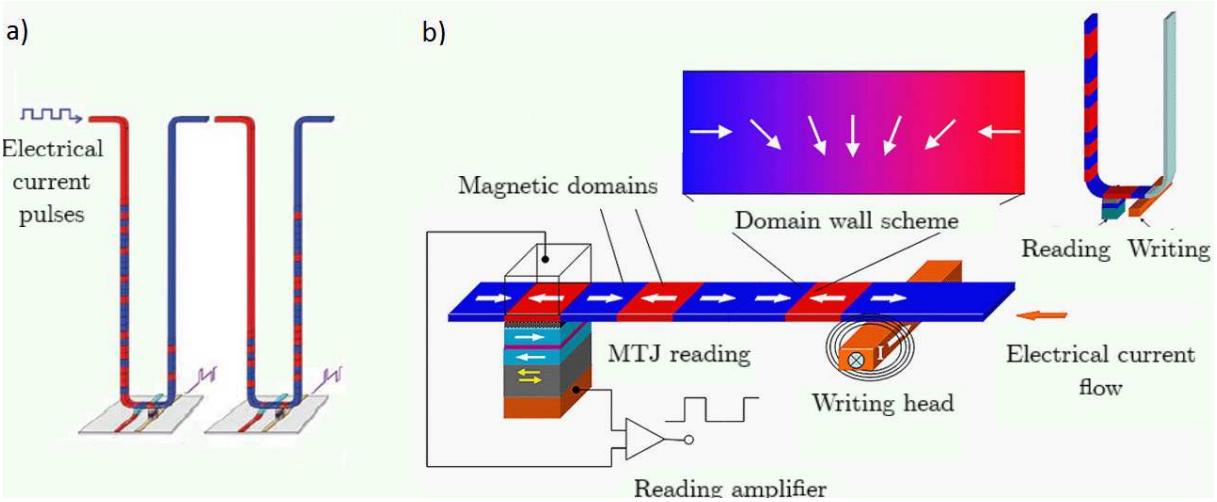

Figure 3.2: **a.** Schematic diagram of the racetrack memory devices proposed by Parkin, with the vertical stripe of magnetic material with the opposite magnetic domais in red and blue. **b.** Scheme for writing and reading the information in the racetrack memory. Adapted from [21, 49]

The domain wall-racetrack (DW-RM) device is composed by a stripe of soft ferromagnetic material with in-plane magnetization and a current density in the order of $10^8 Acm^{-2}$. The velocity of the DW in RM increased from 100 m/s in 2008 [51] up to 750 m/s in 2015 [52] with a current density in the same order of magnitude.

An alternative for the DW-RM system was proposed in 2013 by Albert Fert [22] with the utilization of magnetic Skyrmions, a type of magnetic excitation induced by Dzyaloshinskii-Moriya interaction on perpendicularly magnetized ferromagnetic materials, better discussed in chapter 4.

4 - Spintronics and Skyrmionics for Memory Devices

In condensed matter, a magnetic skyrmion is a kind of topologically protected soliton, with strong Dzyaloshinskii-Moriya interaction (DMI), characterized by an in plane chirality and an out of plane magnetization in the center and and in the borders (with opposite directions). They were named after Tony Skyrme [53] for a work in 1962 that describes localized particle-like systems with a nonlinear field theory for interacting pions. Those pions are described by bosonic fields, but in the Skyrme work, the localized particle-like solutions can be interpreted as baryons.

Topology is a concept to classify geometrical properties of continuous structures (vector fields, space functions, etc). This means the skyrmion, as long it stays far of the edge of the sample, it can't be created or annihilated due to a topological energy barrier and it can coexist with a ferromagnetic state (parallel spins). Another feature of skyrmions is a very low sensibility to pinning by deffetcs or impurities, as they are topologically protected entities [54]. This is the main advantage of the recent proposition of using skyrmions in racetrack devices with the spin transfer torque mechanism (subsection 5.1.1) responsible for moving those structures along a racetrack.

The different interactions on a magnetic system are due mainly to the exchange interaction Equation 2.4, that tends to align the magnetic moments ferro or antiferromagnetically. This interactions can also have contributions from anisotropy, magnetostatic effects and spin-orbit coupling, responsible tfor the broken inversion symmetry of the Dzyaloshinskii-Moriya interaction.

In a skyrmion structure, mainly the exchange and DMI compete each other, causing a deviation in the spins from the (anti)ferromagnetic order. The result is an helical order, depending on the direction of the vector $\vec{D}_{ij}$ (see section 2.2). The magnetic configuration of skyrmions are presented in Figure 4.1.

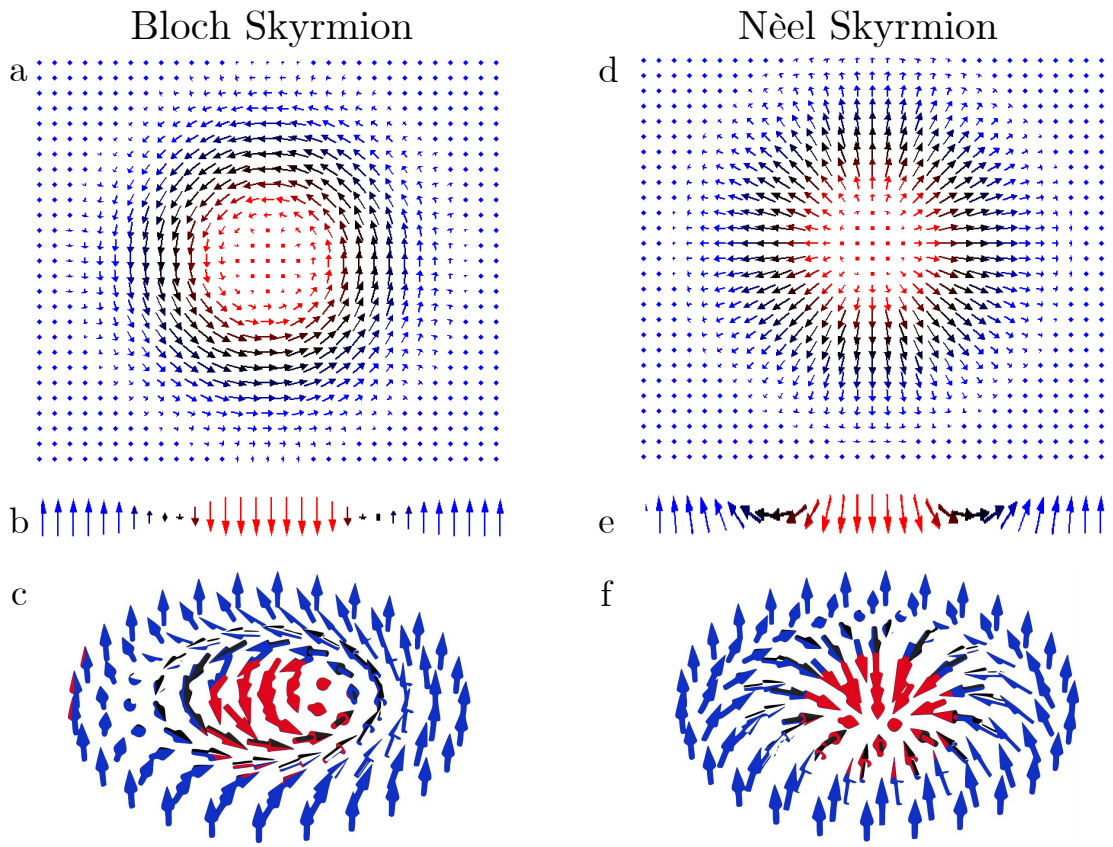

Figure 4.1: Comparison between Bloch and Nèel-type skyrmions with **a** and **d** the top view of the spins configuration. **b** and **e** the cross section of the figures above, showing the direction of rotation of the spins. In the Bloch-type, the spins rotate perpendicular to the radial direction, form the core to the borders and in the Nèel-type the skyrmions rotate in the radial plane. **e** and **f** (adapted from [55]) shows the perspective view of the Bloch and Nèel-type respectively.

The first evidence of the skyrmion phase came in 2009 in MnSi crystals [56–59], where a magnetic structure with helical phase was observed with the presence of a perpendicular applied magnetic field (it was called "A-phase" before it was found out to be a skyrmion lattice phase). From this point, skyrmion phases at low temperatures were observed in many different materials, like $Fe_{1-x}Co_xSi$ [17, 60], $Mn_{1-x}Co_xSi$ [61], FeGe [62, 63]. The induced DMI quiral state in those works appear in low temperatures. More recent works [64, 65] show skyrmion crystals at room temperature in $Co_xZn_yMn_z$ polycrystalline films.

From 2013, another pathway to create skyrmions at room temperature, to overcome the reliability of DM at room temperature, limited by the materials selection, was proposed with the interaction between a magnetic vortex and a magnetic thin film with out-of-plane anisotropy [66–68] and Co/Ru/Co multilayers [69] without DMI. The proposition of Sun *et. al.* [66] was to create an hexagonal array of magnetic nanodisks with vortex configuration [70], arranged similarly to the lattice of skyrmions in the chiral materials cited before and built on top of a perpendicularly magnetized thin film (CoPt) as shown in Figure 4.3.

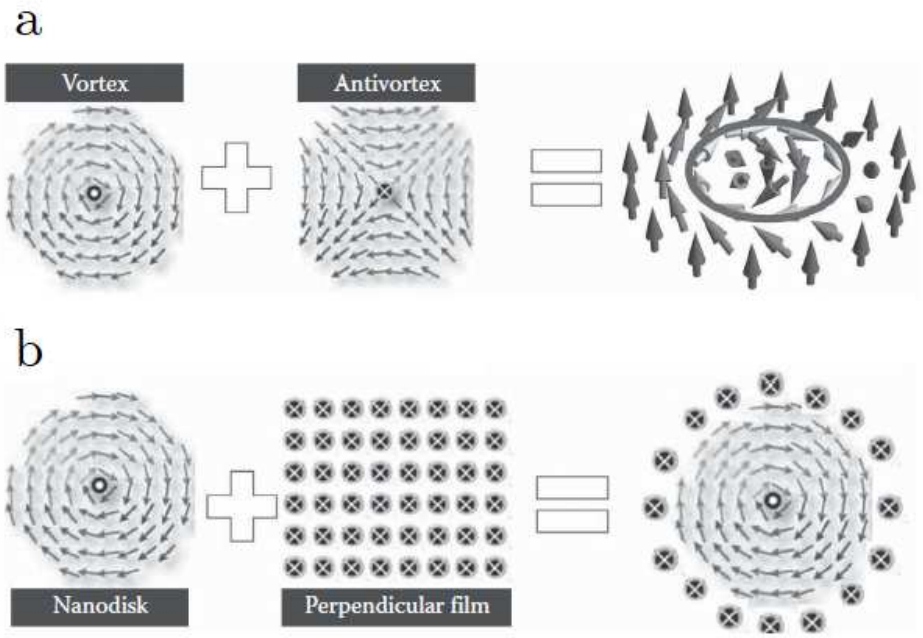

Figure 4.2: **a.** A skyrmion can be built by a superposition of a vortex-antivortex states. **b.** A skyrmion may form through implanting a vortex into a perpendicular film. Extracted from [50].

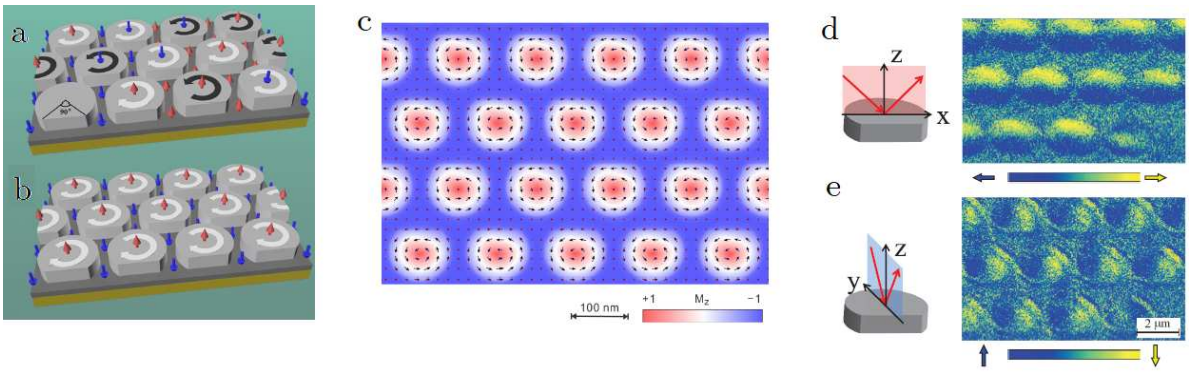

Figure 4.3: **a.** Proposal with the Co nanodisks on top of CoPt layer without magnetic field. **b.** Skyrmion lattice creation after applying a magnetic field. **c.** Top view of calcuted magnetic configuration of the CoPt layer. The arrows represents in plane spins configurations. Extracted from [66]. **d.** Kerr microscopy images with the sensitivities along the x axis and **e.** along y axis. Extracted from [67].

In the skyrmion-based racetrack devices [17, 22, 71–74], the skyrmions are the responsible for storage and transport of information. Figure 4.4 shows the micromagnetic simulation of skyrmions in racetracks. By applying a spin polarized current, the skyrmion moves in the track by spin transfer torque. The interaction between consecutive skyrmions decays exponentially [75] and the distance between them can be around 30nm without consequences. For a practical application, the separation of $\approx$ 62nm is shown to be the ideal for writing and detection of different bits, which can be defined as 0 or 1 for a skyrmion state or uniform ferromagnetic state, respectively [76].

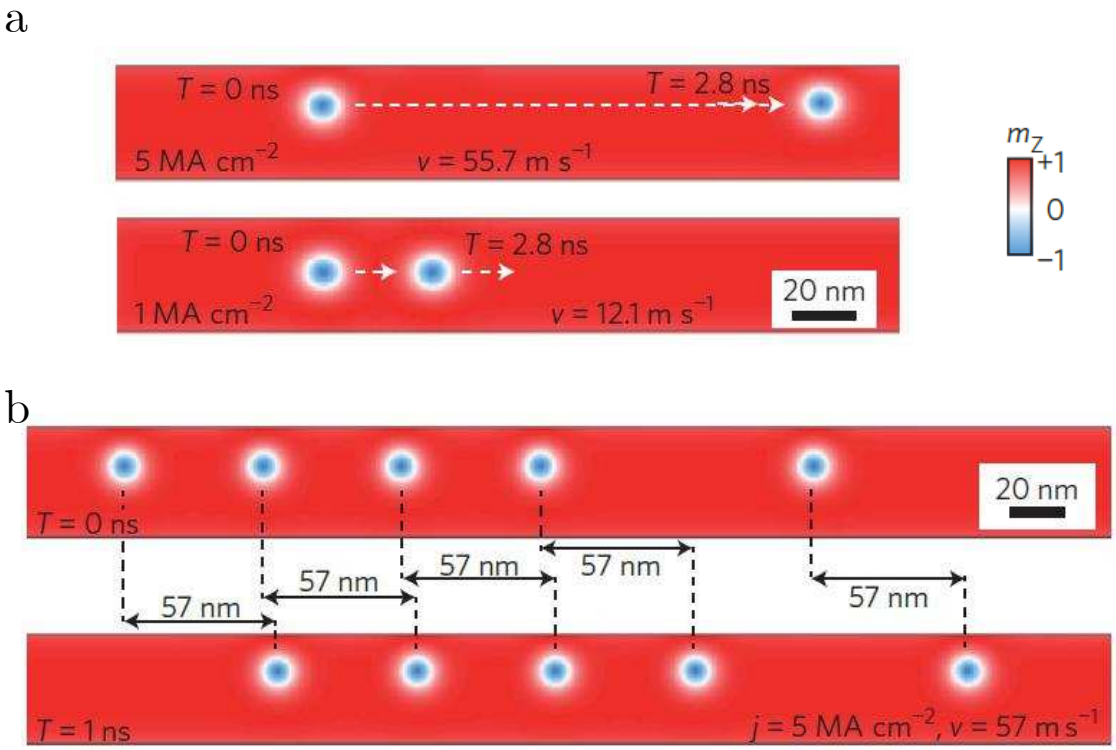

Figure 4.4: a. Micromagnetic simulations of current-induced motion of individual skyrmions or chains of skyrmions showing the dependence of the velocity with the current density. **b.** Individual skyrmions and chains of skyrmions exhibit the same velocity and can travel with a distance between each other of around 57nm. Extracted from [22].

After Fert's proposal, several others came up to use skyrmions in racetrack devices [76, 77], as shown in Figure 4.5, leading to applied researches for logic computing application and electric devices based on skyrmions, making skyrmionics a promising technology to future real applications. [78–81]. These devices, even with the experimental realization, still have limitations due to the need of applying an external magnetic field in order to create or stabilize the skyrmions besides the need for the DM interaction and the skyrmion hall effect (see section 5.3) which arises in skyrmion systems with charge $Q = \pm 1$.

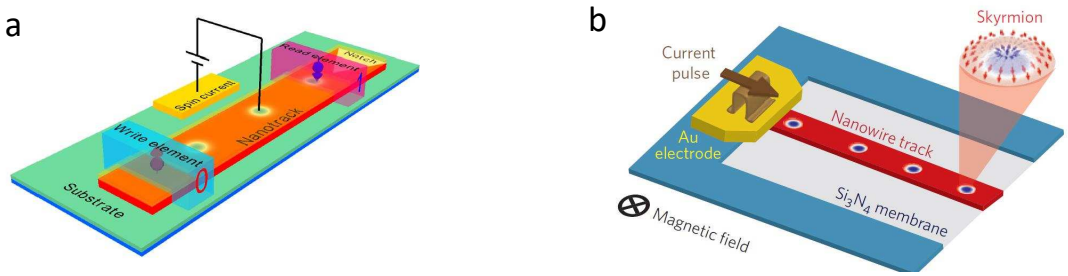

Figure 4.5: Skyrmion-based racetrack devices proposed **a.** Zhang (2015) [76], where a perpendicular electrode in the middle of the track is responsible to induce the skyrmion creation and **b.** Woo (2016) [77], where a protocol of magnetic fields are necessary to create the skyrmions.

5 - Methodology

5.1 Micromagnetic Simulations with Mumax^3

5.1.1 Dynamic Theory of Ferromagnets: Landau-Lifshitz equation

The first theories that investigated the magnetic phenomena were proposed in the early XX century with Pierre Curie by studiying the paramagnetic susceptibility of substances. Paul Langevin explained diamagnetism and, in 1907, Pierre-Ernest Weiss developed the theory of an spontaneous magnetic field in solids to explain the alignment of micromagnets (atomic spins) in a ferromagnetic material. This spontaneous magnetization is related to the crystal structure of the ferromagnetic material, which tends to align those spins in the easy axis, called Weiss Domains [82]. The modern magnetization theory started with Akulov and Becker in 1929 by studying the anisotropy energy for Fe and Ni [83, 84]. Further progress came with the development of the quantum mechanics in the following years. In 1932, Felix Bloch worked towards the theory of the structure of the region between two Weiss domains, that might have a finite length, due to the exchange energy, [85] now known as the Bloch wall, similar to shown in Figure 5.1.

Figure 5.1: Representation of a Bloch Wall

In 1935, Landau and Lifshitz [86] introduced a continuous theory for those walls, giving the first interpretation for those domain patterns, which are mainly governed by the minimization of the stray field energy. This theory describes the motion of magnetic moments in ferromagnetic materials by the precession of a spin vector induced by an effective magnetic field. The modern concept of Micromagnetism was introduced by Brown in 1958 [87] where the beginning computational science in the 40's allowed the solution of the Landau-Lifshitz (LL) equation numerically.

From the classical mechanics, the equation for a rigid body in a rotational movement is:

$$\frac{d\vec{L}}{dt} = \vec{\tau} \tag{5.1}$$

where $\vec{\tau}$ is the torque acting the angular momentum $\vec{L}$.

Suppose a rigid magnet of length l and magnetic dipole moment m in the presence of a magnetic field $\vec{H} = \vec{H}(x)$, as shown in the Equation 5.5.

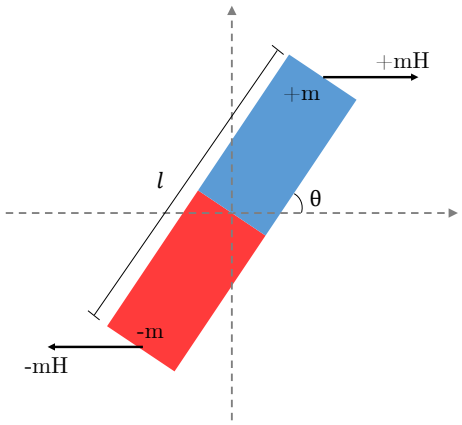

Figure 5.2: Torque experienced by a rigid magnet with opposite moments $+m$ and $-m$

Each pole will experience a force

$$\vec{F_1} = +m\vec{H} \tag{5.2}$$

$$\vec{F_2} = -m\vec{H} \tag{5.3}$$

In a referential in the center of the magnet, the total force is zero, but the torque is given by:

$$\vec{\tau} = \sum_i \vec{r} \times \vec{F_i} \tag{5.4}$$

$$\vec{\tau} = (\vec{r_1} \times \vec{F_1}) + (\vec{r_2} \times \vec{F_2}) \tag{5.5}$$

where $\vec{r}$ is the vector from the center of the magnet to m with $l = 2\left|\vec{r}\right|$. From Equation 5.2 and Equation 5.3, Equation 5.5 becomes:

$$\vec{\tau} = (m_1\vec{r} \times \vec{H_1}) + (m_2\vec{r} \times \vec{H_2}) \tag{5.6}$$

$$\vec{\tau} = 2m\vec{r} \times \vec{H} \tag{5.7}$$

We will define here, the magnetic moment $\vec{M} = m\,\vec{l}$, where $\vec{l}$ is the vector between the two poles. Equation 5.7 becomes:

$$\vec{\tau} = \vec{M} \times \vec{H} \tag{5.8}$$

From Equation 5.1 and Equation 5.9,

$$\frac{d\vec{L}}{dt} = \vec{M} \times \vec{H} \tag{5.9}$$

In a quantum mechanical system, the magnetic moment $\vec{M}$ can be replaced by the quantum spin operator $\vec{S}$

$$\frac{d\vec{S}}{dt} = \vec{\tau} \tag{5.10}$$

and the magnetic moment of an electron is related to the spin moment by the relation:

$$\vec{M} = -\gamma\vec{S} \tag{5.11}$$

where

$$\gamma = \frac{g\,|e|}{2m_e c} \tag{5.12}$$

is the gyromagnetic ratio. g is the Landè factor, a dimensionless constant ($\approx 2.002319...$ for an electron), e is the elementary charge, m_e is the electron mass and c is the speed of light.

Then

$$\frac{d\vec{S}}{dt} = -\frac{1}{\gamma}\frac{d\vec{M}}{dt} = \vec{M} \times \vec{H}$$

$$\frac{d\vec{M}}{dt} = -\gamma\vec{M} \times \vec{H} \tag{5.13}$$

This is the LL model for dynamics of a magnetic moment in an external magnetic field. It represents the precession of $\vec{M}$ around $\vec{H}$, without any energy loss, as illustrated in Figure 5.3a.

This equation can also be delivered from a quantum mechanical approach, by considering the Heisenberg equation, which says the time evolution of an observable is given by its commutator with the Hamilton operator. For the spin operator:

$$i\hbar\frac{d}{dt}\langle\hat{S}\rangle = \langle[\hat{S}, \mathscr{H}]\rangle \tag{5.14}$$

Here, $\mathscr{H}$ is the Hamiltonian, in our case, described by the Zeeman energy

$$\mathscr{H} = -\frac{g\mu_b}{\hbar}\left(\hat{S}\cdot\vec{H}\right) \tag{5.15}$$

Ferromagnetic substances shows, in a range of applied magnetic field strengths, the magnetization as shown in the Figure 6.2. In order to take account of this experimental fact, it was added a phenomenological damping term in the Equation 5.13 that describes how the magnetization acts in its precessional motion to reach the energy minimum, where this energy is dissipated until $\vec{M}$ becomes aligned to $\vec{H}$. This damping may be described by the Gilbert term, added up to Equation 5.13, that becomes [88] :

$$\frac{d\vec{M}}{dt} = -\gamma\vec{M}\times\vec{H} + \frac{\alpha}{M}\left(\vec{M}\times\frac{d\vec{M}}{dt}\right) \tag{5.16}$$

This is the Landau-Lifshitz-Gilbert (LLG) equation. The second term in the right side is due to the Gilbert damping. α is a dimensionless constant, that depends on the material.

Equation 5.16 describes the motion of the magnetization $\vec{M}$ in an external magnetic field $\vec{H}$. The first term indicates the precession of $\vec{M}$ becomes aligned to $\vec{H}$ where the second is related to the energy loss, and tends to align $\vec{M}$ with $\vec{H}$ (Figure 5.3b).

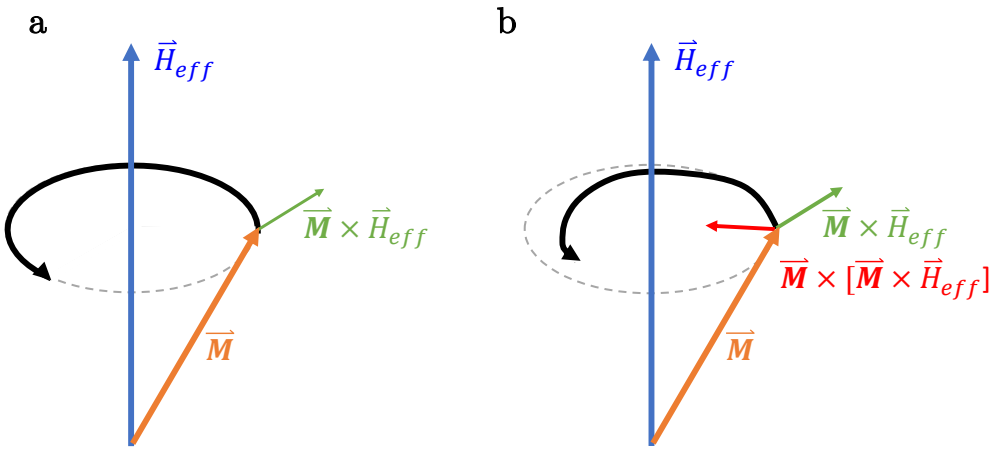

Figure 5.3: LLG equation representation. **a.** Without and **b.** with the Gilbert damping term. The magnetization (red) precesses around the effective field (blue). The Gilbert damping term adds a component (green) that leads M towards the low energy equilibrium state of the system. Adapted from [89]

Spin-polarized electrical currents interact with magnetic moments via spin-transfer torque (STT). In addition to the standard LLG equation when in presence of a spin polarized current, John Slonczewski and Luc Berger in 1996 [7, 8], proposed a model for this spin momentum transfer (SMT) and introduced a term in the LLG equation. The spin polarization of the con-

duction electrons of the electrical current can transfer momentum to the layer magnetization, applying a spin-transfer torque that can affect the magnetic moments without applying a magnetic field. The Slonczewski term added to the LLG equation have the form:

$$-\frac{\gamma}{\mu_0 M_s}\left[a_j\vec{m}\times(\vec{m}\times\hat{p})+b_j(\vec{m}\times\hat{p})\right] \tag{5.17}$$

where a_j are related to the in-plane torque efficiency and the first term is called the Slonczewski torque. b_j is the perpendicular torque efficiency and the second term in the brackets is a "field like" torque and $\hat{p}$ unit vector of the spin polarization. The spin current and the coefficients a_j and b_j depend on the angle between $\vec{m}$ and $\hat{p}$. The parameter $b_j = \xi a_j$ and

$$a_j = \frac{\hbar\gamma JP}{2|e|dM_s\mu_0(1+\xi^2)} \tag{5.18}$$

$\xi = l_{ex}/l_{sf}$ denotes the ratio of spin decoherence length and spin-flip relaxation length [90], J is the current density, P is the electrical current polarization and $0 \leq P \leq 1$ ($P = 1$ means that 100% of the electrons have the same spin orientation), e is the elemental charge and d is the thickness of the FM layer. The spin current and the coefficients a_j and b_j depend on the angle between $\vec{m}$ and $\hat{p}$ due to the influence of the longitudinal spin accumulation on spin transport. They indicate that the spin-torque term can be another source of precessionand it can either increase or decrease the usual damping (second term in Equation 5.16) [91]. Some works have found that the second term inside the brackets of Equation 5.17 is much smaller than the first, and can be neglected [92–95].

The fenomenological description of the STT [90,96–98] is due to the transfer of spin-angular momentum from the spin-polarized current. In an interface of a non magnetic (NM) and a ferromagnetic (FM) material, a current through the interface can act like a filter for spin states. In this current entering in a free layer, the electrons polarization are either aligned or misaligned with an angle θ in relation to the free layer magnetization direction. At the interface, when the electrons are entering the magnetic layer, a transference of angular momentum from the electron to the layer magnetization occurs.

The first process (related to the first term of Equation 5.17) is the reflection or transmission of electrons due to the difference of the energy bands related to the electron spin. The reflection probabilities depends on the electron spin and the spin-filtering effect will lead to the discontinuity of the spin components and one part of the transverse spin current is adsorbed at the interface. [99, 100].

The second process (related to the second term of Equation 5.17) is the rotation of the

scattered spins from the interface that will lead to another component of the spin torque perpendicular to $\vec{m}$ and $\hat{p}$.

The Slonczewski perpendicular and parallel torques descripted above were studied in the situation for spin valves and magnetic tunnel junctions, where the current flows through a free and a pinned magnetic layers. In the case of magnetic vortex or domain walls, where the magnetization gradually changes the direction, the STT of an electrical current is due to the adiabatic and non-adiabatic torques. In the Zhang Li model [101, 102], the adiabatic (τ_a caused by the non-equilibrium conduction electrons with polarizations that coincide with the magnetic moments) and the non-adiabatic (τ_n caused by non-equilibrium electrons whose polarizations are misaligned from the moments) STT terms are described [103, 104].

$$\vec{\tau}_a = -u_0 \vec{M} \times \left(\vec{M} \times \frac{\partial \vec{M}}{\partial x} \right) \tag{5.19}$$

$$\vec{\tau}_n = -\beta u_0 \vec{M} \times \frac{\partial \vec{M}}{\partial x} \tag{5.20}$$

for currents flowing in the x-direction. β is a dimensionless small constant. For a current in an arbitrary direction,

$$\vec{\tau}_a = -u_0 \vec{M} \times \left(\vec{M} \times \left(\vec{J}_c \cdot \vec{\nabla} \right) \vec{M} \right) \tag{5.21}$$

$$\vec{\tau}_n = -\beta u_0 \vec{M} \times \left(\vec{J}_c \cdot \vec{\nabla} \right) \vec{M} \tag{5.22}$$

here, $\vec{J}_c$ is the electrical current density vector. Those terms combined are similar to the Equation 5.17 by taking $\hat{p} = (\vec{J}_c \cdot \vec{\nabla})\vec{M}$ and

$$u_0 = \frac{Pg\mu_b}{2|e|M_s} \tag{5.23}$$

where $u_0 \cdot J$ represents the drift velocity of the conduction electrons.

5.2 Numerical Solving of LLGS Equation

In summary, the numeric simulations of the space and time-dependent dynamics in ferromagnet, for energy minimization and transitions between spin configurations, are given by numerically solving the LLGS (Landau-Lifshitz-Gilbert-Slonczewski) equation and provides a description of magnetism on a mesoscopic length scale. The LLGS equation described in the

previous section takes the form:

$$\frac{\partial \vec{m}}{\partial t} = -\gamma \vec{m} \times \vec{H}_{\text{eff}} + \frac{\alpha}{M_S} \vec{m} \times \frac{\partial \vec{m}}{\partial t} + \frac{p}{2eM_S} (\vec{J}(\vec{r}) \cdot \nabla) \vec{m}, \tag{5.24}$$

where $\vec{m} = \vec{M}/M_s$, γ is the gyromagnetic ratio, M_S the saturation magnetization, α is the Gilbert damping coefficient, p is the polarization ratio of the electric current, a is the lattice constant and $\vec{H}_{\text{eff}}$ is the effective field (subsection 5.2.1), which is composed by the magnetostatic field, the external magnetic field, the magnetocrystalline anisotropy, the Heisenberg exchange interaction, and the dipolar interaction and others. The third term on the right-hand side of Equation 5.24 is related to the adiabatic spin-transfer torque provided by the spin-polarized current $\vec{J}(\vec{r})$ in the nanotrack.

For the iterations, we have utilized the GPU-accelerated micromagnetic simulator MuMax^3 [105], that solves numerically the LLG equation with a finite-difference method for one or more ferromagnetic materials, from a two or three-dimensional space composed by a lattice of orthorhombic cells with volume $\Delta V = \Delta x \Delta y \Delta z$, where for each cell is associated a magnetic moment $\vec{m}(x, y, z)$ in the center of the cell. The input parameters of simulation, in terms of Equation 5.24 are associated to each cell. In order to conserve memory, Mumax associates those parameters for a region, that represents a material, as shown in Figure 5.4 and the numerical parameters used in this work are described in Table 6.1.

The simulation cell usually have a nanometer size, to facilitate the numerical solving and reduce the simulation time. The iterations are then calculated between cells instead of single atoms or crystalline structures. This nano-sized cell corresponds to a group of atoms oriented in the same direction.

For example, the Nickel has a face-centered cubic unitary cell, that holds 4 atoms per unit cell with lattice parameter $a_0 = 0.352nm$ [106]. In a cubic simulation cell of $d = 1nm$ side, we obtain almost 92 atoms per simulation cell. If we raise the cell to $d = 10nm$, it will hold around 91713 atoms. The cell size is limited by the exchange length (l_{ex}, defined by Equation 5.25) that defines what is large and what is small in micromagnetics [107]. A small cell ($d < l_{ex}$) is necessary to ensure uniformity in the magnetization and guarantee that the material properties are the same in the whole cell.

The exchange length is defined as

$$l_{ex} = \sqrt{\frac{2A_{ex}}{\mu_0 M_s}} \tag{5.25}$$

whereA_{ex} is the exchange stiffness of the material and M_s the saturation magnetization and

$\mu_0 = 4\pi \times 10^{-7} H/m$.

The advantages of MuMax^3 compared to other micromagnetic simulators like OOMMF (that also uses the finite discretization method), Nmag, magpar (that uses the finite elements method) and others is the simplicity input scripting specially for introducing complex geometries and, by using the graphics processing (GPU) instead of the processing unit (CPU), the simulation takes place more quickly.

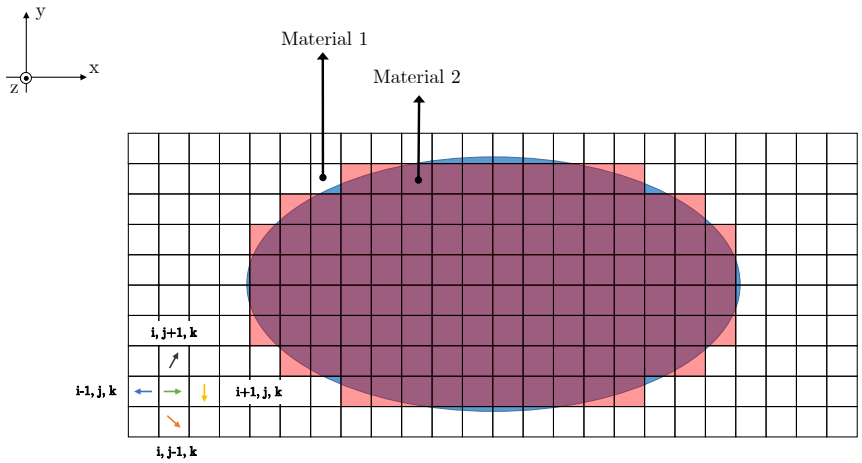

Figure 5.4: 2D representation of cells discretization in Mumax. The elliptical geometry (blue) is divided in cubic cells (red), where a magnetic moment $\vec{m}$ is associated in the center of the cell. The calculations are then made following Equation 5.24 for the neighbours spins.

According to the developers, MuMax^3 can also include [1]:

- Magnetostatic field
- Heisenberg exchange
- Arbitrary inter-region exchange like RKKY(Ruderman–Kittel–Kasuya–Yosida) coupling
- Dzyaloshinskii-Moriya interaction
- Spin-transfer torque (Zhang-Li and Slonczewski)
- Uniaxial and cubic magnetocrystalline anisotropy
- Thermal fluctuations (Brown)
- Voronoi tessellation
- Time and space dependent material parameters
- Arbitrary complex excitation (field, current)
- Optional 1D, 2D or 3D periodic boundary conditions

[1] mumax.github.io

5.2.1 The effective Field

The effective field, on the first term of Equation 5.24 is composed by [108]:

$$\vec{H}_{eff} = \vec{H}_{ext} + \vec{H}_{exch} + \vec{H}_{ani} + \vec{H}_{demag} + \vec{H}_{DM} + \vec{H}_{current} + \vec{H}_{th} \tag{5.26}$$

where $\vec{H}_{ext}$ is the external applied field, $\vec{H}_{exch}$ is the exchange field, $\vec{H}_{ani}$ takes account of the anisotropy contributions, $\vec{H}_{demag}$ is the demagnetization field, $\vec{H}_{DM}$ is the Dzyaloshinskii-Moriya interaction, $\vec{H}_{current}$ is the field due to electrical currents and $\vec{H}_{th}$ is the thermal field. In the micromagnetic approach, the energies associated with the components of the effective field have to be minimized.

The **external field** is, the energy associated is the Zeeman energy. The magnetization tends to align with this field. This energy have the form:

$$E_z = -\mu_0 M_s \int \vec{m} \cdot \vec{H_{ext}} \tag{5.27}$$

The **exchange field** is due to the exchange interaction (section 2.1) where atoms interact with the first neighbours. The energy associated to this interaction is written:

$$E_{exch} = A_{ex} \int (\nabla \vec{m})^2 dV \tag{5.28}$$

with A_{ex} the exchange constant (or exchange stiffness), $\vec{H}_{exch}$ the exchange field given by

$$\vec{H}_{exch} = \frac{2A_{ex}}{\mu_0 M_s} \nabla^2 \vec{m} \tag{5.29}$$

which for Mumax [105], it's used in a six-neighbour evaluation in the form:

$$\vec{H}_{exch} = \frac{2A_{ex}}{\mu_0 M_s} \sum \frac{(\vec{m_i} - \vec{m})}{\Delta_i^2} \tag{5.30}$$

where i are the six nearest neighbours of the of the cell with magnetization $\vec{m}$. Δ_i is the separation between the center of the consecutive cells.

The **anisotropic field** take account of the anisotropic effects of the materials and it can come from different sources, as magnetocrystalline anisotropy, shape anisotropy or interface interactions (section 2.3).

The energy associated with a unaxial anisotropy have the form:

$$E_{ani} = -K_u \int (\vec{m} \cdot \hat{n}) dV \tag{5.31}$$

where K_u is the anisotropy constant, $\hat{n}$ is a unit vector indicating the anisotropy axis, with a field given by

$$\vec{H}_{ani} = \frac{2K_{u1}}{\mu_0 M_s}(\vec{m}\cdot\hat{n})\hat{n} + \frac{4K_{u2}}{\mu_0 M_s}(\vec{m}\cdot\hat{n})^3\hat{n} \tag{5.32}$$

where K_{u1} and K_{u2} are the first and second order uniaxial anisotropy constants respectively.

The **demagnetization field** is the responsible for the domain formation and is the biggest contribution for the effective field (depending on the strength of external field). The demagnetizing field can be found from the magnetostatic Maxwell equations.

$$\nabla\cdot\vec{B} = 0 \tag{5.33a}$$

$$\nabla\times\vec{H}_d = 0 \tag{5.33b}$$

for $\vec{B} = \mu_0(\vec{H}_d + \vec{M})$ and $\vec{H}_d$ the demagnetizing field. The field $H_d = -\nabla\phi$, where ϕ is the magnetostatic scalar potential. A complete approach for this field is done in Makarov [108].

The **Dzyaloshinskii-Moriya** field due to the interaction (Equation 5.35), can be due to the interfacial and bulk DM. The respective effective fields are written

$$\vec{H}_{DM} = -\frac{2D}{M_s}\left[(\nabla\times\vec{m})\hat{z} - \nabla m_z\right] \tag{5.34}$$

with the boundary conditions

$$\begin{aligned}
\left.\frac{\partial m_x}{\partial x}\right|_{\partial V} = \left.\frac{\partial m_y}{\partial y}\right|_{\partial V} &= -\frac{D}{2A}m_z \\
\left.\frac{\partial m_z}{\partial x}\right|_{\partial V} = \left.\frac{\partial m_z}{\partial y}\right|_{\partial V} &= \frac{D}{2A}m_x \\
\left.\frac{\partial m_y}{\partial x}\right|_{\partial V} = \left.\frac{\partial m_x}{\partial y}\right|_{\partial V} &= 0 \\
\left.\frac{\partial m_x}{\partial z}\right|_{\partial V} = \left.\frac{\partial m_y}{\partial z}\right|_{\partial V} = \left.\frac{\partial m_z}{\partial z}\right|_{\partial V} &= 0
\end{aligned}$$

with A the exchange stiffness and D is the DMI constant (in J/m^3). The related energy is [109]:

$$E_{dm} = t\int\int D\left[\left(m_x\frac{\partial m_z}{\partial x} - m_z\frac{\partial m_x}{\partial x}\right) + \left(m_y\frac{\partial m_z}{\partial y} - m_z\frac{\partial m_y}{\partial y}\right)\right] \tag{5.35}$$

for t the sample thickness.

5.3 Skyrmion Hall Effect

One of the main problems in skyrmion systems is the Skyrmion Hall Effect (SkHE) [110], an analog of the usual Hall effect, where a current flowing through an conductor in the presence of an external field results in a measurable electric field perpendicular to the current direction due to the accumulated charges on opposite sides of the material. The route made by a skyrmion, when moving in a racetrack, is not a straight line [111, 112], as it feels a Magnus force while moving. This force shifts its trajectory towards the border of the racetrack and it can happen even in Skyrmion crystal [113]. This effect was experimentally obeserved in [114, 115].

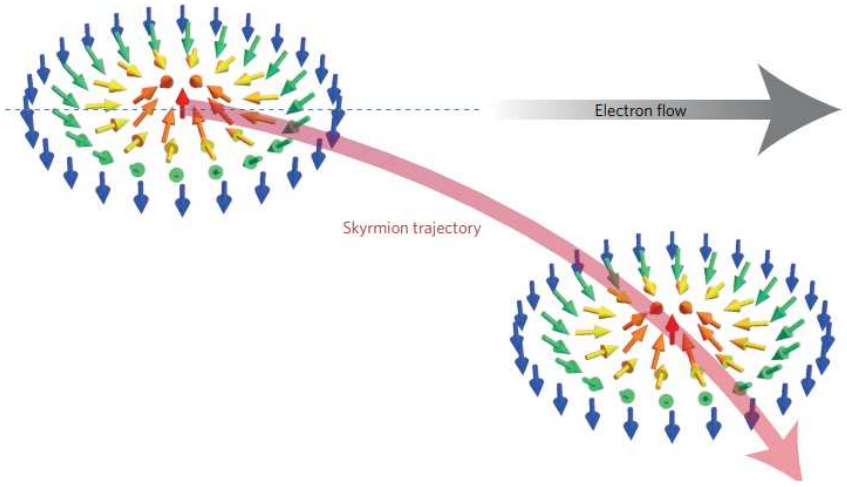

Figure 5.5: Schematics of the skyrmion Hall effect. Extracted from [110]

The translational motion of a skyrmion driven by the in-plane current (CIP) can be described by a modified Thiele equation [116]:

$$\vec{G} \times (\vec{v}^{(s)} - \vec{v}^{(d)}) - \mathcal{D} \cdot (\beta \vec{v}^{(s)} - \alpha \vec{v}^{(d)}) + \nabla V(\vec{r}) = 0 \tag{5.36}$$

where $\vec{G} = (0, 0, 4\pi Q)$ is the gyromagnetic coupling vector, for Q the topological charge. $\mathcal{D}$ is a dissipative force tensor describing the effect of the dissipative forces on the moving magnetic skyrmion. $V(\vec{r})$ is the confining potential induced by the sample edges; α is the Gilbert damping term and β is the non-adiabatic torque term. $\vec{v}^{(d)}$ is the skyrmion drift velocity and $\vec{v}^{(s)}$ is the skyrmion velocity due to STT [117].

Considering a skyrmion moving in the $+x$ direction ($\vec{v}_x^{(s)} \neq 0$ and $\vec{v}_y^{(s)} = 0$), far away from the edges ($V = 0$), with an electrical current applied in the $-x$ direction. By solving the Equation 5.36 with the conditions presented, we can find the drift velocities:

$$\vec{v}_x^{(d)} = \left(\frac{\beta}{\alpha} + \frac{G^2}{\alpha} \frac{(\alpha - \beta)}{(G^2 + \alpha \mathcal{D}^2)} \right) \vec{v}_x^{(s)} \tag{5.37}$$

$$\vec{v}_y^{(d)} = \left(\mathcal{D}G \frac{(\alpha - \beta)}{(G^2 + \alpha \mathcal{D}^2)} \right) \vec{v}_x^{(s)} \tag{5.38}$$

Here we can see that, for a skyrmion moving in the x direction ($\vec{v}_x^{(s)} \neq 0$) and having a non-zero topological charge ($G \neq 0$), it will be subject to a perpendicular drift velocity, dependent of the Gilbert damping term α.

6 - Results

From the skyrmionics proposed so far, in this work, using full micromagnetic simulations, we propose a device where external magnetic fields and DMI are absent, and is capable to transport a new kind of magnetic spin texture through a nanotrack. The scheme is shown in the Figure 6.1. The device consists in a magnetic nanotrack, made of Platinum/Cobalt where the magnetization is perpendicular to the plane, with dimensions of 2000 x 200 x 8 nm^3. A Cobalt nanodisk, 120nm diameter and 20 nm thick, is used to induce in the nanotrack a skyrmion phase that moves in the nanotrack when a spin-polarized electrical current protocol is applied. On the opposite side of the track, a magnetic tunnel junction (MTJ) is used to detection of the structure when it passes below the junction. The MTJ is composed by a 2nm oxide layer and a 120nm diameter and 20nm thick nanodisk made of the same material of the track. Two electrical contacts between the opposite sides of the track are used to apply the electrical current and an electrical contact between the MTJ and the track is used to measure the tunnel magnetoresistance. The steps for creation, transport and detection of the moving structure are described in the chapter 6.

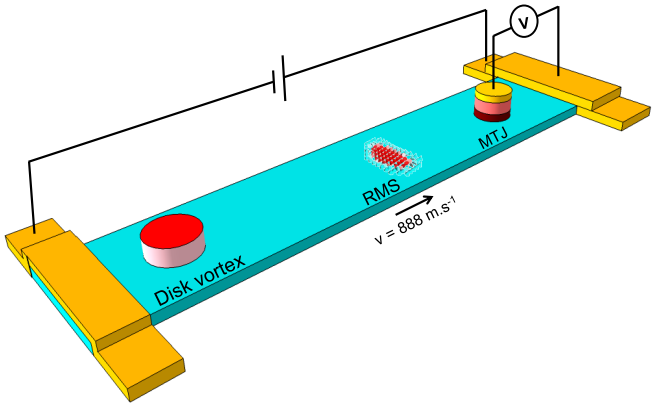

Figure 6.1: Proposed device composed by a nanotrack (light blue) with perpendicular magnetization, a nanodisk with vortex magnetization (red, on the left side) responsible to imprinting the magnetic spin texture in the track, a magnetic tunnel junction (wine/yellow stack, on the right side) for detection and electrical contacts (yellow) to applying electrical current, responsible to moving the structure.

The finite difference discretization used by MuMax^3 to follow Equation 5.24 is performed in a space of a two or three-dimensional grid of orthorhombic cells. Here, we have utilized a cubic cell of 4 nm $\times$ 4 nm $\times$ 4 nm for the iterations. Magnetic parameters for Co and CoPt are adopted

from [66] and displayed in the table below.

Material	**Pt/Co**	**Co**
Magnetization	Out of plane	In plane
M_s (A/m)	5×10^5	1.4×10^6
A_{ex} (J/m)	1.5×10^{-11}	2.5×10^{-11}
K_u (J/m^3)	$(2-5) \times 10^5$	5.2×10^5
Direction (x, y, z)	$(0, 0, 1)$	$(1, 1, 0)$
α	0.3	0.3
p	0.5	0.5

Table 6.1: Parameters used in the simulations for out-of-plane (track) and in plane magnetization (disk).

From the parameters shown in Table 6.1 and the proposed device in Figure 6.1, we show in this chapter the processes since the creation of the spin texture and its detection, as well as the advantages for using this structure in racetrack devices.

6.1 The imprinted spin texture

In this simulation, according to Table 6.1, we have used different anisotropy constants (K_u), with out-of-plane easy axis, varying from $2 \times 10^5 J/m^3$ to $5 \times 10^5 J/m^3$. Figure 6.2 shows the hysteresis curves, with an external magnetic field applied in the z direction, for the system including the nanotrack and the Co nanodisk (MTJ not included). The behaviour of the magnetization for different values of (K_u) change due to the interaction of the topologically stable vortex-sate with the interaction between the core of the vortex and the track magnetization. For anisotropy values below $4 \times 10^5 J/m^3$ the coercive field increases due to the pinning caused by the vortex core polarization. For values higher than that ($K_u = 5 \times 10^5 J/m^3$), the hysteresis decreases due to the pinning loss, when the vortex core is aligned with the strong track perpendicular magnetization.

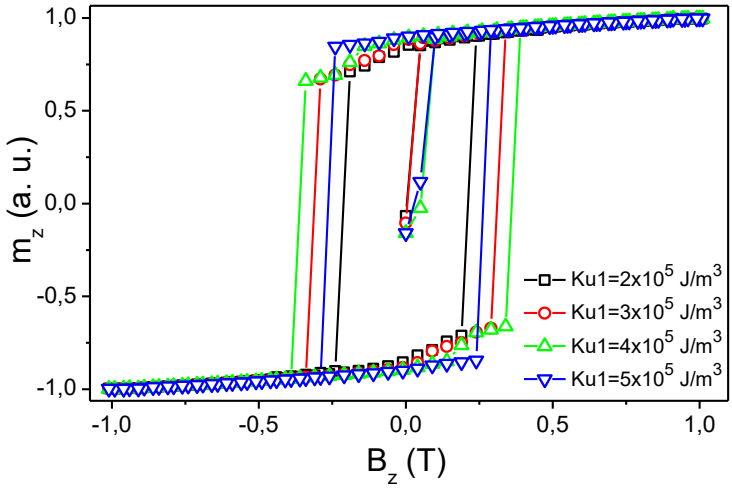

Figure 6.2: Hysteresis curves for the systems with different K_u values for the track magnetization, with an applied external field perpendicular to the plane.

The first step of the simulation process is to "relax" the system to its minimal energy state, from a random configuration of spins. The Figure 6.3 shows that, the first magnetization configuration, after relaxing, have magnetic domains distributed in the track length, in this case, the application of an external magnetic field is necessary, only in this situation, in order to annihilate the as-grown magnetic domains in the track. Note that, below the disk, an imprinted spin texture remains even when the whole track shows uniform magnetization. This structure also vanish when the field is strong enough to destroy the vortex-state in the nanodisk. It's important to notice that the magnetic field is necessary only once, after the device fabrication and the disk magnetization remais in vortex state in the whole process. This magnetic field is not necessary in the next steps and this one of the advantages over the other devices proposed so far [76, 118, 119].

The remanent magnetization recorded under the disk, after applying small field B_z to saturate the magnetization just in the stripe is presented in Figure 6.4, from the bottom point of view displaying the magnetization behaviour on the track (white color represents the in-plane spins, while red and blue represent the opposite out-of-plane spin configurations. Here we notice imprinted skyrmion-like structures, with topological charge $Q \approx -1$, for the magnetization in the stripe in each case presented in the figure. The skyrmion diameters decrease with PMA strength increasing.

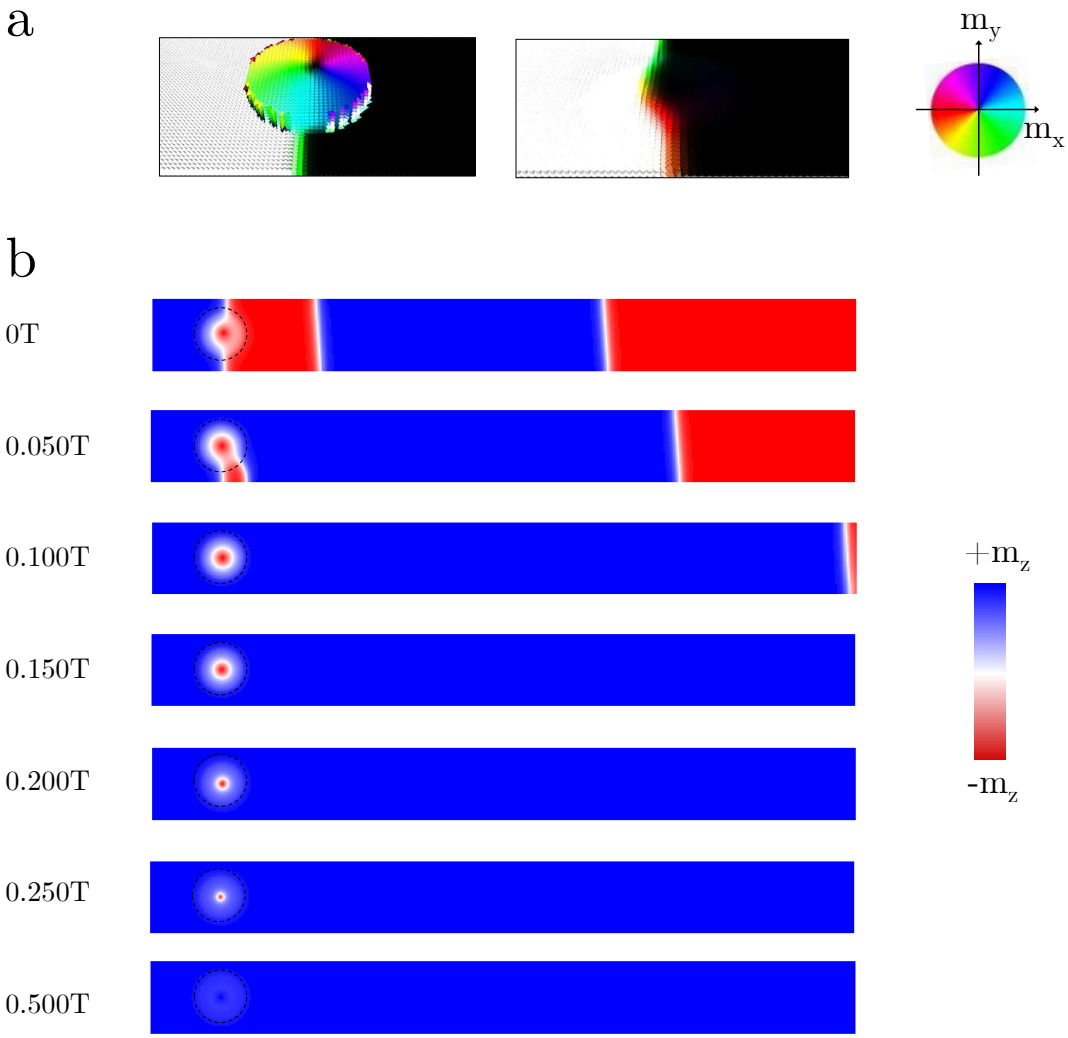

Figure 6.3: **a.** Perspective view of the top and bottom of the track with zero field, displaying the in-plane magnetization according to the color scale. The nanodisk is in a vortex-state configuration. **b.** Partial view of the bottom part of the track of $K_u = 5 \times 10^5$ J $\cdot$ m^{-3}, for several external applied fields in the $+z$ direction. The dashed lines show the diameter of the Cobalt disk, in the top part of the track.

Here, we find that the imprinted spin texture (IST) can be treated as a skyrmions [120, 121] with the topological number of $Q \approx -1$, for the magnetization in the nanotrack in each case presented. As shown in Figure 6.4a the skyrmion diameter decreases with increasing PMA strength.

It should be noted that the topological number (also called winding number) Q is defined as [122, 123]:

$$Q = \int \frac{1}{4\pi} \vec{m} \cdot (\frac{\partial \vec{m}}{\partial x} \times \frac{\partial \vec{m}}{\partial y}) dx dy, \tag{6.1}$$

where $\vec{m}$ is the reduced magnetization. This winding number means the number of times the spins (or field) configuration wraps the suface of the internal sphere [50]. In theory, the topological number Q for a skyrmion is strictly equal to ± 1 in the continuous model, with boundary

conditions $\vec{m}(\vec{r} \to \infty) = (0, 0, 1)$ and $\vec{m}(\vec{r} = 0) = (0, 0, -1)$ or vice-versa (for $\vec{r} = 0$ in the center of the skyrmion), however, due to the numerical discretization of the simulation process, we have $Q \approx \pm 1$ for a skyrmion in the micro-magnetic system.

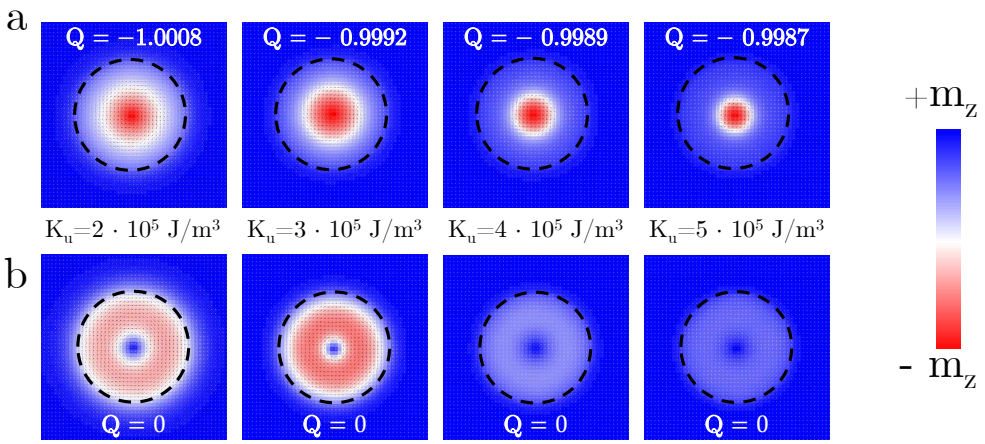

Figure 6.4: Imprinted spin textures under the disk for different values of K_u according to the table 6.1. **a.** Structures formed below the disk after applying an external magnetic field $B_z = +0,150T$ with respective values of Q in each structure. **b.** Structures formed below the disk after applying an external magnetic field $B_z = +0,500T$ with respective values of Q in each structure. The dashed lines represents the diameter of the disk in the opposite side of the track.

Figure 6.4-b shows the remanent state of the system after the total out-of-plane magnetization saturation, for track and disk. In this case, it is possible to note that the skyrmion-like structure is not formed again, but a chiral configuration could be formed, in which the magnetic vortex core is not opposite anymore to the nanotrack background magnetization. This structure now have the topological number of $Q = 0$ and it is known as the skyrmionium [124–126], which is composed by a combination of skyrmions with opposite topological numbers, i.e., $Q = +1$ and $Q = -1$.

6.2 Detaching process

After the creation of the structure, we should move it through the track. As usual for syrmions transport [17, 63, 118] in racetracks proposed so far, an spin-polarized current have to be applied in the device. As shown in Figure 6.1, the electrical current is applied in the opposite sides of the nanotrack.

In order to detach the skyrmion from the underneath of the nanodisk and move it by STT in an adiabatic approximation [73, 127, 128], an uniform DC spin-polarized current ($J = 10 \times 10^8 A/cm^2$ with 50% of polarization) was applied in the track ($Ku_1 = 2 \times 10^5 J/m^3$) with the skyrmion-like structure imprinted, as shown in the Figure 6.5. Higher values of K_{u1} could be

used to decrease the diameter of the moving IST, but with highest Ku_1, the magnetization below the disk core turns to opposite direction, aligned with the stripe, under applied current. If the same amount of J is applied continuously, the moving IST rapidly evolves to a domain-wall pair, as shown in Figure 6.5a. The topological number of the domain-wall (DW) pair becomes large since the spin rotates many times in the region where $m_z = 0$.

In the case where a skyrmionium imprinted from the nanodisk, in the nanotrack with $K_{u1} = 5 \times 10^5$ J m^{-3} (Figure 6.5b), the current applied in the previous step is not enough to make any changes in the structure. Now, a combination of spin-transfer torque and Oersted field from $J = 53 \times 10^8$ A cm^{-2} is enough to remove a skyrmion inside the imprinted skyrmionium and expel it as a magnetic droplet. The droplet rapidly evolves to a small moving magnetic structure. However, if the same amount of J continues to be applied, it evolves subsequently to a domain wall pair (Figure 6.5b). As in the previous case, is necessary to decrease the current J to prevent it from developing into a domain wall pair. Maintaining this current, as the first created structure evolves in the track as a DW pair, after some time, another structure is expelled from below the disk and this process continues to happen.

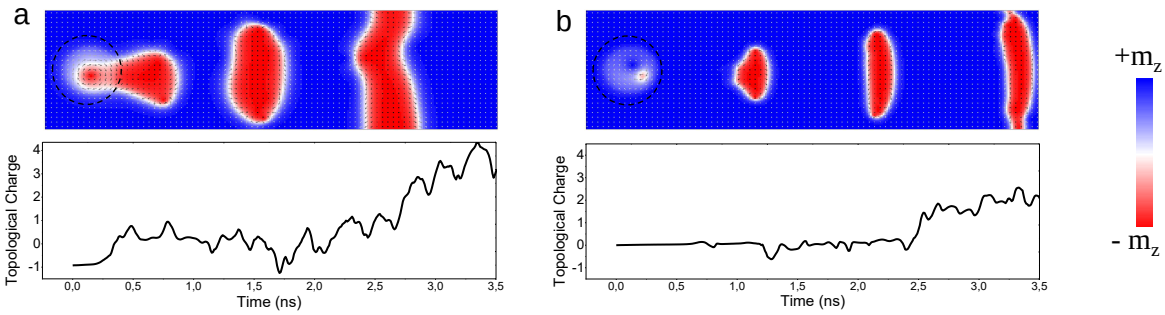

Figure 6.5: Structure behaviour after a spin-polarized electrical current is applied **a.** $J = 10 \times 10^8$ A $\cdot$ cm^{-2} in a track of $K_u = 3 \times 10^5$ J m^{-3} and **b.** $J = 53 \times 10^8$ A $\cdot$ cm^{-2} in a track of $K_u = 5 \times 10^5$ J m^{-3}. The dashed lines represents the diameter of the disk in the opposite side of the track.

After the first structure is created, from an imprinted skyrmionium, the current of $J = 53 \times 10^8$ A cm^{-2} is too high to transport a stable structure, since the expelled magnetic bubble rapidly expands and is transformed into a domain wall pair when it touches the edges. So we should reduce the current for a stable value J_s to avoid turning this system to a conventional DW racetrack.

6.3 Transport

For the initial condition, as described in Figure 6.5b, after the detaching process, by using a creation current $J_c = 53 \times 10^8$ A $\cdot$ cm^{-2}, the structure can be transported, but with huge

variations in size. In order to have a structure with stable size, after J_c is applied, we need to reduce the current. We found that the optimal value of current, to transport the structure all the way through the track is $J_s = 18.5 \times 10^8$ A cm^{-2}. If the current is higher than J_s, the structure grows until it reaches the border of the track, and if is weaker than J_s, it shrinks and disappears. The reason is that the IST cannot be stabilized in the absence of the spin-polarized current and the minimum energy takes when the radius is equal to zero. The magnetization m_z becomes constant after the disappearance of the IST. Figure 6.6 shows the time evolution of the magnetization m_z for various magnitude of the current J, where we find that the IST travels straightly when $J = J_s \equiv 18.5 \times 10^8$ A cm^{-2}. The results also show that the spin-polarized current has a force to expand the IST.

To transport a small and stable IST, we utilize a fast pulse of $J_c = 53 \times 10^8$ A cm^{-2} during 0.17 ns to create and expel the IST from the underneath of the nanodisk. After the structure is detached, the current J_c is reduced to J_s and kept during the movement where the IST reaches a stable size of 60×80 nm and a steady velocity of 888 m s^{-1} during the entire way through the 2-μm-long nanotrack. Small deformations may occur due to the strong interaction with the nanodisk magnetization during its creation, similarly to magnetic droplets formation [119, 121]. This deformations continues throughout the motion because there is no external magnetic field applied to stabilize the IST, as in the case of the skyrmion investigations performed so far [72, 129, 130].

The time evolution of the magnetization m_z during the creation and the transport of an IST is given in Figure 6.7. Small variations of m_z during the transport indicates the size stability, as also described in Figure 6.6a and can also be observed in the snapshots as given in Figure 6.7b. Figure 6.7c shows the evolution topological number Q of the nanotrack as a function of time during the creation and motion of the IST. Notice that the topological number Q is oscillating, indicating the IST is evolving rapidly between a state with $Q = 0$ and $Q_{max} \approx \pm 0.75$.

We can create a single dynamical IST with spin-polarized current pulses as described above, and analyse the transport of such spin configuration with stable size under an applied current density of $J_s = 18.5 \times 10^8$ A cm^{-2}.

Because of this oscillation of the topological number, we have called the IST as the **resonant magnetic soliton (RMS)** hereafter. Since its average value of the topological number equals zero ($Q = 0$), there exists no skyrmion Hall effect, and the RMS moves along a straight line.

For a practical utilization in real devices of the proposed method, the density of RMS formation and their dipolar interaction between each other should be tested. For this matter, we propose a successive creation of RMS by applying a new series of current pulses, as presented in

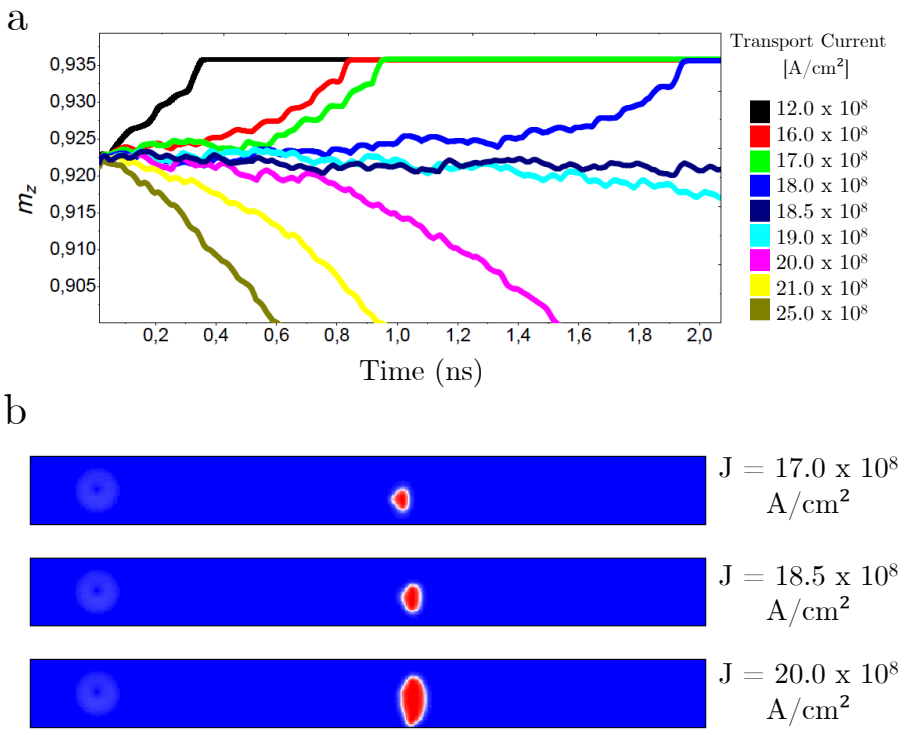

Figure 6.6: **a.** Time evolution of m_z of the structure moving along the track, for different values of current. m_z is stable for a certain magnitude of J **b.** Transport of the structure, after the current is reduced to $J_s = 18,5 \times 10^8$ A cm^{-2}, moving with stable size. For smaller currents, the structure vanishes and for higher currents, it turns into a DW pair.

Figure 6.7d. First, we create a RMS by applying the current J_c during 0.17 ns, same protocol for the single structure. Just after the creation of the first RMS, the applied current is switched off for 0.22 ns. This procedure is performed to quickly reduce the size of the first RMS for enough time to avoid the structure to disappear and assure that the successive application of the current J_c for the formation of a second RMS will restore the size of the first RMS to its original size. By turning off the current for more than 0.22 ns, the first structure will disappear and less than this time, the structure will remain big enough for, when the second pulse of J_c is applied, the first structure will grow and turn into a domain wall pair. By applying this protocol, we find a possible way to create a stable pair with similar size and a distance between each other of around $\sim$ 300 nm. Such a process can be observed along the evolution of m_z in Figure 6.7d. The motion of the pair was investigated throughout the nanotrack and some snapshots are presented in Figure 6.7e and the corresponding topological number Q of the nanotrack is given in Figure 6.7f.

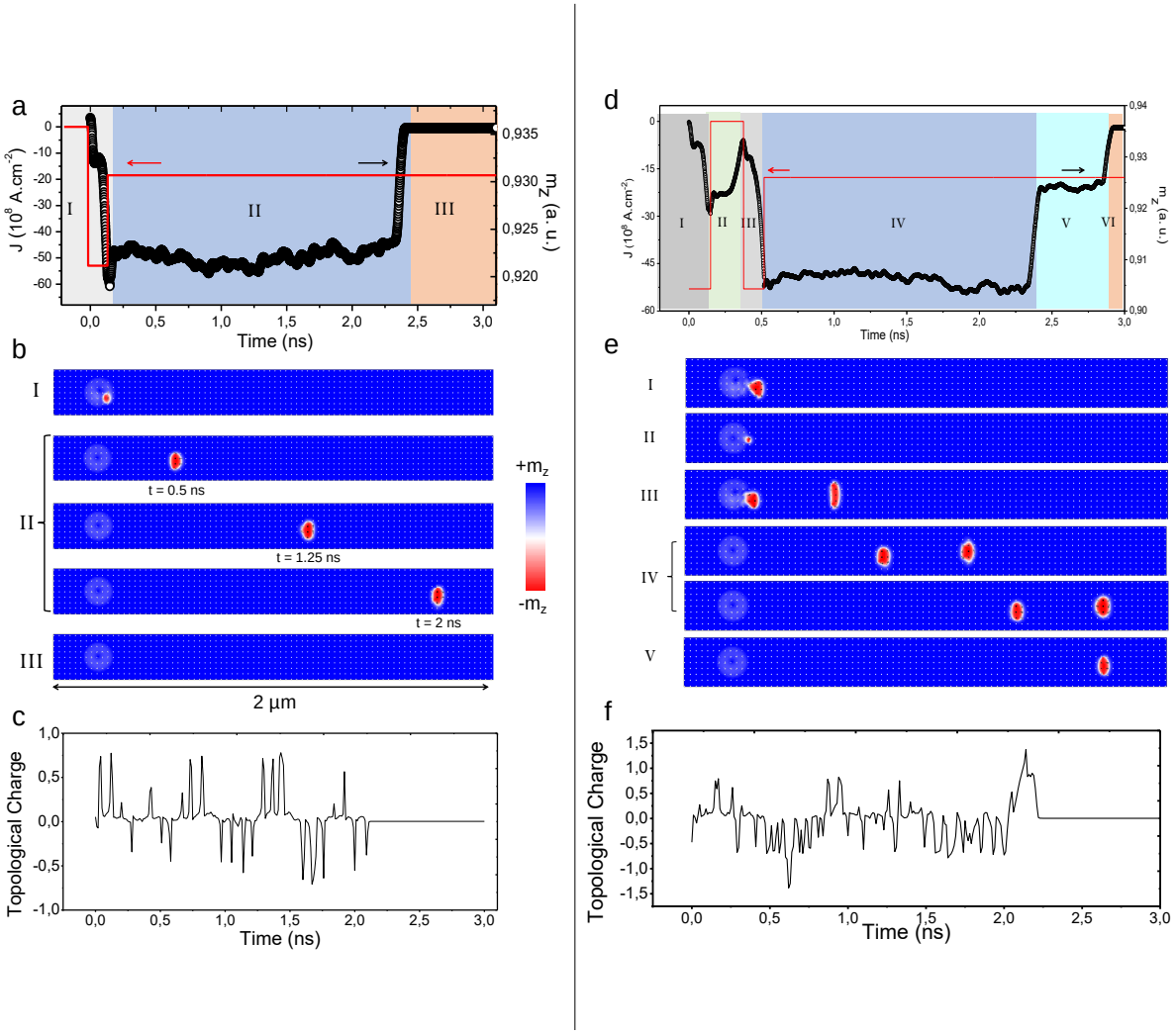

Figure 6.7: **a.** Time evolution of m_z (black) e J (red) during the creation and transport of a single RMS. **b.** Snapshots of the nanotrack during the transport of the RMS in certain time intervals with the creation (I), transport (II) and the moment when the structure reaches the racetrack end (III). **c.** Time evolution of the topological charge during the transport of the single structure. **d.** Time evolution of m_z (black) e J (red) during the creation and transport of multiple successive RMS. **e.** Snapshots of the nanotrack during the transport of the multiple RMS in certain during the successive creation and transport. **f.** Time evolution of the topological charge during the transport of the multiple structures.

To explore a detailed mechanism of the fluctuation of the topological number of a RMS we study the topological number Q showing a detailed time-evolution of the topological number in Figure 6.8 that fluctuates around $Q = 0$ and takes extrema around $Q = \pm 0.75$. In this process, the topological number $|Q|$ suddenly increases (II, III′) and reaches a maximum value (IV, V′). Then it decreases smoothly (V, VI′) and returns to be zero (VII, VII′).

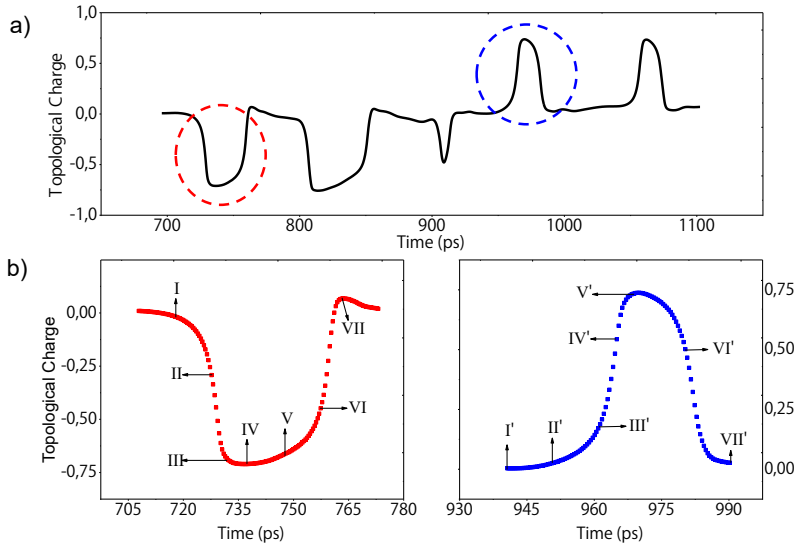

Figure 6.8: a. Topological number evolution during the transport of a RMS. **b.** shows the highlighted peaks of **a** with the minimum and maximum values of Q. The spin configuration for each peak are given in Figure 6.9.

We present snapshots of the topological number density and the corresponding spin configuration in Figure 6.9. Especially, the in-plane spin configuration contains a defect-like point at the snapshot time when the topological number takes a maximum value, where the contribution to the topological number is not strictly $Q = \pm 1$. Namely, when a defect-like point is almost formed but not completely, the soliton acquires the topological number $|Q| < 1$. We can see that the sudden change of the topological number is induced by the creation and the annihilation of a defect-like point.

In Figure 6.9, the topological number density for the RMS with $Q = 0$ is represented by blue and red colors, and is positive for the upper half (red), while it is negative for the lower half (blue) that represents the maximum positive and negative values respectively. We can see that, in Figure 6.9a, in the situation I, the average topological charge is close to zero (represented in the image by the same amount of blue and red). In the situation III we can notice the formation of a blue dot in the red area, which represents the increase in the norm of the topological number, which is due to formation or annihilation of a point-like defect in the structure, as shown in the in-plane spins distribution below. The RMS is not round, like a skyrmion, it is ellipse-shaped, elongated perpendicular to the applied current direction. A defect-like point emerges almost at the top or the bottom of the RMS.

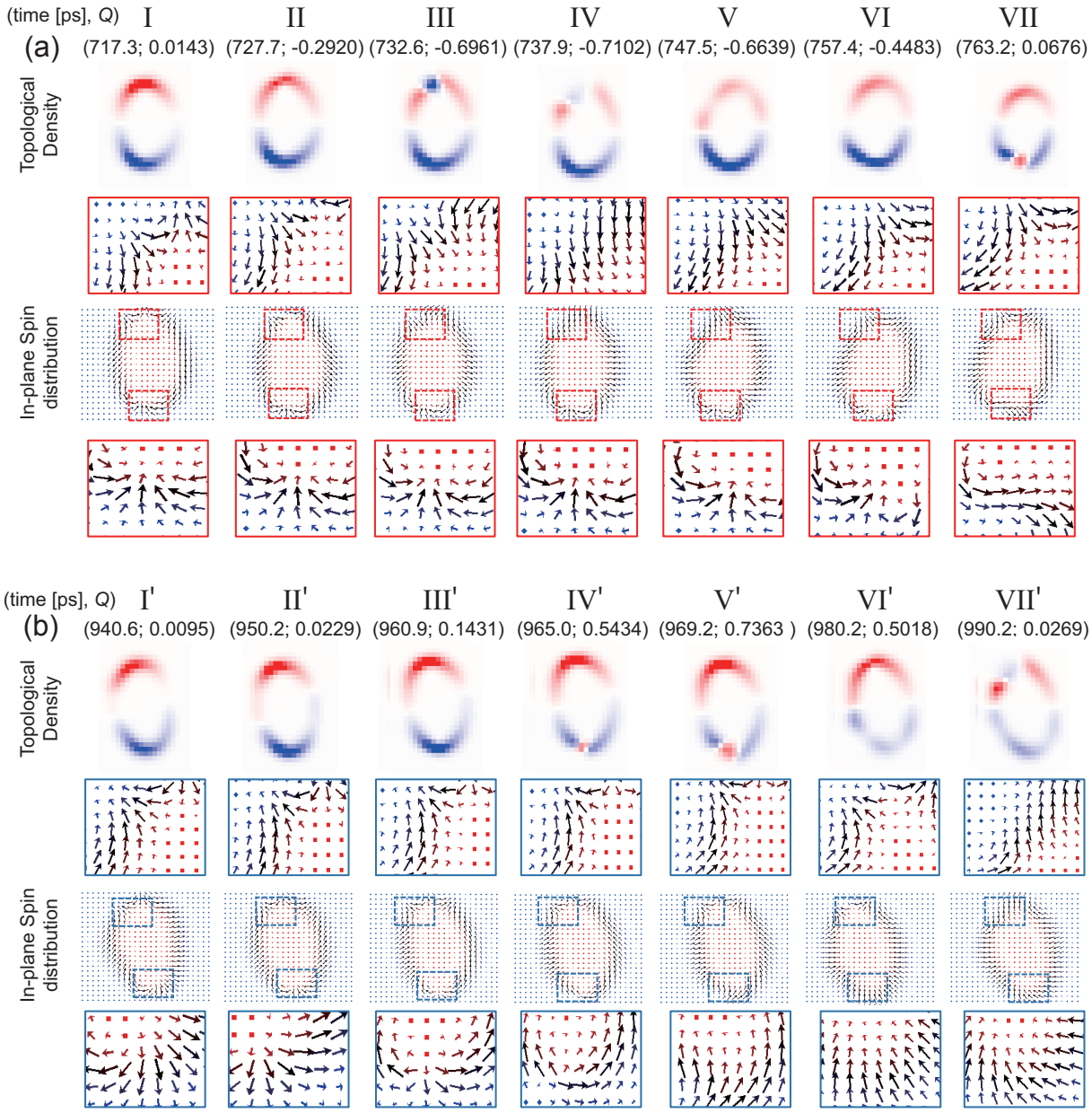

Figure 6.9: Spin configuration and topological number density for the **a.** minimum value of Q, as shown in Figure 6.8b and **b.** maximum value of Q, as shown in Figure 6.8c. The Roman numerals corresponds to its respective point in the graph, the time and the spin-component distribution $m_z(x)$ of each state is indexed by (t, Q).

This RMS is different from a traditional magnetic bubble because of the size of a RMS, that is much smaller than a traditional bubble [131, 132], which is stabilized by the magnetic dipole-dipole interaction and have a size in the order of μm. This magnetic dipole-dipole interaction does not play a main role for the stabilization of a RMS since its size around 100 nm. A RMS is stabilized only in the presence of the applied current, as we have shown before, if the current is turned off, the RMS shrinks until disappear, while a traditional magnetic bubble is stable even in the absence current. The topological number of a RMS oscillates as a function of time in a RMS, of which the average value is equal to zero. This is in contrast to a moving traditional magnetic

bubble, of which the topological number may vary but cannot have an average value of zero.

6.4 Detection

After the creation and transport of the RMS, the detection of the magnetic moving structure can be done by using a magnetic tunnel junction (MTJ) sensor [4, 133] to detect the passing RMS through the nanotrack, which consists in two magnetic layers separated for a thin oxide layer between them. This oxide is usually MgO or Al_2O_3, with thickness less than $5nm$.

We have inserted above the track, a CoPt nanodisk electrode with a diameter of 120 nm and thickness of 4 nm, made of the same material of the nanotrack (same simulation parameters for CoPt in the Table 6.1), 2 nm apart the track to simulate the average thickness of thin oxides used as tunnel barriers in MTJs.

It is important to investigate the interaction between the RMS and the MTJ electrode, which could pin, deform or destroy the RMS if the interaction is too strong. As shown in Figure 6.10, the effect of the RMS interaction with CoPt MTJ electrode is not strong enough to destroy the RMS. When the RMS is passing below the MTJ electrode, we can notice a very small reduction in the size of the RMS, represented by the positive slight increase in the m_z of the nanotrack (black curve of Figure 6.10b).

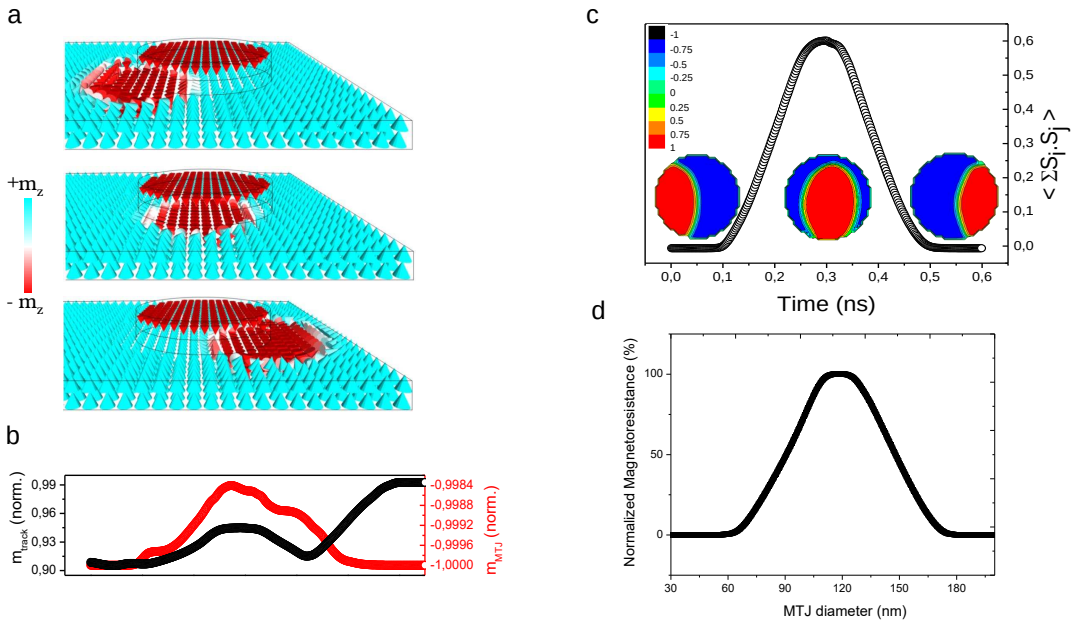

Figure 6.10: **a.** Images with three different times when the RMS passes through the MTJ electrode. **b.** Variations in m_z for the RMS and the track **c.** Estimated tunnel magnetoresistance for the junction, showing an approximate maximum value of 60%. **d.** The estimated value of TMR for different diameters of the MTJ electrode, with an optimal value of 120 nm.

The tunnel magnetoresistance (TMR) could be estimated as

$$T = \langle \sum \vec{S}_i \cdot \vec{S}_j \rangle^{-1} \tag{6.2}$$

We calculated scalar products of spins from each cell of both tunnel junction sides, using a $Fortran$ code (made in collaboration with Prof. Sidney G. Alves) that calculates the magnetization in each cell in the track and MTJ electrode, and sum all contributions according to Equation 6.2. The results are given in Figure 6.10c. Using the same diameter for the MTJ and nanodisk used in the RMS creation (120 nm), the highest tunnel magnetoresistance observed is about 60%. The insets show the snapshots of scalar products $\sum \vec{S}_i \cdot \vec{S}_j$ at selected times, where the red area shows the position of the moving RMS. The size of the MTJ electrode of 120 nm was chosen for having the best TMR relation, compared to electrodes from 30nm to 180 nm as shown in Figure 6.10d.

7 - Discussion and Perspectives

The proposal about the creation, transport and detection of magnetic solitons, stabilized by spin-polarized currents have shown to be, with the results obtained until now, a new possibility for aplication in racetrack devices, as previously proposed for domain walls [21] and skyrmions [118].

An advantage of this kind of system, is the higher transport velocity, compared to in plane DW devices [52], and simplicity, compared to skyrmion devices, since it does not require any external magnetic fields and Dzyaloshinskii-Moriya interaction. Another great advantage, is the fact that this device does not need a third electrode for the spin-polarized current application, as in [76].

For a practical realization of the device, since the RMS is not possible to stabilize without an electrical current, it may be difficult to apply this new feature in a practical device without a way to store data.

The conversion between skyrmions and domain walls have already been reported [119], in materials with PMA and DMI, by using a planar junction geometry, from a nanowire to the nanotrack, with difference in the width as in Figure 7.1. This conversion depends on the value of the electrical current and the width difference in the junction.

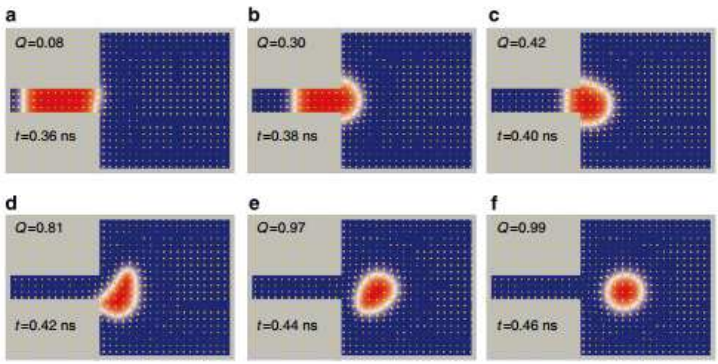

Figure 7.1: Skyrmion being created from a DW pair, driven by spin transfer torque from the narrow part to the wide part of the nanowire. Red and Blue colors shows m_z in opposite directions. Extracted from [119]

By following this idea, without DMI, our system can also be converted from a DW to a

RMS, without changing the current density used for transport the RMS. Figure 7.2 shows the conversion between the wider track to a narrower one and back to the wide track, where the first one is 200nm wide and the middle is varying sizes with different widths W. By passing through the junction of the two tracks, where there is an enlargement, the DW turns into a RMS.

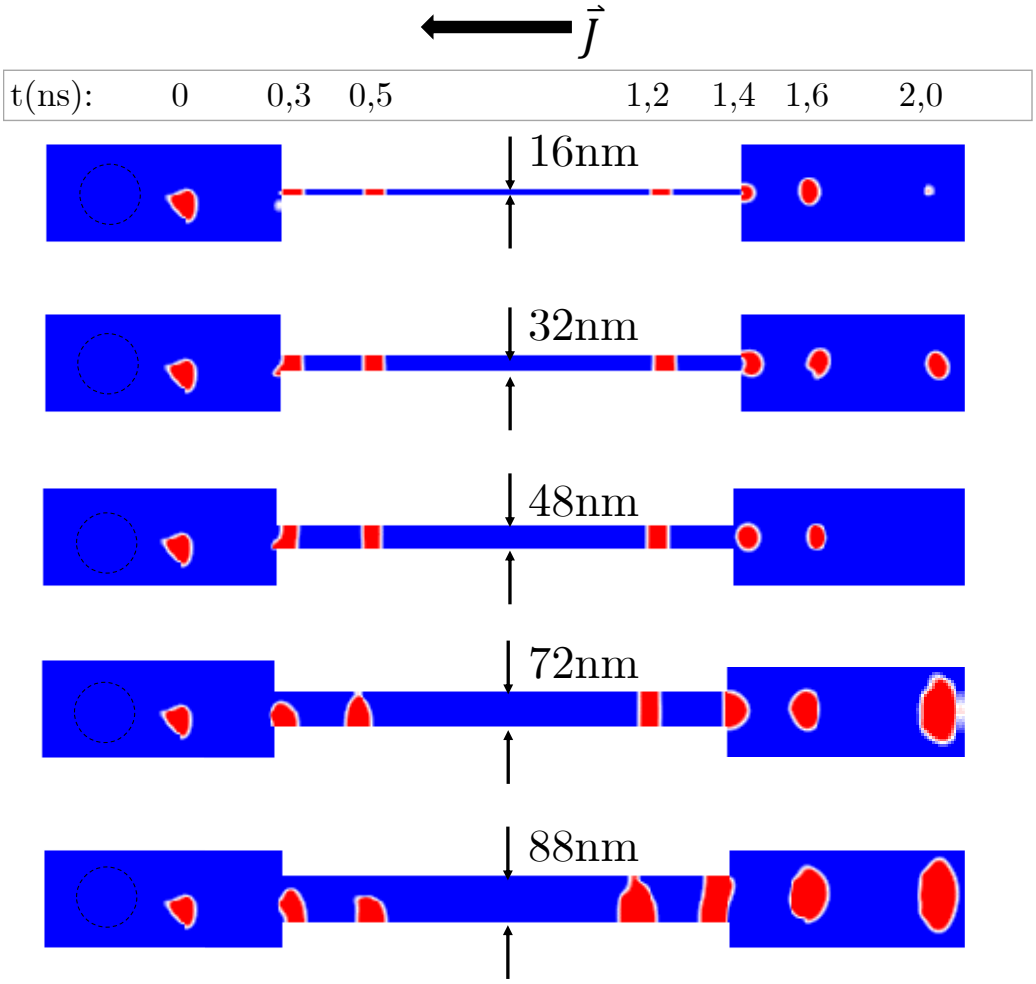

Figure 7.2: RMS - DW - RMS conversion by constriction with different sizes of W. The dashed lines indicates the diameter of the disk.

Further analysis on the movement and stability of the RMS are still necessary, once this structure can't be considered as a skyrmion, a bubble or a domain wall. Differently from skyrmions, the RMS is not round-shaped, being elongated similar do an ellipse with the major axis perpendicular to its velocity. From the analysis of m_x and m_y, the RMS evolves similarly to a domain wall pair in its major axis (Figure 7.3), but since it does not touch the borders, the DW pair join together and meet at some point at the top and bottom of the structure, leading to the formation of point-like defects, as shown in Figure 6.9. Those point like defects are also a promising further work, with a rigorous analysis to verify if they can be considered Bloch points as shown

in Figure 6.9 [134, 135].

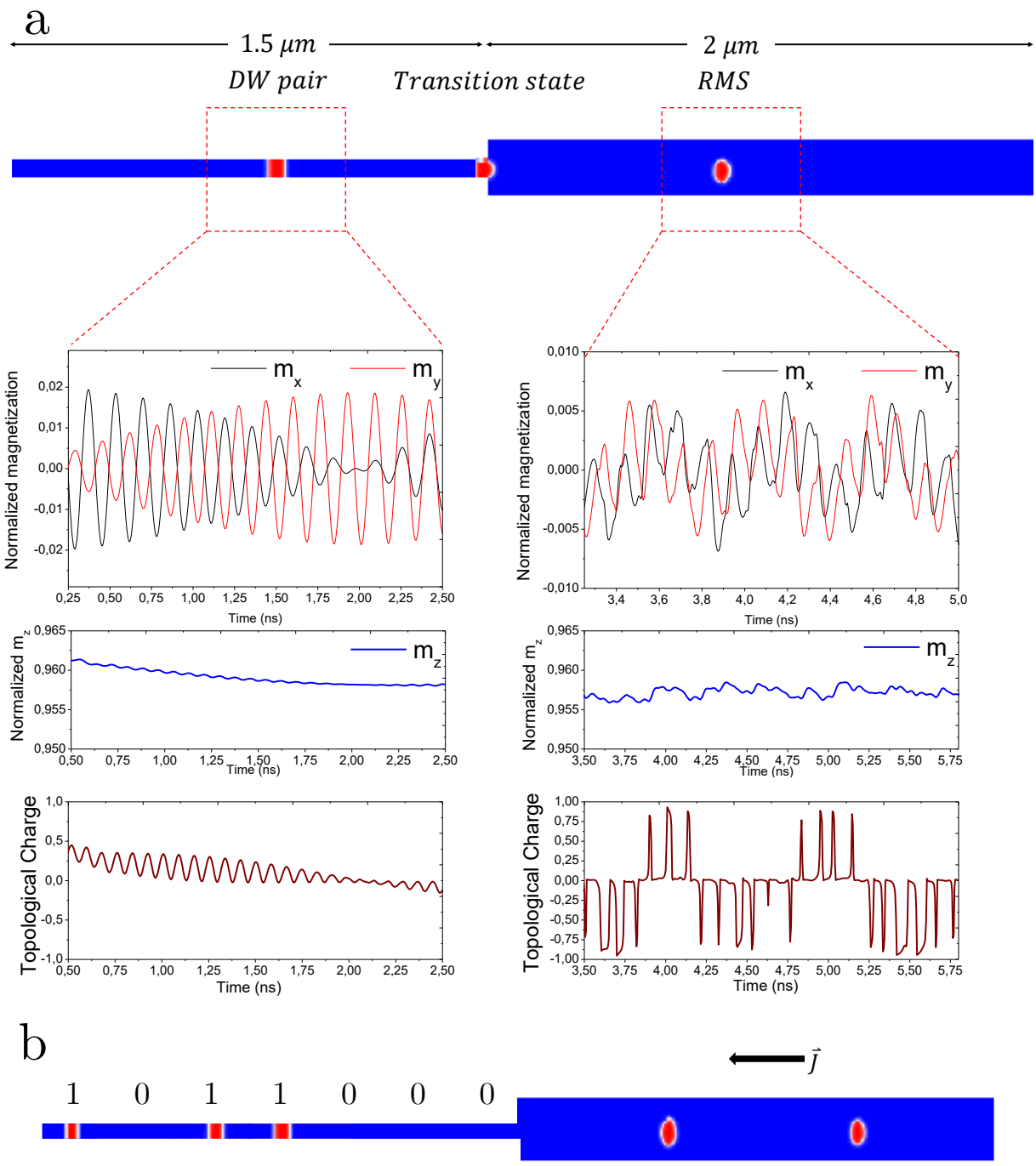

Figure 7.3: a. Conversion of a DW pair in RMS from a constriction with $J = 18,5 \times 10^8 Acm^{-2}$ showing the variation in the in-plane magnetization m_x and m_y, the variation of m_z, related to the domain between two consecutive DW pair size, that is stable in size and the RMS that shows small oscillations in size. **b.** Hybrid device with storage and transport configuration for a RMS racetrack device.

8 - Ongoing Works

8.1 Experimental Device

The following steps to the RMS study is the real device realization. For this, we need the correct PMA film to match the simulation parameters. Using Pt/Co multilayer, we have produced samples following the scheme described in Figure 8.1.

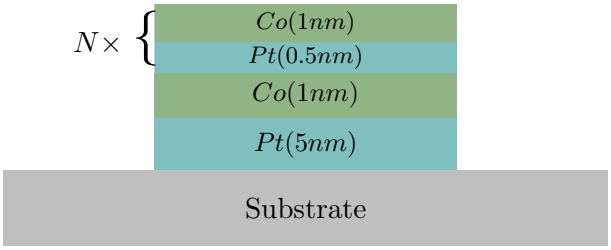

Figure 8.1: Multilayer deposition scheme for out-of-plane anisotropic samples.

In the samples produced so far, we have utilized Si, SiO_2 and MgO substrates. A $5nm$ layer of Platinum is deposited onto the susbtrate, as the heavy metal responsible for the spin-orbit effect. Over this layer, is deposited $1nm$ of Cobalt. The thickness of the magnetic material deposited on the metal layer is of major importance for the magnetization turn to easy-axis in plane or out-of-plane, since in this case, the effect is interfacial. Cobalt thickness lower than $1.3nm$ have predominantly perpendicular magnetic anisotropy [41].

For future specific measurements, the amount of magnetic material have to be enough to be detected and the anisotropy constant also can be controlled. Instead of using a bilayer of Pt/Co, multilayer can be intercalated without loss of PMA. In our work we have used $Pt(0,5nm)$ and $Co(1nm)$ N times (as shown in Figure 8.1) with N varying from 4 to 8. Some of this films were grown in a ultra-high vacuum ($\sim 10^{-10} torr$) sputtering chamber built at MIT [1]and some in collaboration at 'Centro Brasileiro de Pesquisas Físicas' (CBPF[2])

In both places, the Pt and Co were grown by the sputtering method where an Argon ions beam are accelerated through a target, with the desired material. Argon is utilized because

[1] moodera.mit.edu - Accessed in March, 1^{st}, 2018.
[2] www.cbpf.br - Accessed in March, 1^{st}, 2018.

it's inert, that means, it does not react with any materials forming another compounds. The atoms of the target are ripped off the target and travel in the ultra-high vacuum system to the substrate. The deposition rate is previously calibrated for some radio-frequency (RF) or DC power, depending on the system and the final thickness is determined by the deposition time. The substrate was previously cleaned with Acetone and Isopropyl alcohol in an ultrasonic bath to remove dust and organic residues. This substrate is then dried with nitrogen and loaded in the Load-Lock, when the main chambers are kept in ultra-high vacuum.

Hysteresis curves obtained with a Vibrating Sample Magnetometer (VSM), made in UFSC [3] are shown in Figure 8.2.

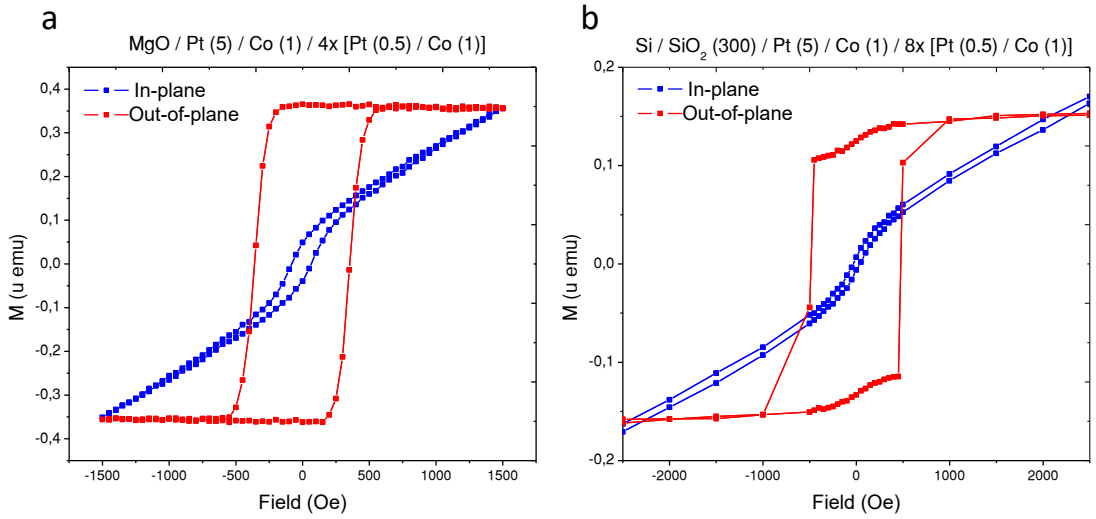

Figure 8.2: Hysteresis measured by VMS for some Pt/Co multilayer.

After grown, a nanolithography process will define the device. This step will be made in collaboration with International Iberian Nanotechnology Laboratory [4] (INL). The lithography process to define the structures is done by an electron beam and are described in Figure 8.3. A layer of Poly-methyl-methacrylate (PMMA), an electron sensitive polymer, is deposited onto the sample, by dropping a few amount of liquid PMMA and spinning at 4000 rpm for 1 minute to guarantee uniformity and a thickness of 500 nm. The sample is taken into a Field Emission Gun Scanning Electron Microscope (SEM-FEG) that is responsible to draw the structures with the electron beam in the PMMA. The resist is exposed to the electron beam where the exposed regions will be removed, for positive lithography. In these resists, exposure to the electron beam changes the chemical structure of the polymer so that it becomes more soluble in the developer.

[3] labcam.paginas.ufsc.br
[4] inl.int - Accessed in March, 1^{st}, 2018

The sample is placed into a bath in the developer solution, where the exposed areas leaves a window on the material. In the negative process of lithography, the resist becomes more difficult to dissolve in developer. The negative resist remains on the surface of the substrate where it is exposed, and the developer solution removes only the unexposed areas. More details on lithography process are described in chapter 16.

After the PMA layer deposition, a 20nm Cobalt film is deposited (Figure 8.3a) onto it and then it's covered with a negative resist layer. The 120 nm diameter nanodisks are lithographed and, after the process, the disk will remain (Figure 8.3b). The Cobalt film will be removed by ion-milling technique where a beam of Argon ions accelerated through the sample will remove the metallic film, leaving whatever is under the resist. After cleaning, the Cobalt disks will remain. The same process will be done to define the tracks (Figure 8.3d). For the detection structure (the MTJ) we will use a positive resist, aligned with the track, leaving a hole in the exposed area, where the oxide and the consecutive PMA layer will be deposited.

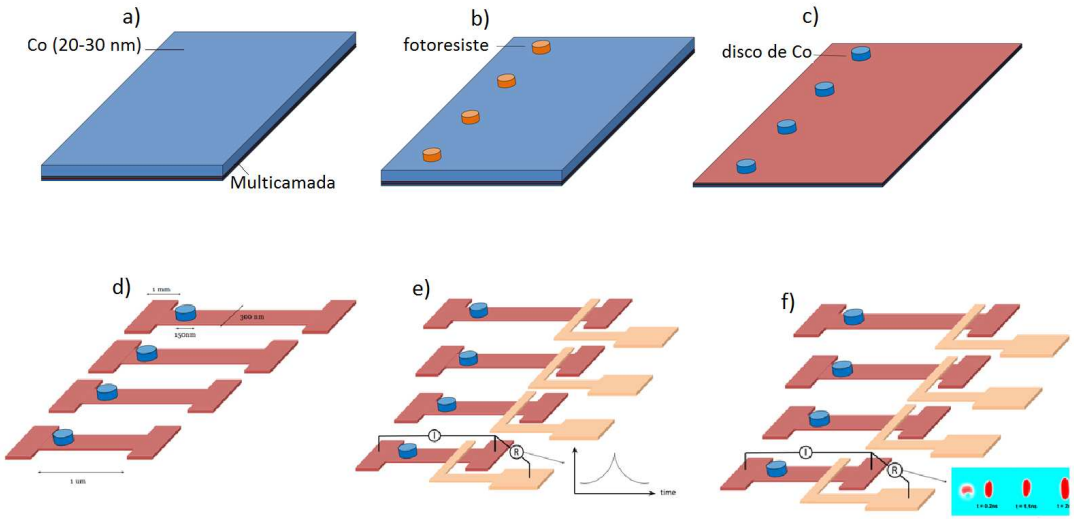

Figure 8.3: Lithography scheme procedure for the experimental device realization.

After fabrication, electrical measurements will be done at Labspin [5], at 'Universidade Federal de Viçosa', which can be done in a range of temperatures from 10K to 300K. A possible measurement for direct detection of the moving structure is the X-ray Magnetic Circular Dicrohism [136], with Photoelectron Emission Microscopy (PEEM) with temporal resolution of $10^{-9}s$, would be carried in collaboration with group of Prof. Stefan Eisebitt[6]. In this technique, the absorption of soft circularly polarized x-rays of the core level of atoms (L-band for Ni, Fe, and Co, for instance). The $2d$ level absorbs the radiation and the electrons are excited to the $3d$ level. The

[5] posfisicaaplicada.ufv.br/?page_id=81#SN. Accessed in March, 1^{st}, 2018.
[6] http://staff.mbi-berlin.de/eisebitt/

moment transferred to the photoelectrons is different if the circularly polarization of the x-rays is oriented right or left that results in a contrast in the intensity in the detector. More details on PEEM/XMCD process are described in chapter 16.

8.2 The TbCo alloy

To overcome the skyrmion hall effect present in systems with Dzyaloshinskii-Moriya interaction, (e.g. Pt/Co systems [137, 138]), other approaches with topological charge ± 1 can be investigated in ferrimagnetic systems, where dipolar interaction is almost zero as in some perpendicularly magnetized material that have been researched, like the Terbium-Cobalt alloy.

The anisotropy effect was first predicted by Néel in 1954 [139] and since then a variety of thin films with perpendicular magnetic anisotropy (PMA) has been developed to increase thermal stability for high density magnetic memory with perpendicular magnetic tunnel junctions (MTJ) [140–143], spin valves [144], and other physical effects observed in spintronic devices like spin orbit torque (SOT) [145–148] and spin transfer torque (STT) [149–151].

The most commonly known PMA materials and structures use ferromagnetic (FM) and heavy metals (HM) multilayers (*e.g.* Cr [152], Pd [153–155], Pt [156], Au [157]) and metal-oxides bilayers [158–161] with high spin-orbit interaction in the interface causing the PMA to vanish for larger FM layer thickness [41]. (Co,Fe)-Pt alloys [162, 163] and rare-earth (RE)/FM alloys [164,165] are also used for PMA due to the antiferromagnetically coupled $4f$ orbitals [144,166].

The focus on this work is the Terbium-Cobalt alloy, that shows a ferrimagnetic behavior and already have been reported to show bulk perpendicular magnetic anisotropy [167–169] in samples of around 20nm.

Here, we report perpendicular magnetic anisotropy in bulk Tb_xCo_{1-x} electrodeposited alloys with thickness of around 200 nm. Rare Earth (RE) Iron-group transition metals (TM) thin films obtained by this technique have already been reported before. [170]

8.2.1 Electrodeposition

The electrodeposition is a powerful and low cost technique for thin film deposition compared to the most usual deposition techniques as sputtering, chemical vapor deposition or physical vapor deposition since it does not requires high or ultra-high vacuum systems and can be performed at room temperature and pressure. [171]

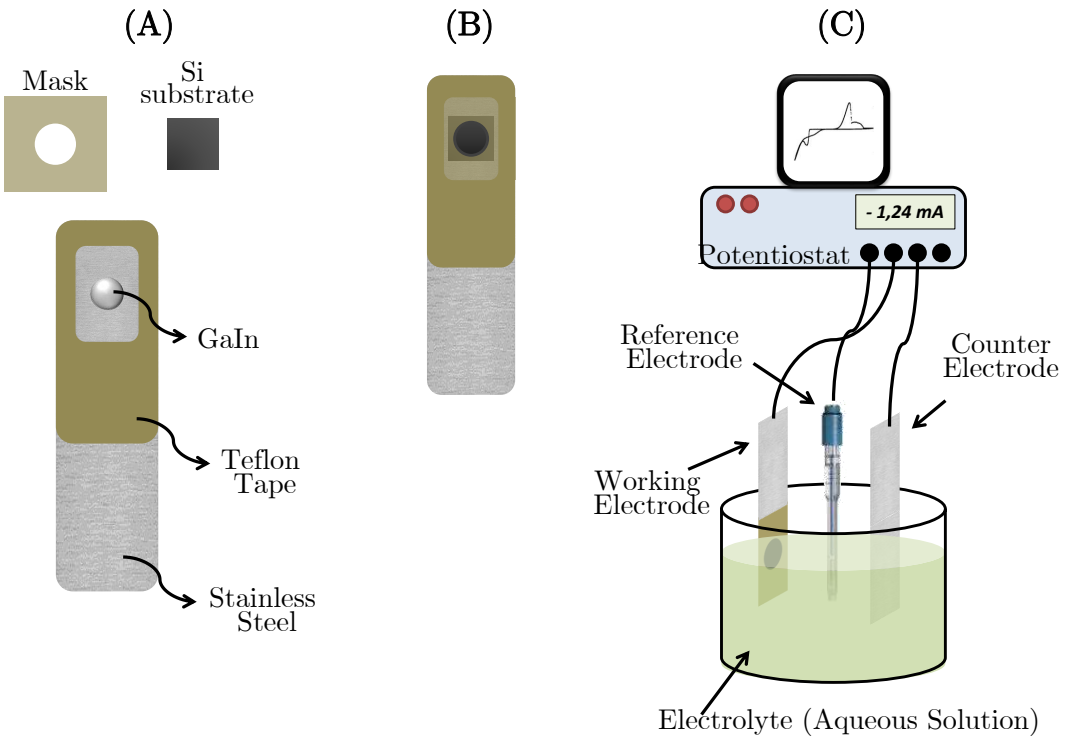

Figure 8.4: Electrochemical deposition technique setup. **a.** Components involved in the process for the working electrode. The silicon substrate will be held in the stainless steel plate by the mask and the electrical contact is done with Gallium-Indium alloy. The teflon tape (not the same for plumbing) is used to avoid contact between the electrode and the solution. **b.** Working Electrode mounted. The only conductive surface exposed to the solution is the silicon in the round opening in the mask. **c.** Technique mounting setup. The counter electrode is Platinum mounted on a stainless steel plate, insulated by teflon tape. Adapted with permission from [172]

The films were electrochemically deposited from a aqueous solution of

$$0.2M(TbCl_3 : 6H_2O) + 0.2M(CoSO_4 : 7H_2O) + 0.5M(H_3BO_3)$$

onto n-type (111) silicon with resistivity of 0.010 - 0.015 $\Omega \cdot cm$. H_2SO_4 was used in the solution to control and mantain the pH at 2.15 for stable co-depositions of Co and Tb [173]. The silicon is contacted in a stainless steel plate by applying a small amount of GaIn in the back of the substrate and serves as the working electrode in a standard three-electrode electrochemical cell, including a Pt counterelectrode (because Pt is inert) and a saturated calomel reference electrode. The schematic setup of the electrodeposition process can be found in the reference [174].

Cyclic voltammetry indicates the reduction potentials for Co at -1.28V and Tb at -2.05V. The potentiostatic electrodeposition method was used, by keeping the applied potential constant between electrodes, with the potentials varying from -1V to -2.9V. Here, we show the results for the samples of -1V, -1.5V, -1.6V, -1.7, -2.3V and -2.5V obtained after 30 seconds of depsition. For potentials more negative than -2.5V the deposition becomes unstable due to high rate of the

water electrolysis [173] and the samples show no magnetic behaviour.

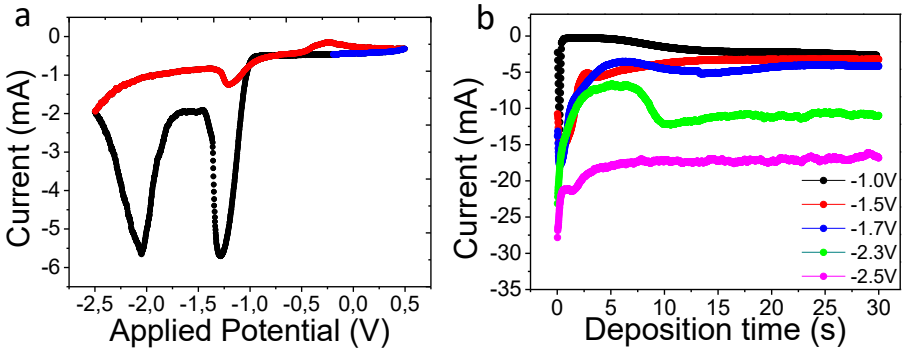

Figure 8.5: (a)Cyclic voltammetry for the electrolyte. (b) Current transients for deposition in some applied potentials.

8.2.2 Preliminary Results

Hysteresis curves for the TbCo alloy are shown in Figure 8.6 for different applied potentials and show both in plane and out-of-plane hysteresis curves. The most strong PMA behavior should occurs when the antiparallel RE and TM moments are nearly compensated. At room temperature, a compensation composition of x = 0.48 (which lies between -1.6 and -1.7 potential) was determined. Above this composition, the magnetization of the Co sublattice is larger than the Tb magnetization. Above the compensation point the resultant magnetization is determined by the Tb, so the alloy is called Tb dominant. Note that the out of plane saturation magnetization reaches a minimum at the compensation point.

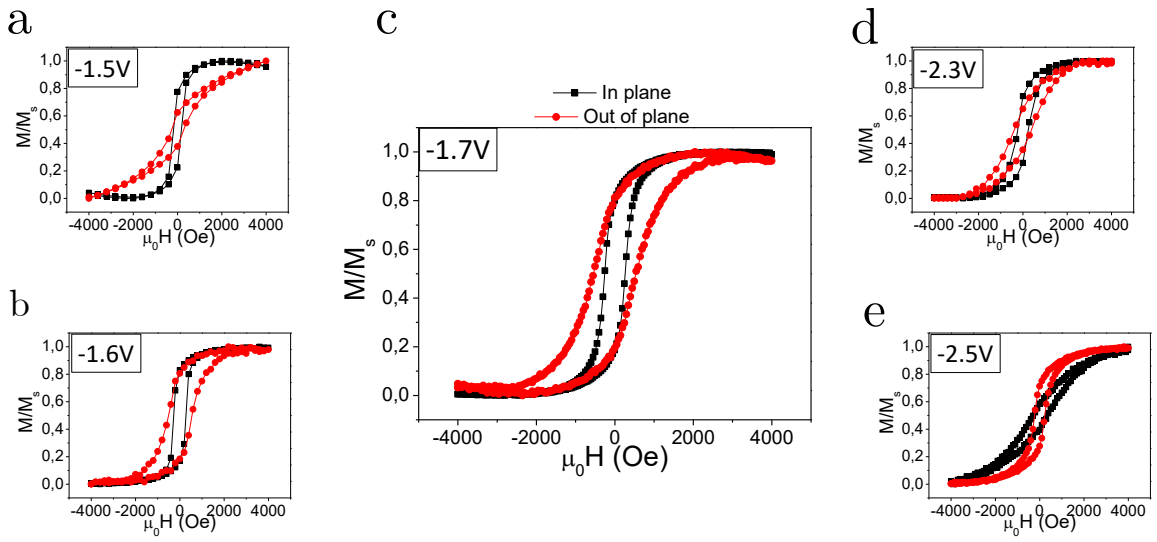

Figure 8.6: Normalized hysteresis curves for different electrodeposition potentials showing the in plane (IP) in black and out of plane (OOP) in red.

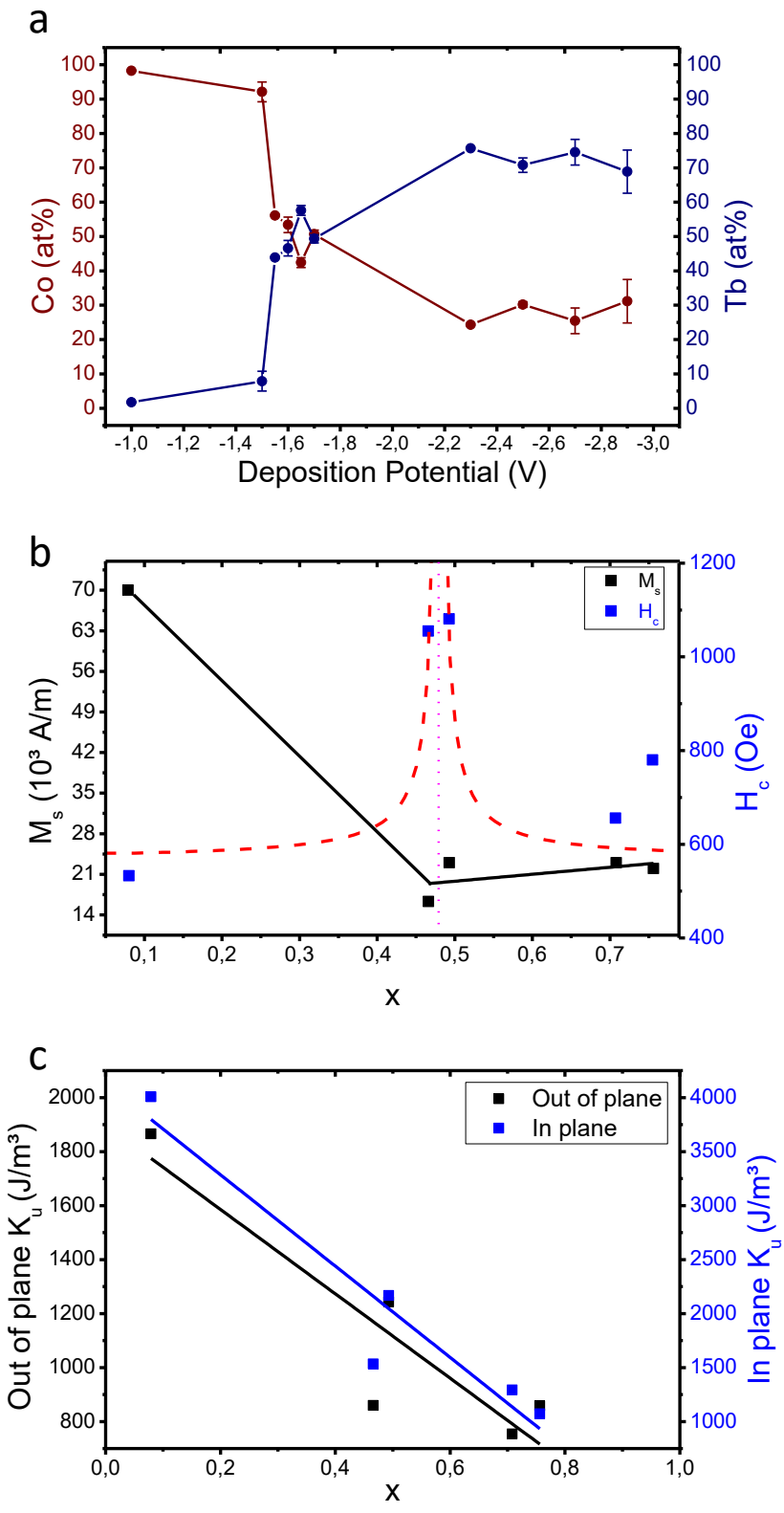

Figure 8.7: a. EDS analysis for the atomic concentration of Cobalt (red) and Terbium (blue) for some deposition potentials. **b.** Out of plane M_s and H_c dependence with Terbium concentration (x). The blue line is a guide to the eye where the compensation point lies in the Terbium concentration x=0.48. **c.** Out of plane (black) and In plane (blue) calculated anisotropy constant (K_u) in function of Terbium concentration.

This work is still under development, being those only preliminary results. More steps on this material still need to be done, with a more range of samples by investigating the magnetoresistance, spin orbit torque effects [169] and exchange bias [175] properties and optical magnetic switching [176, 177] of this kind of materials to determine their potential spintronic applications specially for applications in antiferromagnetic skyrmions [112, 124, 178, 179].

Part II

Spin to Charge Current Conversion in Topological Insulators

9 - Introduction

Efficient injection, transport and detection of spins are main questions to be focused in the development of spintronic devices. Spin-polarized currents plays an important role in spintronics, specially in the one we discussed in Part I. Nonvolatility, increased processing speed, less power consumption, and increased integration densities are the main advantages of those spin-based electronic devices. The search for new materials that exhibit large spin polarization of carriers include "half-metallics" ferromagnetic oxides and related compounds [180–182], half and full-Heusler alloys [183–187], binary oxides [188] and semiconductors [189–191].

Injection, transport and detection of spins or pure spin currents are also fields of high interest in the spintronics researches. A pure spin current is obtained by making electrons of opposite spins move in opposite directions or it can be carried by spin waves (magnons). In the past years, the discovery of a new class of materials increased the researches in the condensed matter physics. The topological insulators (TI) are materials that differ from regular insulators by having a energy gap different from zero in the bulk and a gapless edges or surface states, due to a non-trivial topology in the band structure. The research in TIs are limited by a few amounts of materials, as discussed below.

10 - A Brief Introduction on Topological Insulators

The band theory is a large theory about the electronic structure of solids. It is applicable to metals, semiconductors and insulators. From this theory, physical properties of solids, like thermal, elastic, magnetic and electrical properties can be described.

Considering an lone atom, the electrons are strongly bonded to the nucleus, being necessary a huge amount of energy to excite the electron from the inner shells to the most outer levels, this makes the atom electrically inert. In non-interagent atoms, like a monoatomic gas, the electrons occupy well defined levels according to the Pauli exclusion principle, where two electrons can't have the same set of atomic quantum numbers. Three of those numbers defines the level, the subshell and the electron spin. Each energy level can have two electrons with opposite spins.

When two atoms are far from each other, their 1s levels have two electrons with the same energy, when those atoms are close to each other to form a crystal, the position of the energy levels are strongly modified and the electron clouds of two consecutive atoms overlap and now the Pauli principle is valid not for those atoms separately and this 1 level split in two levels with slightly different energies.

The band theory explores the translational symmetry of a crystal (set of organized atoms). Similarly, when N atoms come together to form a solid crystal, each level of the free atom must split into N levels, because the Pauli principle now applies to the whole group of N atoms and the behaviour of this splitting is different for each level. These splitting covers an area called the permitted bands and the spacing between them are forbidden states. The difference in energy between a two permitted bands is called the band gap [192].

The band strucutre of a solid can be obtained by solving the Scrödinger equation with a periodic potencial $U(\vec{r})$ due to the symmetry of the crystalline lattice with the crystal moment $\vec{k}$. The Hamiltonian containing this potential is called the Bloch Hamiltonian and have its eigenstates (called Bloch eigenstates) defined in a crystal cell $\psi_k(\vec{r})$. The eigenvalues $E_{n,k}$ of the Bloch Hamiltonian are plane waves multiplied by an periodic funcion $u_{n,k}(\vec{r})$ and defines

the crystal band structure, where n is an index for each band level [193].

The term "band gap" in a solid refers to the energy difference between the top of the valence band (last filled level) and the bottom of the conduction band (first empty level). Electrons are able to make a transition from the valence to conduction band, or between bands below valence level, but it requires a specific minimum amount of energy for the transition, for an insulator, the gap energy is much higher than K_bT and for semiconductors, the gap is comparable to K_bT. In partially filled bands, the energy where higher occupied state lies is the Fermi level. At absolute zero, the electrons fill the lowest available energy states. The Fermi level is the limit of the highest occupied state at absolute zero where no electrons will have enough energy jump above this state. When the energy gap is zero or the valence and conduction bands overlap, the material is called a metal or a conductor.

During the XX century, theories on condensed matter physics were well explained by using concepts of spontaneous symmetry breaking, where quantum phases were described in terms of symmetry breaking and phase transitions occurs. For example, crystalline structures are related to translational symmetry, where the crystal lattice confines the possibilities of translation in determined values. In this case the interactions between atoms are translational invariants. Those phase transitions are described by the Ginzburg-Landau theory. Another example is the alignment in magnetic systems, where the ferromagmetic order comes from rotational symmetry breaking. Two insulators are said to be topologically equivalent if their respective Hamiltonians can be slowly transformed into one another, while maintaining a finite, non-zero energy gap [194].

In 1980 the existence of an order with states topologically different from the ones known until then was discovered [195]. The study of the quantum Hall effect has started a different classification based on topological characteristics of materials. The quantum Hall state does not break any symmetries, but it defines a topological phase where certain fundamental properties cannot change unless the system go through a quantum phase transition [194].

The integer quantum hall effect (QHE) occurs in electrons confined in two dimensions at low temperatures and experiencing high magnetic fields. This state is the simplest topologically ordered state. The field makes the electrons experience a perpendicular Lorentz force, which causes their motion to lie in a circle, rather the usual motion of electrons bound to an atom, causing an energy gap between the occupied and unoccupied states, like a regular insulator. At the boundaries, the electrons are in a different kind of motion, where the circular orbits can bounce off the edge, as shown in Figure 10.1b. These orbits in the boundaries lead to electronic states that propagate without quantized energies.

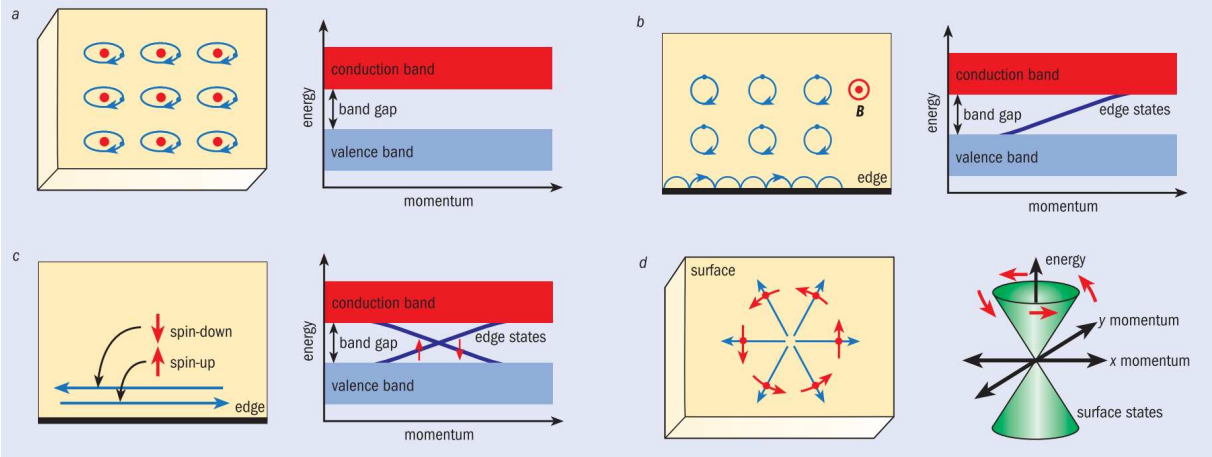

Figure 10.1: a. Regular insulator, represented by electrons moving bonded to its atom and characterized by an energy gap between valence and conduction bands. **b.** Integer Quantum Hall effect, where the orbits of the electrons are circular with frequency ω_c. At the edge, electrons execute "skipping orbit" as shown, ultimately leading to perfect conduction in one direction along the edge. **c.** The edge of the quantum spin Hall effect state or 2D topological insulator contains left-moving and right- moving modes that have opposite spins. **d.**The surface of a 3D topological insulator supports electronic motion in any direction along the surface, but the direction of the electron's motion uniquely determines its spin direction and vice versa. The 2D energy-momentum relation has a Dirac cone structure similar to that in graphene. Extracted from [196]

Since these border states can conduct and have no energy gap, they can conduct in a one-way flow making the electronic transport in the edge states "dissipationles" since there are no available states for backscattering and the electrons are immune to disorder. In this case, no electrons scatter and so no energy is lost leading to a precise quantized transport. This kind of transport is shown to be extremely useful for semiconductor devices, unfortunately, the requirement of a large magnetic field makes this effect less useful for potential applications.

The electrons are in a circular motion with cyclotron frequency ω_c leading to quantized Landau levels with energy $E_c = (m + 1/2)\hbar\omega_c$ (m is an integer). The Hall conductance in this case was found to be quantized due to an electric field that causes the electron orbits to drift, leading to a transverse conductance $\sigma_{xy} = ne/\hbar$, for n an integer number, different from the usual Hall conductance $\sigma_{xy_H} = j_x/E_y$. The quantization of the Hall conductance in QHE is due to a topological nature of σ_{xy}, a topological invariant and have been measured to 1 part in 10^9 [195].

The discovery of QHE was the first observation of topological phases, where phases of matter are not distinguished by broken symmetries as according to the Landau theory. Those phases differ from each other from a topological invariant $n \in \mathbb{Z}$ called the Chern invariant [194]. In the QHE the symmetry breaking is due to the external field and the Hall conductance is odd under the time-reversal symmetry. This Chern invariant term comes from a mathematical area of algebraic topology with many applications in the elementary particles physics and now in

condensed matter physics as well. The metallic states in the borders comes from this invariant number, in Figure 10.1b, considering the interface between the QHE material ($n = 1$) and the vacuum ($n = 0$), for the invariant number to change, there must be a metallic state between them, otherwise the invariant term cannot change from one material to another.

Since the QHE is not practical for real devices, specially at room temperature, besides, it requires strong fields and complex laboratory setups, the question that arises is if the QHE or any topologically non-trivial phases can be observed in time-reversal symmetrical systems.

Recent developments are based on spin orbit coupling (SOC), that causes electrons that are moving through a crystal to feel a spin-dependent force, even in non-magnetic materials [197], in simplified models introduced in around 2003 it can lead to a quantum spin Hall effect, in which electrons with opposite spins move in opposite directions. The spin-orbit coupling arises in atoms with a high atomic number, such as Platinum and Mercury, where the electrons move at relativistic speeds and feel a strong spin and momentum-dependent force similar to a magnetic field [196]. This analogy between spin-orbit coupling and the spin dependence on magnetic fields provides a way to understand the first 2D topological insulator, materials with the quantum spin Hall state. However, SOC allows a different topological class of insulating band structures when time reversal symmetry is not broken. To understanding this new topological class, that was predicted in 2005, there was a need to examine the role of this symmetry for spin 1/2 particles (the inclusion of spin) [198, 199].

The quantum spin Hall (QSH) phase is a time reversal invariant electronic state with a bulk band gap. This phase is associated with a Z_2 topological invariant, which distinguishes it from an ordinary insulator. The Z_2 classification is defined for time reversal invariant Hamiltonians, is analogous to the Chern number classification of the quantum Hall effect. A more detailed approach on the theory of topological invariants can be found in [200–202]

This new type of topological invariant could be computed for any 2D material and would allow the prediction of whether the material had a stable edge state or not [197].

As the effect of the SOC is different for opposite spins, each spin has an opposite sign of the Hall conductivity, and thus under an applied electric field the direction of the current will be opposite for each respective spin and considering two spins together, the total Hall conductivity is zero, but results in a non-zero spin current (Figure 10.1c), in other words, where spin up electrons propagate in one direction, spin down electrons propagate in the opposite direction.

The 2D topological insulator material, also called the QSH insulator, was first theoretically predicted by Bernevig, Hughes and Zhang in 2006 [203] with quantized charge conductance along the edges realized in HgTe/CdTe quantum wells (QW). The experimental signature of the

QSH phase in the HgTe/CdTe quantum well structures was given a year later [204] and showed a topologically trivial insulator state is realized when the thickness of the QW is less than a critical value. The topologically nontrivial state with a conductance close to $2e^2/\hbar$ is obtained when that thickness exceeds the critical value. In the topologically nontrivial state, there is a pair of edge states with opposite spins propagating in opposite directions. Transport measurements have confirmed the edge state transport, as predicted by theory in 2011 [205].

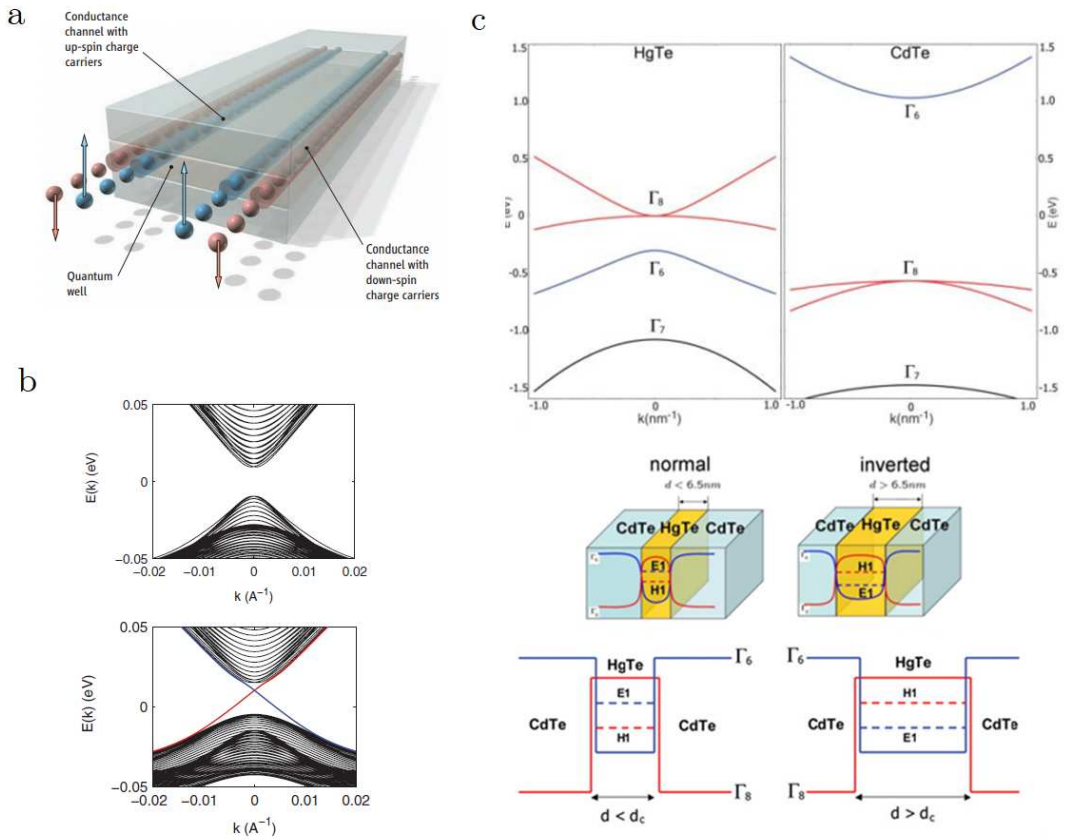

Figure 10.2: **a.**Schematic of the spin-polarized edge channels in a quantum spin Hall insulator. **b.** The energy spectra of the quantum wells. The thin quantum well has an insulating energy gap, but inside the gap in the thick quantum well are edge states, shown by red and blue lines. **c.**Band Structure for CdTe and HgTe in the QW and scheme showing the band inversion of the HgTe for values lower and higher than the critical distance value. Adapted from [203], [204] and [206].

Considering the bands in the Γ point of the Brillouin zone [32], close to the Fermi Level, we have for CdTe, the $s-$orbital band Γ_6 (conduction) and the $p-$orbital bands Γ_7 and Γ_8 (valence) separated by the SOC. This distribution can be briefly explained by the Hund's rules, where the lowest energy state for an electronic distribution is the higher spin state. In this case, on CdTe the Γ_7 and Γ_8 are the lowest energy, with lower energy with Γ_8 being the valence band and the gap energy ΔE being the difference $E_{\Gamma_6} - E_{\Gamma_8}$. The HgTe have the band configuration in the Figure 10.2 when placed between two CdTe layers. For the QW lower than a critical value, the

strong SOC of Hg makes Γ_6 and Γ_8 to be inverted [207].

The model Hamiltonian for the 2D topological insulator in QWs can also leads to generalization to three dimensions [208, 209], for a certain class of materials. The first topological insulator to be discovered was the $Bi_{1-x}Sb_x$ [210, 211] and the unusual surface bands of which were mapped in an angle-resolved photoemission spectroscopy (ARPES) experiments in which a high-energy photon is used to eject an electron from a crystal, and then the surface or bulk electronic structure is determined from the analysis of the momentum of the emitted electron.

The second generation of 3D topological insulators led to materials as Bi_2Se_3 [212], Bi_2Te_3 [213] and Sb_2Te_3 [214] which are well-known semi conductors with strong SOC and have a relatively large bulk energy gap allowing them to work at room temperature (0.3eV for Bi_2Se_3).

The known Bi-based compounds Bi_2X_3 (X = Se, Te) belongs to the class of thermoelectric materials with a rhombohedral crystal structure where unit cell contains five atoms organized in quintuple layers (QL) according to the Figure 10.3a.

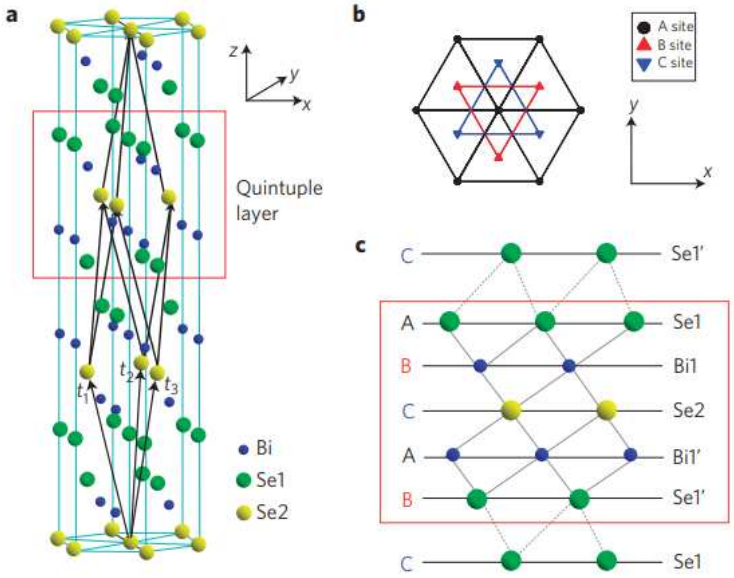

Figure 10.3: a. Crystal structure of Bi_2Se_3. A quintuple layer consists in $Se_1 - Bi - Se_2 - Bi - Se_1$ stack structure. **b.** Top view along the z-direction.The triangle lattice in one quintuple layer has three different positions, denoted as A, B and C. **c.** Side view of one quintuple layer structure. Along the z-direction. Extracted from [214]

This new generation of TIs, besides the possibility to work at room temperature have other advantages. The stoichiometric composition makes the fabrication easier, with a high-degree of purity. They also have a topological band structure more simple than the previous $Bi_{1-x}Sb_x$, the last one shows five Dirac-cones surface states, while the new class have only one and Bi_2Se_3 in special having a near idealized conical dispersion. The surface state of the next-generation topological insulators is closely related to the Dirac electronic structure of graphene [215], which

has a linear energy-momentum relationship like that of a relativistic particle (and is known as a Dirac cone) [197]. The effects of SOC are most evident in the region close to the Fermi level at the γ point of the Brillouin zone, which is indicative of a band inversion at this point.

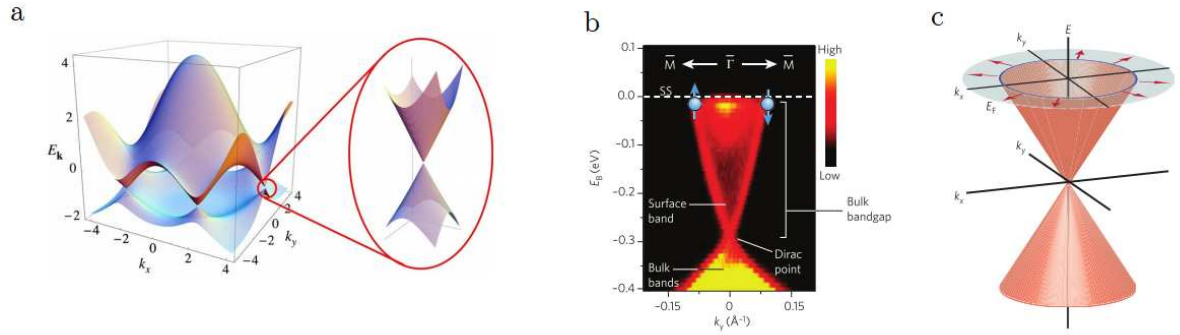

Figure 10.4: **a.** Electronic dispersion on graphene, with a zoom in of the energy bands close to one of the Dirac points. Extracted from [215]. **b.** ARPES measurement of Bi_2Se_3 band structure, The surface bands is a single Dirac point at the center of the Brillouin zone. **c.**Theoretical idealization of the electronic structure of Bi_2Se_3, showing the rotation of the spin degree of freedom (red arrows) as an electron (with energy E) moves around the Fermi surface. Extracted from [197]

11 - Methodology

11.1 Ferromagnetic Resonance and Spin Pumping

The Ferromagnetic Resonance (FMR) spectroscopy is a technique used to estimate the damping in a ferromagnet through the absorption of microwaves. The FMR can also provides information on the saturation magnetization, anisotropy fields and relaxation mechanisms.

The basis of FMR can be understand by analisys of the LLG equation (Equation 5.16). This equation is a nonlinear differential equation and describes the dynamics of the magnetization. This dynamics can be distinguished in small and large amplitude perturbations. Large perturbations occurs during magnetization reversal where the magnetization is oriented into an applied field direction. Small perturbations are related to spinwaves (Figure 11.1), with a well defined spatial correlation of the phase and amplitude of the magnetization fluctuation throughout the sample [216].

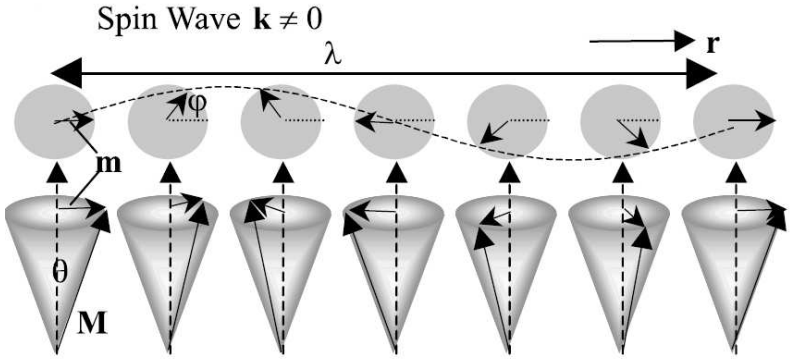

Figure 11.1: Illustration of a finite wavelength spinwave mode of wave vector k. Extracted from [216]

In the figure, θ is the angle between $\vec{M}$ and its static equilibrium position, and with constant θ, the phase ϕ of the transverse dynamic moment **m** oscillates spatially with the wavelength λ.

At static equilibrium, the magnetization position is due to the effective field H_{eff} which has contributions from exchange, anisotropy, dipolar fields and the external field. To induce a precession around this equilibrium position, a weak microwave pumping field is applied that employ a perturbative torque $\vec{M} \times \vec{h}_{mw}$ on the magnetization. The effective field will exert a

torque $\vec{M} \times \vec{H}_{eff}$ as a consequence. The effect in the magnetization is a precessional motion to the restoring force, rather than realigning into its equilibrium position. For a short excitation, the magnetization would spiral in, as a result of damping. When the frequency of the field is the same as the frequency of the magnetization precession, a resonance absorption occurs. This frequency precession is determined by all restoring torques coming from the static effective field as well as additional dynamic torques [216].

This absorption can be measured by FMR spectrometer. The scheme is described in ??. The microwave radiation is coupled via a wave-guide into a cavity placed between an electromagnet. The sample is placed in a region of a maximum of the magnetic field and zero electric field and it is under influence of the external field and the microwave field, perpendicular to each other. This distribution obeys the Maxwell laws and the boundary conditions of the walls of the cavity, where the fields reflections are treated stationary waves (Figure 11.2b-c). In a typical experiment, the microwave frequency f is held constant, and the applied bias field is changed. When the resonance condition is fulfilled, the wave is absorbed by the sample from the microwave radiation. This happens when the external field coincide with the resonant field for a certain microwave frequency.

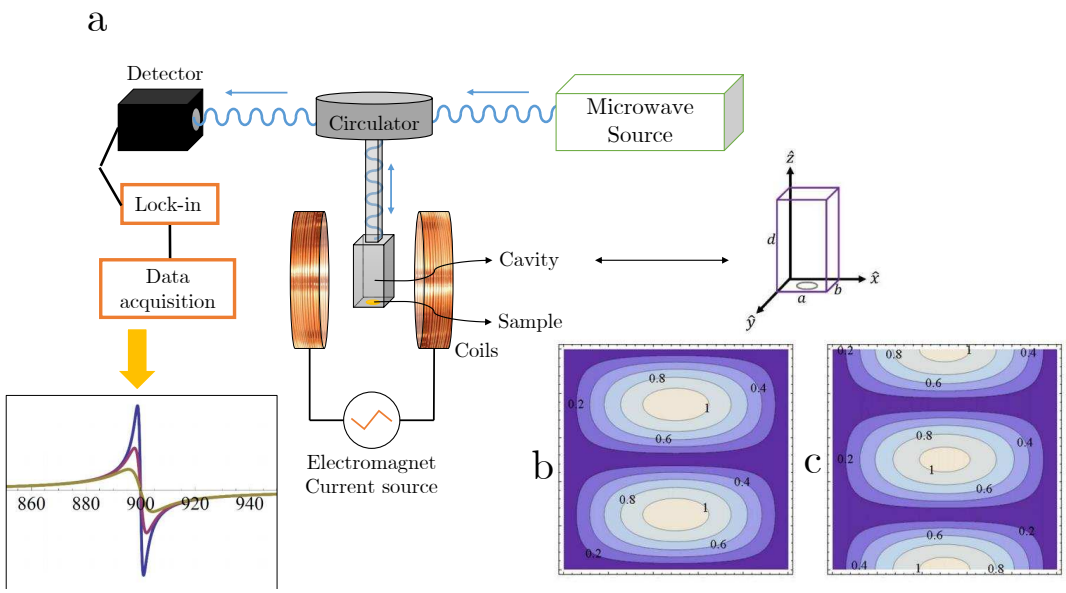

Figure 11.2: a. Schematic diagram of a typical FMR spectrometer. **b.** Electric field and **c.** Magnetic field distribution inside the cavity. Blue color represents zero field and white represents maximum field. Adapted from [217].

The graph on the Figure 11.2a shows the derivative of the absorption peak for FMR measurements. In many experiments, the angle between the sample and the direction of the applied field is varied, from which the angular dependence of the resonance field H_{res} and of the absorption linewidth ΔH can be obtained and used to extract the sample anisotropies, exchange

coupling between layers, as well as other magnetic information [216].

The efficient injection and detection of charge carriers with a controllable spin polarization orientation into nonmagnetic materials, is essential to the successful performance of a wide range of potential spintronics devices. The most usual methods for spin injection include the electrically driven spin injection (by electric current), thermally driven spin current (by heat current) and spin pumping (by spinwaves or magnons).

The spin Hall effect (SHE) is an analog to the usual Hall effect, discovered in 1879 by Edwin Hall [218], where an external magnetic field changes the charge distribution on a conductor by acting on the charge carriers. In the SHE there is an accumulation of electric charge carriers on the sides of an conductor, due to the Lorentz force, when an electrical current passes through an external magnetic field. In the SHE, there is an accumulation of opposite spins in opposite sides, but the magnetic field is not necessary in this case, being replaced by the spin-orbit coupling.

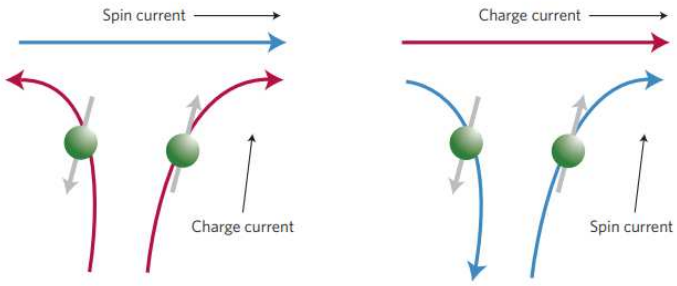

Figure 11.3: a. Spin hall effect and **b.** Inverse spin hall effect, where the longitudinal charge current is converted into the transverse spin current and vice versa. Extracted from [219].

The Spin Pumping (SP) [220] effect consists is a method to the generation of pure spin currents from precessing the magnetization $\vec{M}$ of a ferromagnetic layer injecting (or "pumping") the spin current into a paramagnetic layer in an FMR condition by the transference of angular momentum from the magnetic layer to the conduction electrons. This effect have already been reported in metallic multilayers [221, 222] and magnetic insulators (like Yttrium Iron Garnet [223, 224]). The detection of those spin currents can be made by the (Inverse) Spin Hall Effect, or by measuring for example, the precession on a second magnetic layer. A detailed approach on the (inverse) spin Hall effect can be found in [225–227].

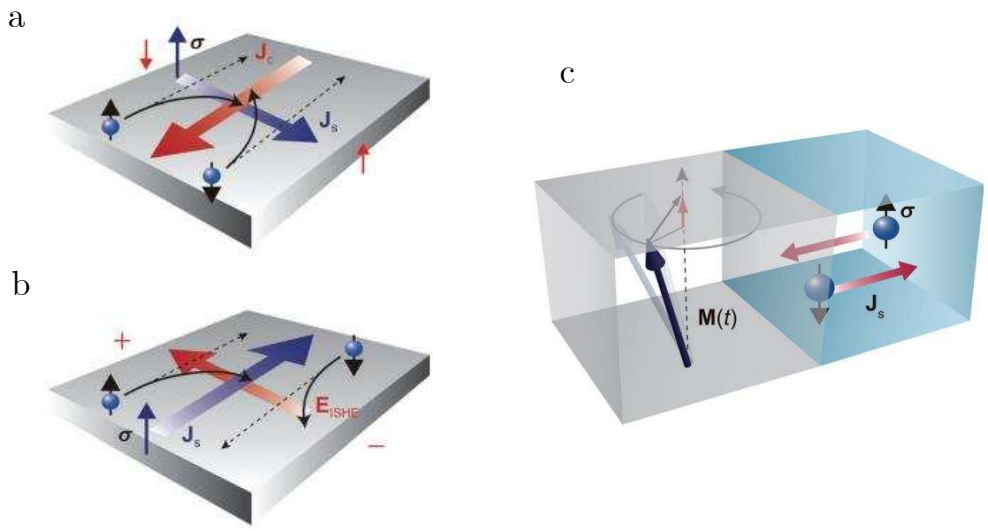

Figure 11.4: a. A schematic illustration of the direct spin-Hall effect. J_c, J_s, and σ denote a charge current, the spatial direction of a spin current, and the spin-polarization vector of the spin current, respectively. **b.** A schematic illustration of the inverse spin-Hall effect. E_{ISHE}, J_s, and σ denote the electromotive force due to the inverse spin-Hall effect, the spatial direction of a spin current, and the spin-polarization vector of the spin current, respectively. **c.** A schematic illustration of the spin pumping. $\vec{M}(t)$ is the magnetization. Extracted from [228].

11.2 Spin-seebeck Effect

In the spin Hall effect (SHE), a charge current driven by a voltage gradient can generate a transverse spin current. In the Seebeck effect (SSE), a temperature gradient can also generate a spin currents. The discovery of this phenomenon opened a new field of study called "spin-caloritronics".

The Seebeck effect consists in the direct conversion of a temperature gradient applied to the sample into an electric voltage difference. This effect can be used to generate electricity (thermoelectric generators), measure temperatures (thermocouples) or change the temperature of objects (Peltier module).

In 2008, Uchida *et. al.* [229] demonstrated that a spin current can be injected from a ferromagnetic film under a temperature gradient into a nonmagnetic metal, where a μV signal could me measured for a temperature difference of 21K. In the following years, the SSE could also be observed in Co_2MnSi Heusler alloy [230], GaMnAs ferrromagnetic semiconductors [231], $LaY_2Fe_5O_12$ ferromagnetic insulators [232] and (Pt,Au)/YIG [233].

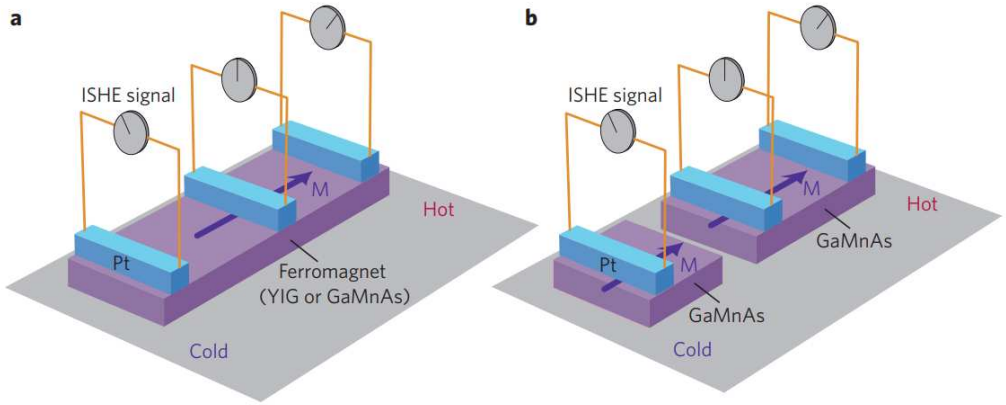

Figure 11.5: **a.** Experimental set-up of the SSE where a temperature gradient is set along a strip of ferromagnetic material (YIG or GaMnAs, in this case) and a voltage is measured across platinum bars placed perpendicular to the temperature gradient across the strip. The measured voltage is due to the inverse spin Hall effect (ISHE), which measures the spin accumulation below the platinum strip. **b.** Same experiment now with the ferromagnetic strip non continuous; the observed spin accumulation along the strip remains unaffected by the cut, suggesting that the origin of the effect cannot be due to charge-particle diffusion. Extracted from [234].

The detection of the injected current by SSE can be made by inverse spin Hall effect (ISHE) where the generated spin current is detected in the Pt strip placed across the FM material. The measured electromotive force $\vec{E}_{\text{ISHE}} = D_{\text{ISHE}} \vec{J}_s \times \vec{\sigma}$, where D_{ISHE} is the ISHE efficiency, which is higher in heavy metals, like Pt; $\vec{J}_s$ is the pure spin current density diffusing into the Pt strip, and $\vec{\sigma}$ is the spin direction. The spin Seebeck effect is caused by a nonequilibrium between the magnon system in the ferromagnet and the conduction electron system in the nonmagnetic metal. The explanation why spin currents can be carried by magnon excitations is because the conduction electrons short spin-flip diffusion length (which is a few nanometers in a NiFe alloy) fails to explain the long length scale (several millimeters) observed in experiments [235].

11.3 Sample Preparation

The topological insulator (TI) thin film growth was performed using a custom-built ultra-high vacuum molecular beam epitaxy (MBE) system at the MIT Francis Bitter Magnet Lab, at Moodera group laboratories. The substrate is an insulating heat-treated sapphire (0001) and has been outgassed at 800°C for an hour before the deposition. The Bi, Sb and Te were evaporated from Knudsen effusion cells using high purity Bi(99.999%), Sb(99.9999%) and Te (99.9999%). During the growth, the substrate was maintained at 230 °C.

To reduce Te vacancies, the growth is kept in Te-rich condition (the flux ratio of Te per (Bi +Sb) was set to approximately $\approx$ 10). The Bi, Sb and Te concentrations in the films were determined by their ratio, obtained in situ during growth using properly calibrated quartz crystal

monitors. The growth rate for the TI films was ≈0.2 quintuple layers (QLs) per minute.

Following the growth, the TI films were annealed at 230°C for 30 minutes to improve the crystal quality before being cooled down to room temperature. To avoid possible contamination, a 3-nm thick epitaxial Te capping layer was deposited at room temperature on top of the TI films before taking the samples out of the MBE chamber for the device fabrications.

The TI quality can be observed in Reflection High Energy Electron Diffraction (RHEED) in-situ measurements right after the growth and X-ray Diffraction (XRD) using a Bruker D8 Discover Diffractometer equipped with the Cu K_α radiation ($\lambda = 1.5418$Å). The XRD diffraction patterns indicates that the reflections are only from (00l) family of planes of $(Bi_{0.22}Sb_{0.78})_2Te_3$, as shown in Figure 11.6.

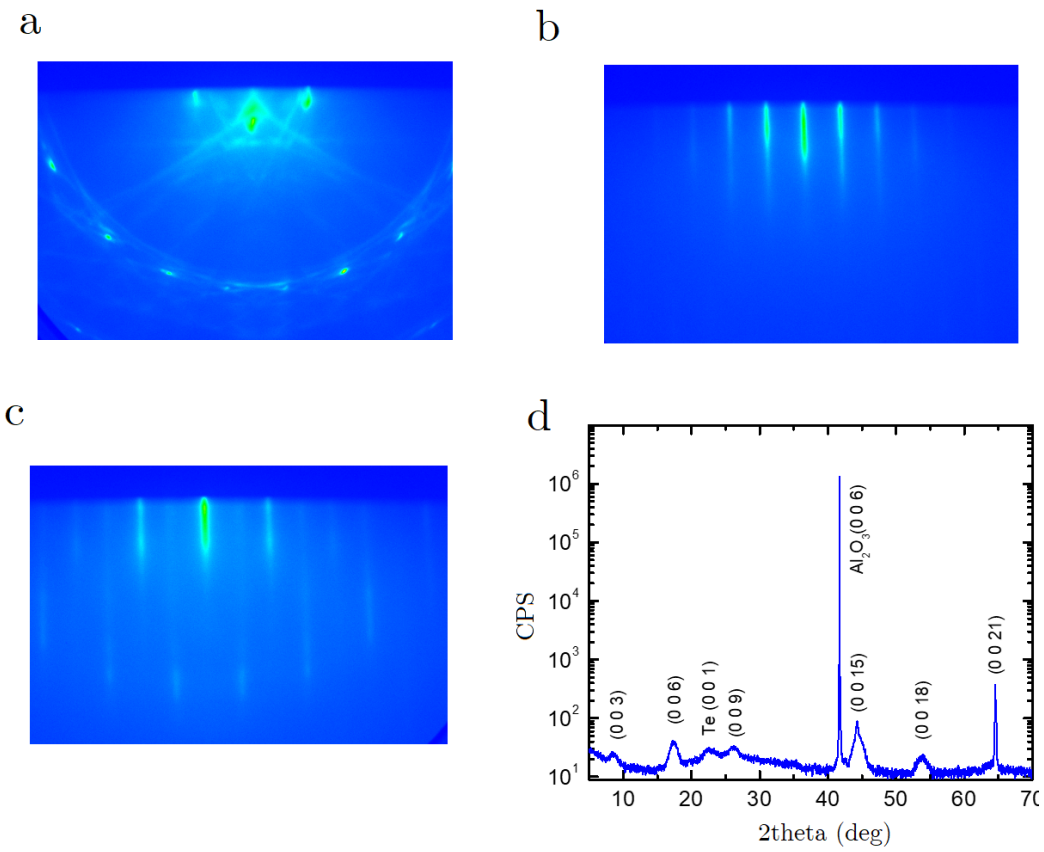

Figure 11.6: RHEED patterns of the **a.** sapphire (0001), **b** and **c.** 6QL $(BiSb)_2Te_3$ in two different directions. **d.** XRD pattern of the sample.

For the Spin Pumping and Spin-Seebeck measurements, the schematics of the built devices are respectively presented in Figure 11.7. The Permalloy (Py) layer, composed of $Ni_{81}Fe_{19}$, is deposited by DC magnetron sputtering, either directly on the TI film or separated by an insulating NiO layer, grown by RF sputtering at 160 °. The Py and NiO films were deposited in a 3 mTorr Argon atmosphere with deposition rates of 1 and 0.3 Å/s, respectively. Finally, two Silver electrodes were attached at the ends of the TI layer for measuring the induced voltages.

By using a shadow mask, the Py layer covers only the central part of the TI surface, then the Silver electrodes can be attached to the edges of the NM layer .

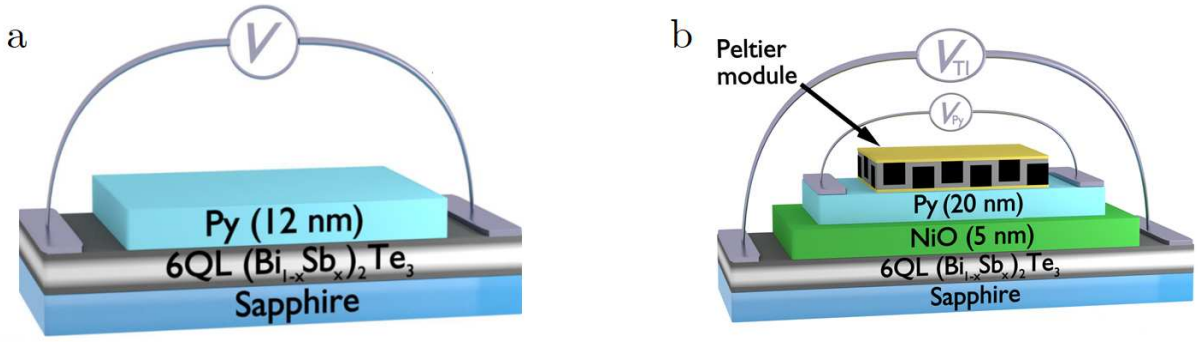

Figure 11.7: a. Spin Pumping device. **b.** Spin-Seebeck device.

The samples were fabricated at Moodera's lab, at MIT and the Spin Pumping and Spin-Seebeck measurements were taken at Sergio Rezende and Antonio Azevedo laboratory at Universidade Federal de Pernambuco.

12 - Results

Here, we have chosen x=0.78 because with this concentration the bulk $(Bi_{1-x}Sb_x)_2Te_3$ has a Fermi level close to the Dirac point [236–238] and 6QL thickness was chosen because of the 2D to 3D limit of the TI [239]. The Py films grown on top of TI have in-plane magnetization, and thus the magnetic proximity effect is expected to shift the Dirac cone in the momentum direction, preserving the Dirac cone without opening any energy gap [240].

12.1 Spin Pumping Results

From the device shown in Figure 11.7a, the FMR absorption spectrum of the Py layer in contact with the TI film was measured with microwave power of 24 mW. The FMR resonant field (H_r) of 1kOe is in agreement with the Kittel relation:

$$(\omega/\gamma)^2 = H_r\,(H_r + 4\pi M_s) \tag{12.1}$$

where ω is the microwave frequency, γ is the gyromagnetic ratio, M_s is the permalloy saturation magnetization.

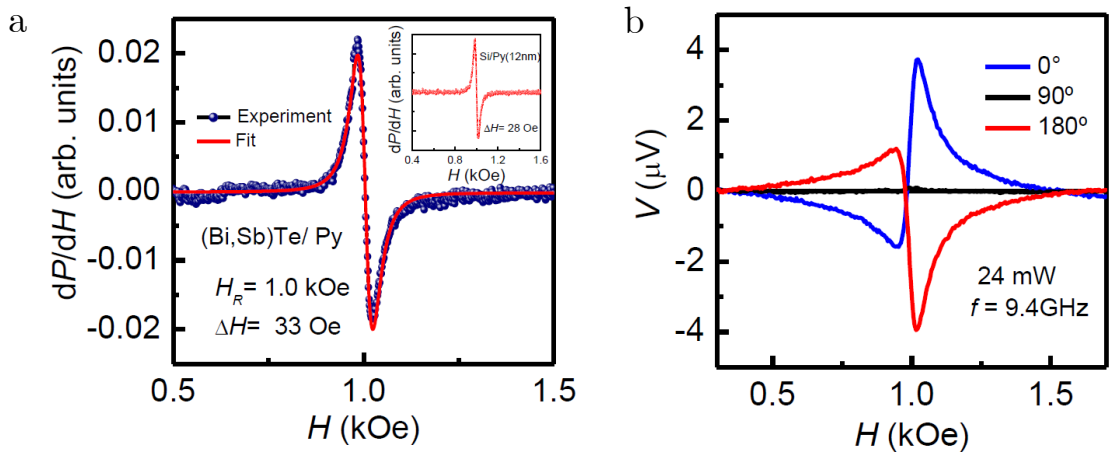

Figure 12.1: a. FMR absorption derivative versus magnetic field H measured at 9.4 GHz and microwave power of 24 mW. Inset shows the FMR spectrum for a single Py (12 nm) layer on a Si substrate. **b.** Voltage measured between the electrodes for three angles of the in-plane field, with the same microwave frequency and power as in **a**

The FMR line has the shape of a Lorentzian derivative of the microwave absorption dP/dH with peak-to-peak linewidth of 38.1 Oe, corresponding to a half-width at half-maximum (HWHM) linewidth of ΔH = 33.0 Oe. A single Permalloy layer, similar to the one used on top of TI, deposited alone on a silicon substrate, shows a linewidth ΔH_{Py} = 28.0 Oe (inset of Figure 12.1a). The difference in FMR linewidth indicates a increase of the damping due to the spin pumping in the Py layer [221] similar to Pt/Py bilayers [241, 242].

Figure 12.1b shows the dc voltage, measured directly with a nano-voltmeter, dependence with magnetic field ($\vec{H}$) scan. The voltage was measured by connecting Copper wires to the Silver electrodes, for a microwave power of 24 mW, for three angles of the in-plane field (as described in Figure 12.2a). The voltage lineshape is the superposition of symmetric and antisymmetric components, and it changes sign with inversion of the field, and vanishes for the field along the sample strip ($\phi = 90°$).

The line shape of V(H) varies strongly with the angle ϕ between the field $\vec{H}$ and the sample axis $\hat{z}'$. Depending on the angle, the line shape is a superposition of absorptive and dispersive curves, and we can observe a huge increase in the dc voltage along the sample at the FMR position. The single Py sample is not affected by spin pumping and show a voltage signal that is purely antisymmetric with respect to the FMR position. The measured voltage due to the ISHE depends on the angle ϕ and thus must be symmetric with respect to the FMR position. V(H) have an asymmetric shape because of two contributions, anisotropic magnetoresistance and spin pumping having both symmetric and antisymmetric components with these contributions having different symmetries with respect to $\vec{H}$. The origin of the anisotropic magnetoresistance is the classical induction effect due to the in-plane microwave magnetic field [242].

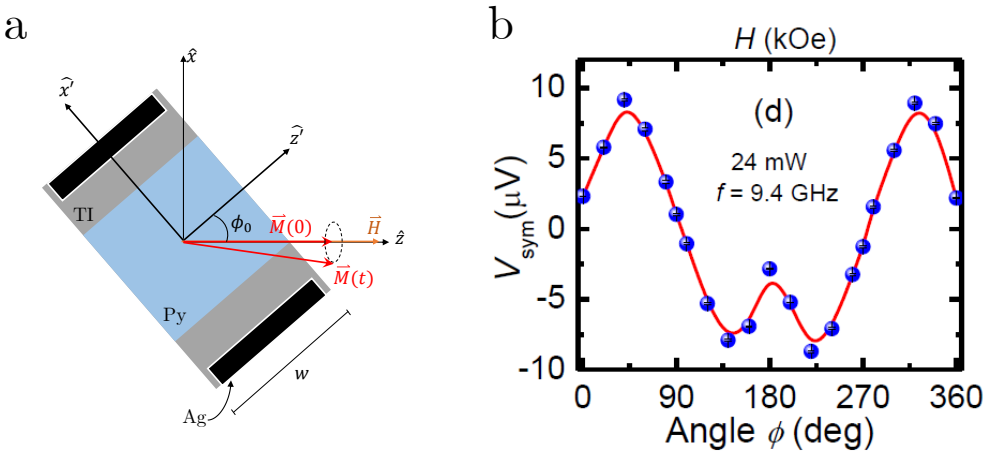

Figure 12.2: a. Schematics on the angle ϕ. **b.** Angular dependence of the symmetric component of the voltage line. The experimental data are represented by the solid circles and the theoretical fit by the solid red line.

The field-voltage dependence can be written by the sum of the contributions of symmetric ($L(H - H_r)$) and antisymmetric (($D(H - H_r)$) Lorentzian functions centred in the resonance field H_r (see Figure 12.3), we have then $V(H) = V_{sym}L(H - H_r) + V_{anti}D(H - H_r)$.

The Lorentzian derivative centred about the FMR resonance field H_r can give information of both symmetric and antisymmetric contributions. The voltage as function of the field angle ϕ and field H can be fit with the expression:

$$V(H,\phi) = \left[V_{cl}^{sym}L(H) + V_{cl}^{anti}D(H)\right]\sin 2\phi \sin\phi + V_q\, L(H)\cos\phi \tag{12.2}$$

where $L(H) = \Delta H/[(H - H_r)^2 + \Delta H^2]$ is the symmetric Lorentzian function and $D(H) = \Delta H(H - H_r)/[(H - H_r)^2 + \Delta H^2]$ is the antissymetric Lorentzian function. V_{cl}^{sym} and V_{cl}^{anti} are the amplitudes of the symmetric and antisymmetric components of the classical contributions, such as the galvanic effect, or spin rectification, generated in the Py layer [242]. V_q is the peak value of the symmetric contribution to the voltage of quantum origin, which exhibits a linear dependence with the microwave power and is due to the magnonic charge pumping (MCP) that is produced in a single Py layer [243]. The symmetric and antisymmetric contributions of the measured V(H) can be separated in the two contributions according to Equation 12.2 and can be seen in Figure 12.3.

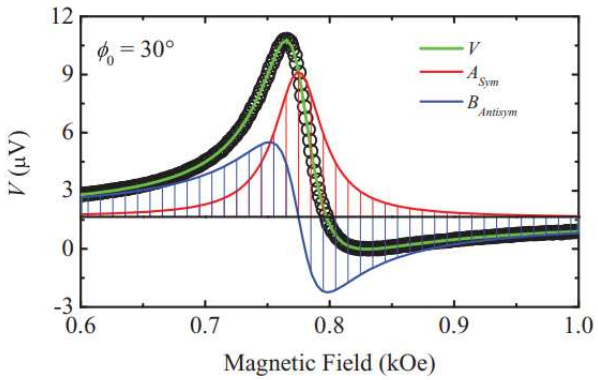

Figure 12.3: Measured dc voltage (open circles) in Pt/Py bilayer. The asymmetric green line is given by a superposition of symmetric (red line) and antisymmetric (blue line) components. Extracted from [242]

We have measured V(H) for different microwave powers (Figure 12.4a) and separated in the symmetric (Figure 12.4b) and antisymmetric (Figure 12.4c) contributions. The most important source for the symmetric component of the voltage, and the one of interest here, is the conversion of the spin current produced by spin pumping into charge current in the TI layer.

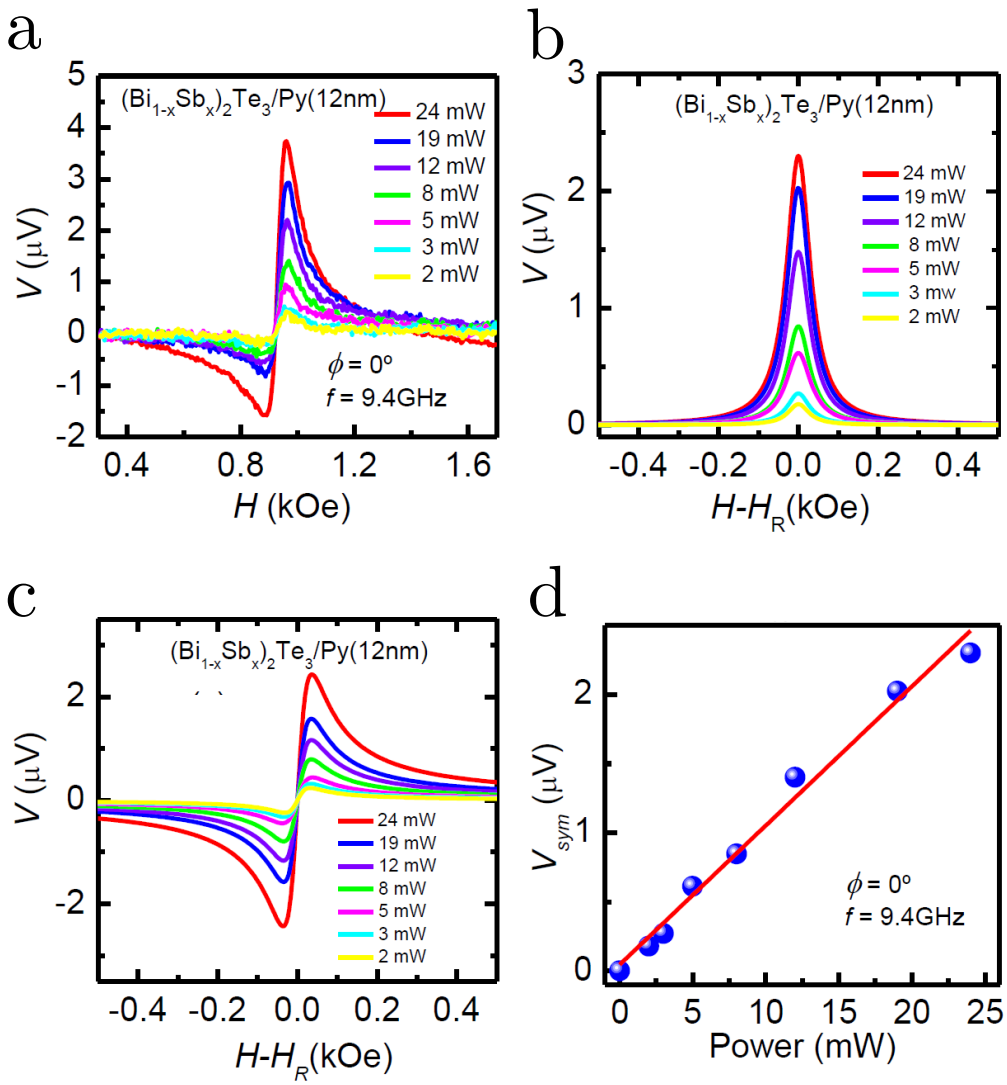

Figure 12.4: **a.** Voltage measured between the electrodes at the field angle $\phi = 0°$ for several microwave power levels, as indicated. **b.** and **c.** Variation with power of the symmetric and antisymmetric components of the voltage obtained by the fitting of Lorentzian derivative functions to the line shapes in **a**. **d.** Power dependence of the measured symmetric peak component of the voltage at $\phi = 0°$.

In a ferromagnetic layer under ferromagnetic resonance, the precessing magnetization generates a spin current density (J_s) at the FM/TI interface given by

$$J_s = \frac{e\omega p g^{\uparrow\downarrow}}{8\pi}\left(\frac{h_{\rm rf}}{\Delta H}\right)^2 L(H) \tag{12.3}$$

where ω is the microwave frequency, e is the electron charge, h_{rf} is the amplitude of the driving microwave magnetic field, and p is the precession ellipticity factor, written as

$$p = 4(\omega/\gamma)(H_r + 4\pi M_s)/(2H_r + 4\pi M_s)^2 \tag{12.4}$$

and $g^{\uparrow\downarrow}$ is the interfacial spin mixing conductance, that takes into account the spin-pumped and backflow spin currents, defined as:

$$g^{\uparrow\downarrow} = \frac{4\pi\gamma M_s d_{\text{FM}}}{g\mu_B\omega}\left(\Delta H_{\text{TI/FM}} - \Delta H_{\text{FM}}\right) \tag{12.5}$$

for d_{FM} the thickness of the ferromagnetic layer and $\Delta H_{\text{FM}} = 28.0Oe$ and $\Delta H_{\text{TI/FM}} = 33.0Oe$ being the measured linewidths for the FM layer alone and on top of TI, respectively.

The spin-to-charge conversion in the TI layer arises from the inverse Edelstein effect (IEE), which has its origin in the spin-momentum locking in the Fermi contours due to the Rashba SOC interaction [244–248]. The spin-momentum locking conduction electrons on the surface of TI states behave as Dirac fermions, where their direction of motion is determined by its spin direction. The spin-momentum locking on a single Dirac cone predicts efficient spin-electricity conversion in TIs even at room temperature as long as the surface state is robust, in other words, topological insulator surface state produces a different sign and a much larger magnitude of spin accumulation than is produced in non-topological materials [23].

The Edelstein effect is defined in which spin injection induces nonequilibrium spin polarization (S_y) and generates a charge current (J_{C_x}) in the longitudinal direction due to the effective magnetic field (generated by the spin-orbit coupling) "seen" by the drifting electrons in their own reference frame [249]. The 3D spin current in Equation 12.3 flows into the TI layer and is converted by the inverse Edelstein effect (IEE) into a lateral charge current with a 2D density, following the relation

$$J_c = (-\hbar/e)\lambda_{\text{IEE}} J_s \tag{12.6}$$

where λ_{IEE} is a coefficient characterizing the IEE, with the dimension of length and proportional to the Rashba coefficient (and hence to the magnitude of the SOC) and proportional to ratio between the induced 2D charge current density J_c and the injected 3D spin current density J_s [250].

The spin mixing conductance (Equation 12.5) of the $(Bi_{0.22}Sb_{0.78})_2Te_3$/Py interface can be found from the broadening of the FMR linewidth due to the spin pumping process. With d_{FM} = 12 nm, $\omega/2\pi$ = 9.4 GHz, we find that the additional linewidth of 5 Oe measured in Py due to the contact with the TI layer corresponds to $g^{\uparrow\downarrow}$ = 1.0 $\times 10^{19} m^{-2}$, a value similar to the one for Py/Pt interfaces, demonstrating an efficient spin transfer in $(Bi_{0.22}Sb_{0.78})_2Te_3$/Py heterostructure.

The induced spin current given by Equation 12.3 can be calculated using $h_{\text{rf}} = 1.776P_i$ where the incident power (P_i) of the microwave is 24mW and the relation above is calculated for the used microwave cavity. Using these values, we obtain a current spin density at the interface produced by the FMR spin pumping $J_s = 2.3 \times 10^5 A/m^2$. The charge current density due to

the conversion from the spin current by IEE can be found from $J_c = V_{\text{IEE}}/wR_s$, for R_s the shunt resistance and w the width of the TI/Py bilayer (see Figure 12.2a). The value measured for the symmetric peak voltage $V_{\text{IEE}} = 2.1\mu V$ and considering the shunt resistance the one of the Py layer of $R_s = 71\Omega$, and the width w of the sample 1.5mm, we can calculate $J_c = 1.7 \times 10^{-5} A/m$ and $\lambda_{\text{IEE}} = 0.075nm$.

12.2 Spin Seebeck Results

Another approach to verify the spin to charge current conversion in those systems can be done by Spin Seebeck Effect [251], where the schematics for this measurement are described in Figure 11.7b. In this device a 5 nm thick NiO layer provides electrical isolation between the TI and Py films. The Py layer has a width of 1.0 mm, smaller than the NiO and TI layers, to avoid possible contacts at the edges. A commercial Peltier module, of width 4 mm, is used to heat or cool the side of the Py layer while the substrate is maintained in thermal contact with a Copper plate at room temperature. The temperature difference ΔT across the sample is calibrated as a function of the current in the Peltier module.

NiO is an antiferromagnetic (AFM) material at room-temperature and it may block the flow of charge current but transports spin currents [252, 253], allowing us to measure the voltage generated in the TI layer separated from the voltage induced in the Py layer by the ANE [254].

The temperature gradient perpendicular to the Py layer has two effects: One is to generate a voltage along the layer by means of the classical anomalous Nernst effect (ANE) the other is to generate a spin current across the Py layer by the longitudinal spin Seebeck effect (LSSE).

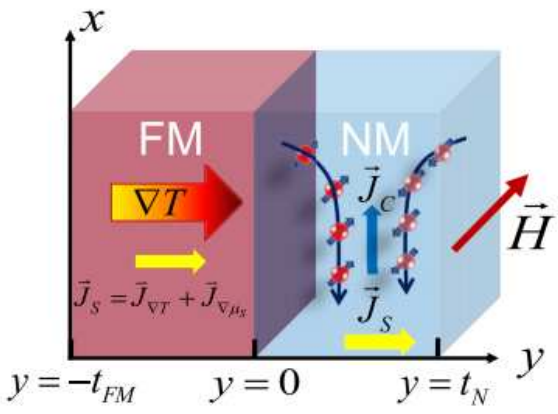

Figure 12.5: Schematics on the LSSE measurements. In our case, there is an AFM layer between FM and NM layer and the last one is a TI. Extracted from [255]

The Nernst Effect occurs when a temperature gradient can drive the charge carriers through the system and an electric field is produced along the direction normal to the temperature

gradient and the magnetization. It can be interpreted as the thermoelectric equivalent of the anomalous Hall effect and its results are shown in Figure 12.6a-b. The data have the shape of the hysteresis curve of Py with very small coercivity in the field scale of the measurements. The change in sign of the ANE voltage with field reversal is due to the change in the polarization of Py filmd. Since the Nio layer ct as a filter for charge currents and the ANE is intrinsecally smaller than the LSSE effecy, in this case the ANE effect can be negected [256, 257] and it is consistent with results in the literature with only a planar film of Py [258].

The interest here is in the LSSE results (as schematics in Figure 12.5). The voltages measured between the two electrodes in the TI layer are produced by the electric current resulting from the IEE spin-to-charge conversion of the spin current generated by the spin Seebeck effect in the Py layer. The spin current is injected into the Py/NiO interface and transported by magnons in the NiO layer into the TI layer. Figure 12.6c shows the magnetic field dependence of the SSE-IEE voltage in the TI layer for several values of the temperature gradient across the sample structure, according to the scheme of Figure 11.7b. This voltage is produced by the charge current resulting from the ISHE conversion of the spin current generated by the thermal gradient in the Py layer.

Figure 12.6d shows the measured variation of the voltage for different temperature gradients for applied fields of $\pm$ 400 Oe. The linear dependence of V_SSE on ΔT arises from the fact that the spin current generated by the LSSE in Py is proportional to the temperature gradient across the Py layer.

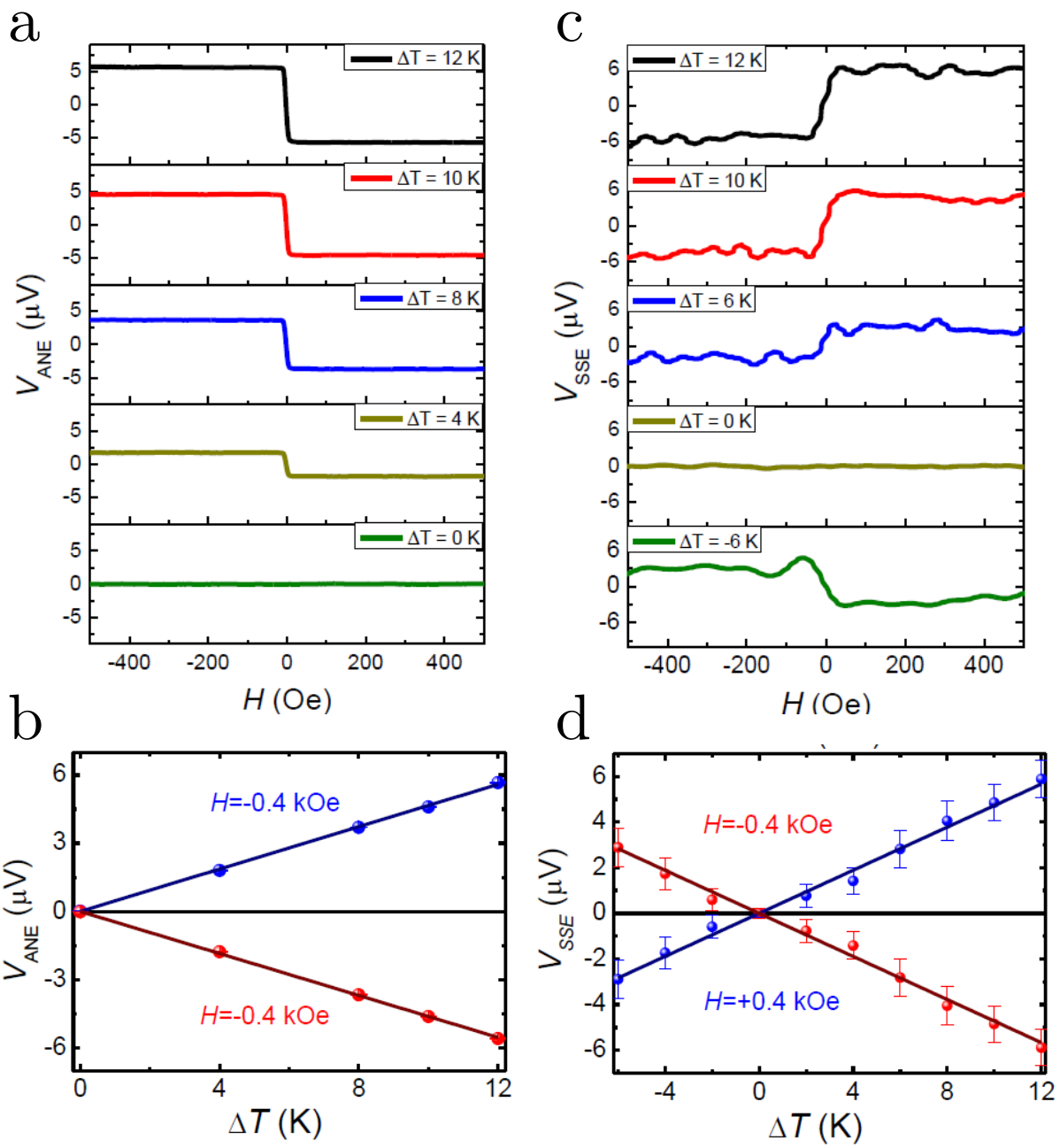

Figure 12.6: **a.** Variation with magnetic field of the ANE voltage measured in the Py layer with several values of the temperature difference indicated. Positive corresponds to the Peltier module warmer than the substrate. **b.** ANE voltage versus temperature difference measured with H=0.4 kOe in two field directions. **c.** Variation with magnetic field of the SSE-IEE voltage measured in the TI layer, created by the combined SSE in the Py layer and IEE in the TI, for several values of ΔT as indicated. **d.** Variation with temperature difference of the SSE-IEE voltage measured with H=0.4 kOe, in two field directions.

The temperature gradient on the PY layer can be calculated from

$$\nabla T_{\mathrm{Py}} \approx \frac{K_{\mathrm{sub}}}{K_{\mathrm{Py}}} \frac{\Delta T}{d_{\mathrm{s}}} \tag{12.7}$$

where K_{sub} and K_{Py} are the thermal conductivities of the substrate and Py, respectively and d_s is the thickness of the whole sample. For our substrate Al_2O_3 ($K_{Al2O3} = 41.9W/(Km)$), and $K_{Py} = 46.4W/(Km)$, for a $\Delta T = 12K$ and the sample thickness being mostly the substrate thickness (0.5mm), we can find $\nabla T_{Py} \approx 217K/cm$.

Compared with previous results [255], for a Si/Pt/NiO/Py stack, the calculated $\nabla T_{Py} \approx 957K/cm$ and a charge current density $J_c = 1.6 \times 10^3 A/m^2$. The spin current due to spin Hall effect can be found by $\vec{J}_c = \theta_{SH} \vec{J}_s \times \hat{\sigma}$, for θ_{SH} being the spin Hall angle (0.05 for Pt) and have a value of $J_s = 3.2 \times 10^4 A/m^2$ for $\Delta T = 12K$.

Since the generated spin current is directly proportional to ∇T, we can expect, by comparing with the sample in [255], for the same thickness of Py and NiO, a spin current of $J_s = 7.2 \times 10^3 A/m^2$.

The measured resistance in the TI layer is $R = 1.08 \times 10^4 \Omega$ and from the results (Figure 12.6), the voltage between two electrodes is $5.4\mu V$ leading to a current density $J_c = 5.46 \times 10^{-7}$ A/m, much smaller than reported for Pt/NiO/Py. The inverse Edelstein coeficient $\lambda_{IEE} = 0.076nm$ which is nearly the same obtained from the SPE measurements.

13 - Discussion and Perspectives

The efficiency of our system can be compared to others according to Table 13.1.

Sample	$\lambda_{\text{IEE}}(nm)$	$g^{\uparrow\downarrow}(\times 10^{19} m^{-2})$	Reference
Py/NiO/$(Bi_{1-x}Sb_x)_2Te_3$	0.075	1	This Work
Bi/Ag/Py	0.2 to 0.33	1.90 to 2.8	[244, 259, 260]
Bi/Cu/Py	0.002	-	[261]
Bi_2Se_3/YIG	0,017 to 0.036	0.415	[26]
Fe/ α-Sn TI	2	-	[247]
Bi_2Se_3/Py	-	1	[262]
CoFe/Bi_2Se_3/Py	-	0.0025	[263]

Table 13.1: IEE parameter and Spin Mixing conductance in different systems.

The λ_{IEE} value measured by SPE and SSE have shown to be smaller than already reported in Bi/Ag/Py and in the same order of magnitude found in Bi/Cu/Py, at room temperature, but is higher than reported in Bi_2Se_3/YIG bilayer. The spin mixing conductance in our system ($g^{\uparrow\downarrow} = 1.0 \times 10^{19} m^{-2}$) have also shown to be higher than in Pt/Py systems which is an indicative of more effective spin to charge current efficiency on those systems [262].

It is important to note that the magnitude of the IEE coefficient should depend not only on intrinsic TI properties, but also on sample preparation processes. In recent studies of TI-based spin pumping works, the interface property plays a critical role for enhancing the spin conversion efficiency [26, 245].

The high intrinsic efficiency of TIs ate still not at maximum because most of the applied current is still shunted through the metallic layer and does not contribute to the generation of spin current in the TI, which is the interest here. Practical applications will probably require that the magnetic layer over the topological insulators to be insulating (or high-resistivity) magnets so that the majority of the current will flow just in the topological insulator.

Part III

Thermodynamics on rectangular-lattice Spin Ices

14 - Introduction

Geometry induced dynamics yields remarkable physical phenomena. In the macrocosmos, the curvature of spacetime (geometrodynamics) tells matter how to move implying in effects like gravitational lensing, birefringence, rotation of the plane of polarization of light from distant sources and others. [264,265]. In the microsize, an example is the geometrical frustration [266] in magnetic materials, whereas under certain conditions, can lead to the formation of spin liquids [267], in which the constituent spins spins are highly correlated but still fluctuate even at low temperatures.

In this work, we would like to explore a geometrical effect in artificial spin ices (ASI). It is theoretically predicted that, in general, this artificial materials are athermal, or at least they respond to temperatures in the order of around $10^5 K$, which is well above Curie temperatures or melting point of ferromagnetic materials. They are constructed with elongated nanomagnets containing a large number of atomic spins, generating a big net magnetic moment that need a great amount of energy to flip.

Therefore, recently, thermally driven dynamics in ASI materials became an important subject of investigation [268] and this picture shows that geometrically driven dynamics in ASI can open up a new view for exploring distinct ground states and thermally magnetic monopole excitations. Here, it is shown that a particular ASI lattice, whereas four spins meet at every vertex, will provide a richer thermodynamic effects, only due to its geometry.

Here, we show theoretically and experimentally that the geometry of the planar arrays may be an additional ingredient able to cause important physical phenomena in ASI materials. In fact, by studying three rectangular artificial spin ices (RASI) systems with different geometric aspect ratios γ, we demonstrate that the geometrical influence goes beyond the simple effect of the variation in lattice parameters.

15 - Spin Ices

Spin ices [269, 270] are a new class of magnetic materials that have been attracted the attention of the scientific community in the past decades [271–274]. This magnetic arrangement shows a magnetic ordering similar to the hydrogen positions in a water molecules in the solid state (that's the origin of the denomination spin "ice"), which shows a degeneracy in the ground state due to the geometry, driving the system to a geometric frustration [275].

The geometrical frustration concept arises from the incapacity of a system to minimize iterations between pairs in a whole system that can apper from a natural intrinsic disorder or a regular geometry that balances the consecutive interactions [276]. Frustration does not appear only in magnetic system, being found also in other fields of study like biological systems [277–279], superconductors [280–282] and ferrites applied to microelectronics [283] but is more common and better understandable in magnetic systems. In this case the concept of magnetic frustration is associated to the incapacity of a system to minimize the energy to the ground state, from each spin-spin interaction. When those interactions can't be satisfied at the same time, the system is called frustrated. The most fundamental example of frustration is considering Ising type spins (that are confined in one direction) antiferromagnetically coupled in a triangular lattice. Figure 15.1 shows in a square lattice, all interactions can be satisfied, but in a triangular lattice, the missing spin can't satisfy the condition for both adjacent spins at the same time.

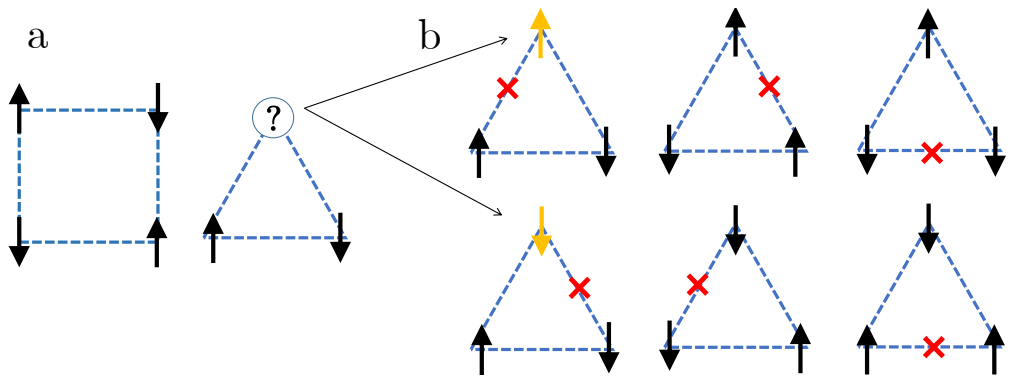

Figure 15.1: a. Square and triangular geometries. In the triangle, the Ising spin on the top (?) can't satisfy the antiferromagnetic coupling with the other two at the same time. **b.** The six possible configurations for the lower energy state in the triangular system, with the red cross showing where the frustration occurs. The yellow arrows are the replacement for the missing (?) symbol.

This frustration leads to degenerate ground states in case of a lone triangle, for example [284]. In an array of triangular structures have multiple degenerate ground states which makes the system unable of having a long range magnetic order [285, 286]. In the case of the square lone structure the system is only two-fold degenerate.

The magnetic frustration in some systems can lead to new and more complex phenomena like emergent quasei-particles, like magnetic monopoles of Dirac [287] or Nambu [288], depending on the geometry of the system. Those emergent monopoles have been researched both theoretically [268, 276, 289, 290] and experimentally [291–293] and with the possibility of control the transport of these magnetic excitations [294–296].

15.1 Water Ice Structure

In the early 30's, Giauque and collaborators [297, 298] observed, even at low temperatures (around 10K) that the water ice had a residual entropy different than zero, contradicting the third law of thermodynamics. Linus Pauling [299] and Bernal and Fowler [300] explained this phenomena and estimated this residual entropy by considering relocating the hydrogen atoms in the H_2O molecules. Pauling claimed that in the ice, each O^{2-} oxygen ion was in the center of a tetrahedron surrounded by other four oxygen ions in the vertices with an hydrogen ion (or just a proton) between each pair. This proton does not stand at the center of the distance between two oxygen ions, but closer to one of them, as shown in Figure 15.2, being this the origin of the residual entropy.

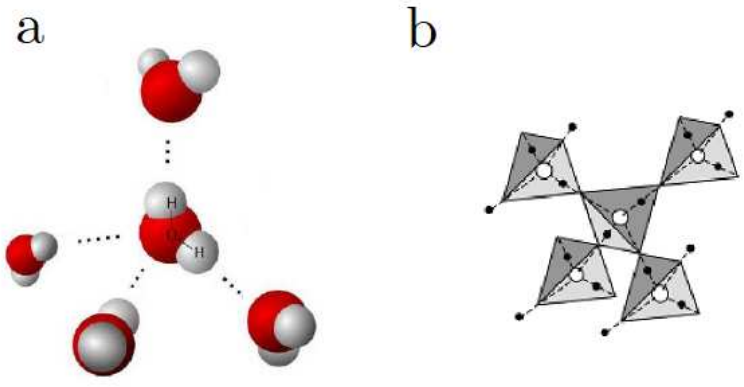

Figure 15.2: a. Schematics of the water ice structure. The dashed lines represents the hydrogen-oxygen bondings. **b.** Tetrahedron structure with neighbours tetrahedra. The with circle representes oxygen ions and black circle represents the hydrogen. Adapted from [301].

This configuration of the protons obeys the called the 'ice rule' (*two-in - two-out*), that means in the ice water arrangement, for a certain oxygen ion, there are two protons closer and two far from it [302].

15.2 Frustration in Pyrochlore Hexagonal Strucutres

The Pauling model for the water has a similar interpretation in magnetic systems in a class of materials with magnetic structures similar to the water ice. Those materials, pyrochlore oxides with the form $A_2B_2O_7$, where A are rare earth ions and B are transition metal ions, have a tetrahedral geometry, where the magnetic moments are located in the vertices of this tetrahedron. Harris *et.al.* in 1997 [269] was the first to propose that the pyrochlore lattice may be mapped directly onto the ice lattice with the $Ho_2Ti_2O_7$ [303] oxide, obeying the ice rule. Other oxides like $Dy_2Ti_2O_7$ [270] and $Ho_2Sn_2O_7$ [304, 305] have also been studied for showing the same behaviour at low temperatures.

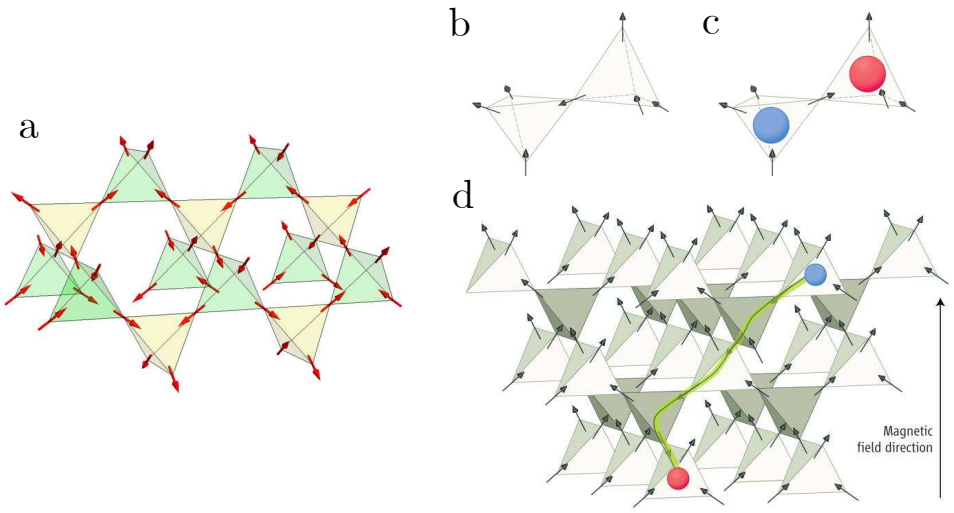

Figure 15.3: a. The pyrochlore lattice with the magnetic moments in each vertex of the tetrahedron. The spin arrangement on each individual tetrahedra obeys the ice rules with two spins pointing in and two spins pointing out. Extracted from [306] **b.** Magnetic moments configuration on two adjacent tetrahedra satisfying the ice rule. **c.** If a spin between two tetrahedra is fliped, the ice rule is broken, creating a "monopole" and an "antimonopole" that differ in magnetic "charge". **d.** A pyrochlore lattice with the monopole-antimonopole pair, connected by a string. Extracted from [307]

In those systems, the ions Ho^{3+} or Dy^{3+} are located in the vertices of the tetrahedra and are the responsible for the magnetic moments (Figure 15.3a) behaving, due to the magnetocrystalline anisotropy, like the Ising model spins [272] pointing to the center or outside the tetrahedron(Figure 15.3b). A tetrahedron that obeys the ice rule neutralize the net magnetic charge in the center of the structure, with two magnetic moments pointing in and two pointing out, cancelling each other in the center. A magnetic moment that changes direction, due to thermal excitations for example, can lead to a "monopole - antimonopole" pair, or magnetic charges as shown in Figure 15.3c.

The rare earth ion carries a large magnetic moment (from its unfilled f-electron shells)

[308], of around ten Bohr magnetons [309]. The hamiltonian that describes this system has the form [274]:

$$\mathscr{H} = \frac{J}{3}\sum_{ij} S_i \cdot S_j + Da^3 \sum_{ij}\left[\frac{\hat{e}_i\hat{e}_i}{|\vec{r}_{ij}|^3} - \frac{3(\hat{e}_i\cdot\vec{r}_{ij})(\hat{e}_j\cdot\vec{r}_{ij})}{|\vec{r}_{ij}|^5}\right] S_iS_j \tag{15.1}$$

where the first term on the right side is the exchange interaction, with J the exchange constant and the second term (in the brackets) is the dipolar interaction, with $D = \mu_0\mu^2/4\pi a^3$ the dipolar interaction constant. a is the lattice parameter ($\approx$ 3.54Å for this system) and $\vec{r}_{ij}$ is the spin position. This dipolar interaction is dominant in systems formed by nanoparticles with a separation between them. The exchange interaction have a limited range of distances, in order of a few angstroms. The dipolar interaction have a much higher value in single domain, interagent particles, compared to the atomic moments.

The magnetic moments $\vec{\mu_i}$ point along the local axis $\hat{e}_i$ and are modelled as Ising type spins where $\vec{S_i} = S\hat{e}_i$, and $S = \pm 1$.

Castelnovo's results in 2008 [274] corroborated with the idea of a dominant dipolar interaction between the spins, as a consequence, the interaction between consecutive spins have to be ferromagnetic, what gives rise to the frustration. The states that minimize energy in the tetrahedron structure is degenerate, with six of the sixteen possible configurations obeying the ice rule [267].

Castelnovo also proposed that the elementary excitations on spin ices behave like magnetic monopoles arises with the ice rule broken ($3-in1-out$ / $1-in3-out$ / $4-in$ or $4-out$) as shown in Figure 15.3c. This magnetic charges could be separated without further breaking of the ice rule (Figure 15.3d), just flipping a chain of magnetic moments in the structure, in this case, a string connect the opposite charges, bond together by a Colombian interaction. This string (Dirac string) does not carry energy, so the monopoles pair are free to move in the material.

15.3 Artificial Spin Ices

An alternative to the natural crystalline spin ices was suggested in 2006 by Wang *et.al.* [273] in an artificial, two-dimensional structure with frustration effects. In this artificial systems, it is possible to have a better control of the geometry, size, symmetries and disorders in a mesoscopic range.

Arrays of nanomagnets designed to resemble the spin ice materials (with disordered magnetic states) are known as artificial spin ices (ASI). Nowadays, with the advances of the nanofabrication techniques, the ASI systems have become an interesting field of study, as well

as their natural counterparts, with the advantage that they can be constructed with desirable geometries and properties. The net magnetic moment of each individual nanoisland is aligned parallel to its longest axis (like in a bar magnet), being considered here as a monodomain and is coupled to all other nanoislands of the planar array by the dipolar interaction.

The artificial spin ices (ASI) consists in a bidimensional lattice of magnetic nanoislands, arranged in a defined lattice, fabricated by e-beam lithograpy and composed by a thin film of magnetic material. The nanoislands are sufficiently small that the total magnetization in an island is a monodomain, behaving like Ising spins due to the shape anisotropy. The possible geometries studied are square [273], brickwork [310], honeycomb [292, 311, 312], triangular [313], unidirectional [296] and others [314, 315] (Figure 15.4), with different frustration effects, monopoles emergences and string configurations.

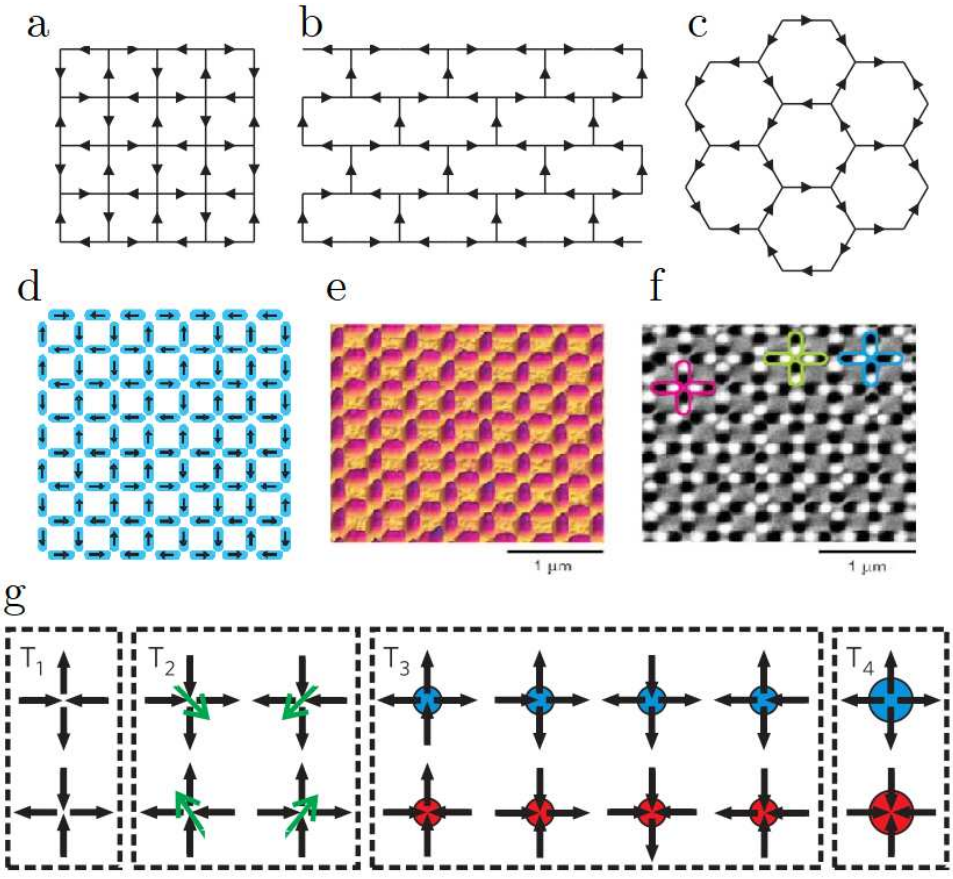

Figure 15.4: **a.** Square, **b.** brickwork and **c.** honeycomb lattices representation. Lines represent nanomagnet islands, arrows indicates the orientation of magnetic moment of the islands in ground state. Extracted from [314]. **d.** Square lattice studied by Wang. **e.** AFM image of the nanoislands. **f.** MFM images of the same array as **e**. The dark and white spots indicates oppposite magnetic fields (as in a north-south poles in a magnet). Extracted from [273]. **g.** 16 possible topologies in the square lattice, grouped in order of energy from left (lower) to right (bigger). The topologies T1 and T2 obeys the ice rule while T3 and T4 have a residual charge in the vertex. Extracted from [316]

In Wang's work, the nanoisland are 80nm x 200nm size with a thickness of 25nm arranged

in a square lattice, as in Figure 15.4. In the literature, the size of the nanoislands can vary a little, but are all in the same order of size, of around 300nm x 100nm x 25nm [296].

For the Wang islands, made of Permalloy ($Ni_{80\%}Fe_{20\%}$) have a magnetic moment $\mu = M_s V$ (M_s is the saturation magnetization of the material and V is the island volume) in the order of $3 \times 10^7 \mu_B$ (μ_B is the Bohr magneton) which make the energy scale due to dipolar interaction around 10^5K. This means that the temperature necessary to flip an island is much bigger than the Curie temperature of permalloy ($\sim$ 850K) making this system to be considered athermal [317].

The square lattice is the most similar to the pyrochlore spin ices, exhibiting 4 spins in each vertex with 16 possible configurations, as shown in Figure 15.4g. Those 16 configurations (by considering each nanoisland a perfect dipole) can be grouped in 4 topologies separated by energy. The lower energy configurations obeys the ice rule, as in T1 and T2. In the square lattice, those topologies are separated in two different energy states depending on the spins configuration. The ground state of the square lattice is two-fold degenerate and show a long range antiferromagnetic ordering [301].

The magnetic excitations in the vertices of the square lattice ("monopole-antimonopole" pair or magnetic "charges") have been studied theoretically by Mól and collaborators [289] in a square lattice by replacing the island magnetic moment for a Ising type spin located in the center of the nanoisland subject to dipolar interactions. Figure 15.5 shows the separation of magnetic charges by flipping consecutive spins. In the string length the vertices obeys the ice rule, but in the T2 topology. The separation of the charges not necessarily add more charges pairs to the system, but creates a chain between them. In the square lattice, the string carries energy (T2 topology are more energetic than T1) and thus those monopoles are called Nambu [288] monopoles, if the string is not energetic, the charges are called Dirac monopoles [290].

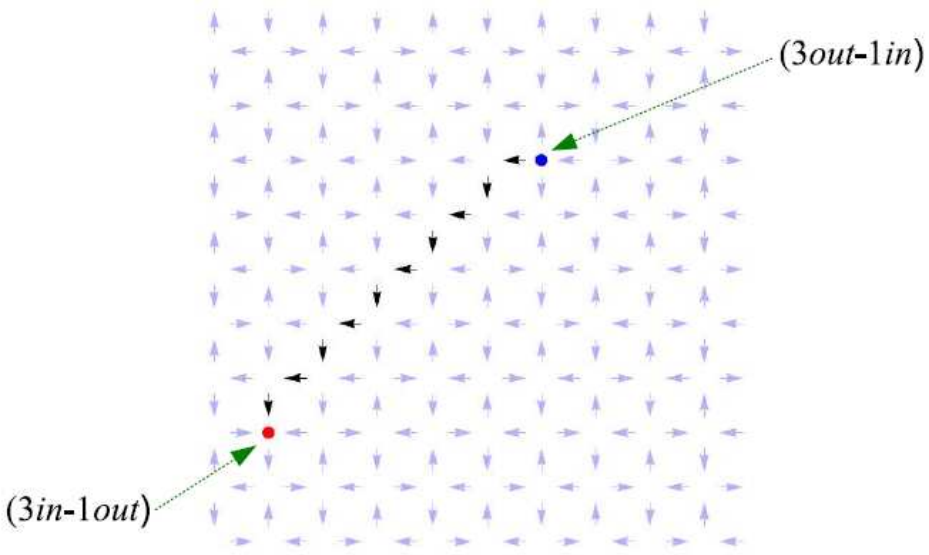

Figure 15.5: Separation of a monopole-antimonopole pair (blue and red dots) in a square lattice. Gray arrows represents the ground state and black arrows the fliped islands in the string. Extracted from [301]

Then, in its original configuration, ASI tiles a square lattice of vertices, with four nanoislands meeting at each vertex. The ground state of this artificial square ice obeys the ice rule, which remains the familiar two-in, two-out (two spins must point in, while the other two must point out in each vertex). However, in two dimensions, the standard ice rule is no longer degenerate [273, 289, 318]. This trouble comes together with the fact that this peculiar material is also athermal. Indeed, the magnetic moments involved are roughly a million times bigger than those of the ions forming the natural spin ices and, therefore, they interact much more strongly, having less tendency to flip. Therefore, to anneal the material into its ground state, the usual approach is not available because the kinetic barriers of individual islands are on the order of $10^4 K$. To advance our understanding (by studying ASI materials) of how geometrical frustration operates to produce new states of matter, at least, two initial difficulties should be experimentally overcome: first, it would be essential to construct arrays with degenerate ground states and, second, it would be important to develop methods to investigate the thermal fluctuations and dynamics of the nanoislands magnetic moment. In this work we would like to connect those two points by comparing arrays that exhibit different ground states, when they are heated to a high temperature regime (we mean by high temperature, the practical values in the range $300K - 800K$).

16 - Methodology

16.1 Sample Fabrication

After the development of nanolithography, the world of nanostructures has opened up to scientists being utilized in many fields of study and being a powerful tool to the miniaturization of electronic and spintronic devices and led to innovations in the micro and nanofabrication resulting in structures from nanometer size to milimiters with optical or electron lithography. The nanolithography process used in this work is displayed in Figure 16.1.

The electron beam lithography (e-beam) uses a focused electron beam scanned over a substrate covered with a sensitive polymer. The scan is done following a predefined path chosen and drawn by the user in a proper software. The polymer can be defined as positive or negative, depending on the effect of the electron beam during the process. In this work, the negative lithography [1] process was used. When exposed to the electron beam, in the negative resist, the molecules becomes crosslinked and more difficult to dissolve in developer, on the other hand, the positive resist becomes easier to remove in the development. In the development process, using the appropriate chemicals for each resist, the negative resist remains on the surface of the substrate where it is exposed (Figure 16.1**d** $\longmapsto$ **e**).

The electron beam lithography is done in a scanning electron microscope (usually) with a field emission gun (SEM-FEG) where the source of electrons is a Tungsten monocrystal in a high electrical field under ultra-high vacuum, giving an intense and focused electron beam, with a spot with around 20nm depending on the equipment accuracy. The scanning of the beam is made by electromagnetic lenses.

[1] $www.allresist.com/ebeamresists - ar - n - 7500 - 7520$

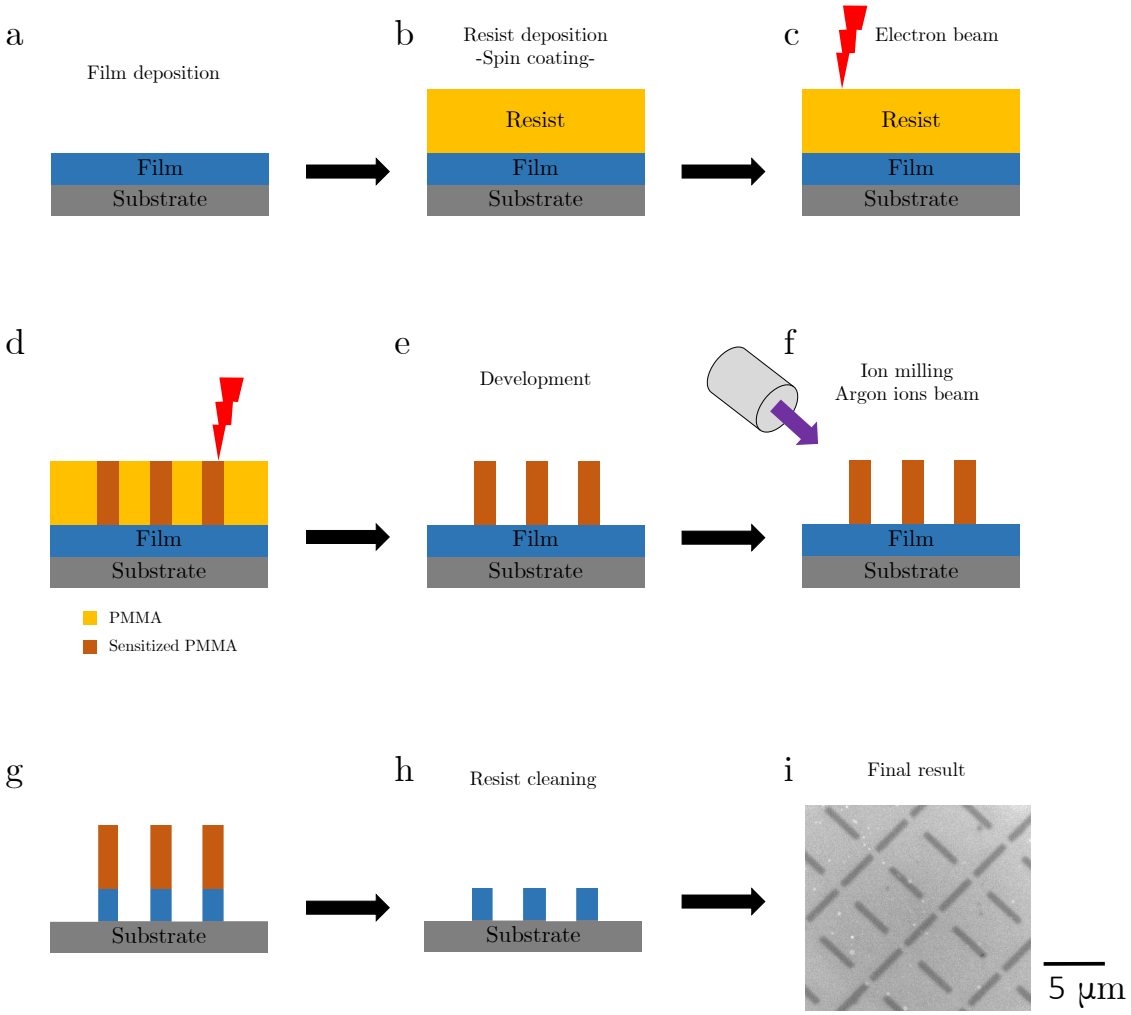

Figure 16.1: Nanolithography processes. **a.** Thin film deposition. **b.** Spin coating of the electron beam resist. **c.** The electron beam will sensitize some areas of the resist. **d.** Sensitized areas by the electron beam. **e.** The development process will remove the sensitized areas, in case of the negative resist used. **f.** Ion milling process. The remaining resist will protect the film underneath, the exposed areas will be removed. **g.** After the ion milling, the exposes areas were removed. **h.** After cleaning the remaining resist, the protected areas with the film remains, leading to the result in **i.** PEEM images of the structure studied in this work.

The silicon substrate is previously chemically cleaned with acetone, isopropyl alcohol and deionized water and taken after to a plasma cleaning in order to fully remove dust, organic residues and contaminants on the surface. The magnetic thin film is deposited via sputtering with a thickness of 3nm and 10nm of permalloy ($Ni_{0.8}Fe_{0.2}$). A buffer layer and a capping layer of Tantalum (3nm) is also deposited (Figure 16.1**a**), the last one to prevent oxidation of Ni and Fe. The multilayer is then composed by Si / SiO_2 / Ta 3nm / $Ni_{0.8}Fe_{0.2}$ 10nm / Ta 3nm and is previously prepared by sputtering from tantalum (seed and cap layer) and alloyed permalloy target. The samples were covered with a layer of AR-N 7500 (ALLRESIST GmbH) negative resist (Figure 16.1**b**). After development (Figure 16.1**e**) the samples were etched by ion milling (Figure 16.1**f** $\longmapsto$ **g**). An ashing in oxygen plasma was subsequently performed to remove the

photoresist. The nanoislands dimensions of l = 3000nm and w = 400nm (Figure 16.1**i**) were conceived in order to present magnetic monodomain in each island. These systems were built on an area of 100μm^2, which enabled topologies density analysis in arrays of up 10 x 14 unit cells (140 islands).

16.2 Characterization

16.2.1 Photoemission Electron Microscopy

The photoemission electron microscopy (PEEM) is one of the most widely used type of emission microscopy and is closely related to the low energy electron microscopy (LEEM). Since the photoelectric effect, explained by Einstein in 1905, where an electron can be ejected from an atom by interacting with a photon of quantized energy.

Before the development of x-rays usage in photoemission microscopy (X-PEEM), UV light was used (UV-PEEM) [319] with a spatial resolution of 10 nm. The first x-ray photoemission was first done in 1987 [320] and in 1993 Stohr discovered the possibility of X-PEEM to measure magnetic domains [321]. With the development of the technique, nowadays most PEEM equipments are located in a synchrotron radiation facilities [322–325].

It is well known that charged particles emit electromagnetic radiation when accelerated. The synchrotrons light sources, or electron storage rings, are one of the most powerful sources of intense x-rays. The synchrotron radiation is generated when relativistic electrons are deflected, for example, by a dipole magnet. The emmited radiation can be found in a range from infrared (micrometer wavelength) to hard x-rays (Angstroms). Radiation from a dipole or bending magnet is linearly polarized in the storage ring plane. In certain circumstances the radiation can be right and left elliptically polarized. The X-rays from the storage ring are driven to the experiment through an evacuated beamline. A grating monochromator in the beamline generates a monochromatic beam. The soft X-rays covers the absorption edges of many important elements, specially Fe, Co, and Ni, ferromagnetic transition metals, necessary also for the XMCD technique (as discussed in Figure 16.4. The X-rays are focused onto the sample using X-ray mirrors [326].

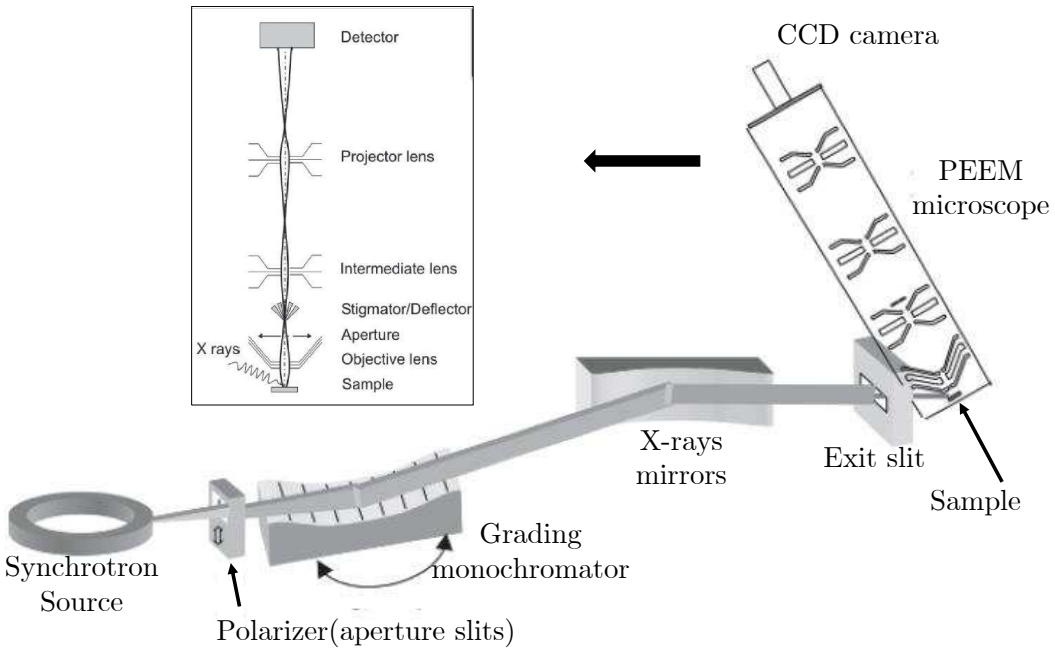

Figure 16.2: PEEM equipment setup. The inset show a detaliled scheme of a simplified PEEM microscope. A more detailed description of the PEEM microscope with the correction lenses can be found in the Lawrence Berkeley National Laboratory website [327]. Adapted from [326].

When the synchrotron generated x-rays hit the sample, electrons from the core level of the atoms are excited to unoccupied states, leaving a hole in the core level. A secondary electron decays to the hole, when Auger processes and inelastic electron scattering occurs. Some of those electrons are ejected and captured by the PEEM detector.

The PEEM technique can be combined with XMCD to magnetic imaging, as discussed in the section below.

16.2.2 X-ray Magnetic Circular Dicrohism

In optics, dicrohism refers to any optical device which can split a beam of light into two beams with differing wavelengths, or from different views, the material appears with two different colors for two different directions, it is called is di- (two-) chroic (colored) [328]. The dicrohism property is not a particularity of visible light and now the use of polarized soft x-rays techniques have become a major tool for measuring properties of magnetic materials. The main advantages of using soft x-rays are good spatial resolution, quantitative information because of the strong magnetic contrast, sensitivity to chemical elements, well defined core-level states among others [329, 330]

The magnetic properties of transition metals are given by the d-valence electrons. The soft x-ray region covers the important edges for transitions in regions that admits access to the strong dipole-permitted core 2p to valence 3d excitations ($L_{2,3}edge$) in transition ferromagnetic metals

(Ni, Fe, Co) and core 3d to valence 4f ($M_{3,4}edge$) in rare-earth elements [331]. Core electrons are excited by the absorption into empty states to above the Fermi level carrying information of the electronic and magnetic properties of the empty valence levels. The magnetic properties of magnetic transition metals are largely determined by the 3d valence electrons.

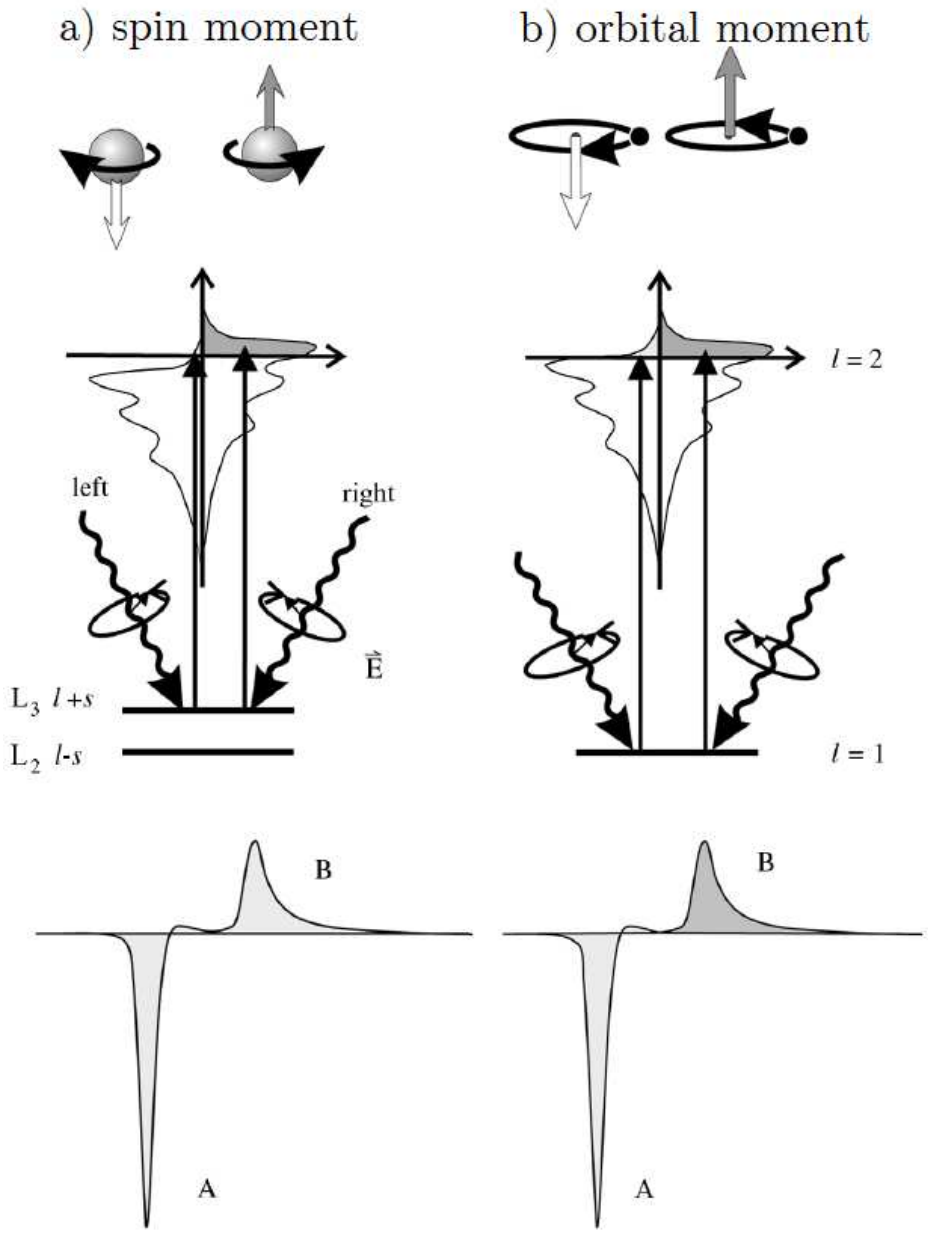

Figure 16.3: One-electron model XMCD. The transitions occur from the spin orbit split of the 2p core levels to empty conduction bands above the Fermi level. By use of circularly polarized X-rays the spin moment **a**, and orbital moment **B**, can be determined from the intensity differences between A and B. Adapted from [332]

The XMCD consists in right or left circularly polarized photons can transfer their angular momentum, $\pm\hbar$ to an excited photoelectron and the x-ray magnetic circular dichroism effect

describes the change in x-ray absorption. The light interacts indirectly with the spin via the spin-orbit interaction, in this case the dichroism increases in with the spin-orbit interaction and spin flips are forbidden, so the photoelectrons from the p-core shell can only be exited to the d-hole state with the same spin it had before. The XMCD effect is opposite in sign at the L_3 and L_2 edges because of the opposite sign of the spin-orbit coupling ($l+s$ and $l-s$, respectively due to the spin-orbit split level) and the spin polarization will be opposite in those two edges. The difference on the intensities measured with right and left circular polarization are A, for L_3 edge, and B for L_2 edge, respectively. The different coupling gives to XMCD the ability to separate spin and orbital momentum. The spin momentum is proportional to the difference of the integrated XMCD intensity and the orbital momentum is proportional to the sum. Sum rules have been developed that are used to quantitatively determine the spin and orbital magnetic moment per atom. The complete mathematical approach of those sum rules can be found in [329, 332, 333]

The relative orientation between the photon polarization (σ) and the sample magnetization ($\vec{m}$) is the origin of XMCD effects that have a signal propotional to $\vec{\sigma} \cdot \vec{m}$ and the largest signal difference occurs between the parallel and antiparallel orientation of σ and $\vec{m}$. In the case of the nanoislands, magnetization direction is in magnetic monodomains so the XMCD intensity obtained by the difference of the two X-ray helicities (left and right polarized) [332].

The XMCD effect is opposite in sign at the L_3 and L_2 edges because of the opposite sign of the spin-orbit coupling $l+s$ for $2_p3/2$, and $l-s$ for $2p_{1/2}$. Most intense XMCD effects appear at the L edges ($2p$ to $3d$) of the transition metal ferromagnets Fe, Co, and Ni. The XMCD spectrum is defined as the difference spectrum of two absorption spectra obtained by different light polarizations. The angle and magnetization dependence of XMCD in the total absorption signal is approximately given by

$$I_{xmcd} \approx cos\alpha\langle\vec{M}\rangle \tag{16.1}$$

with α denoting the angle between the X-ray vector $\vec{E}$ and the magnetization $\vec{M}$. $\langle\vec{M}\rangle$ is the expectation value of the magnetization of 3d shell [326].

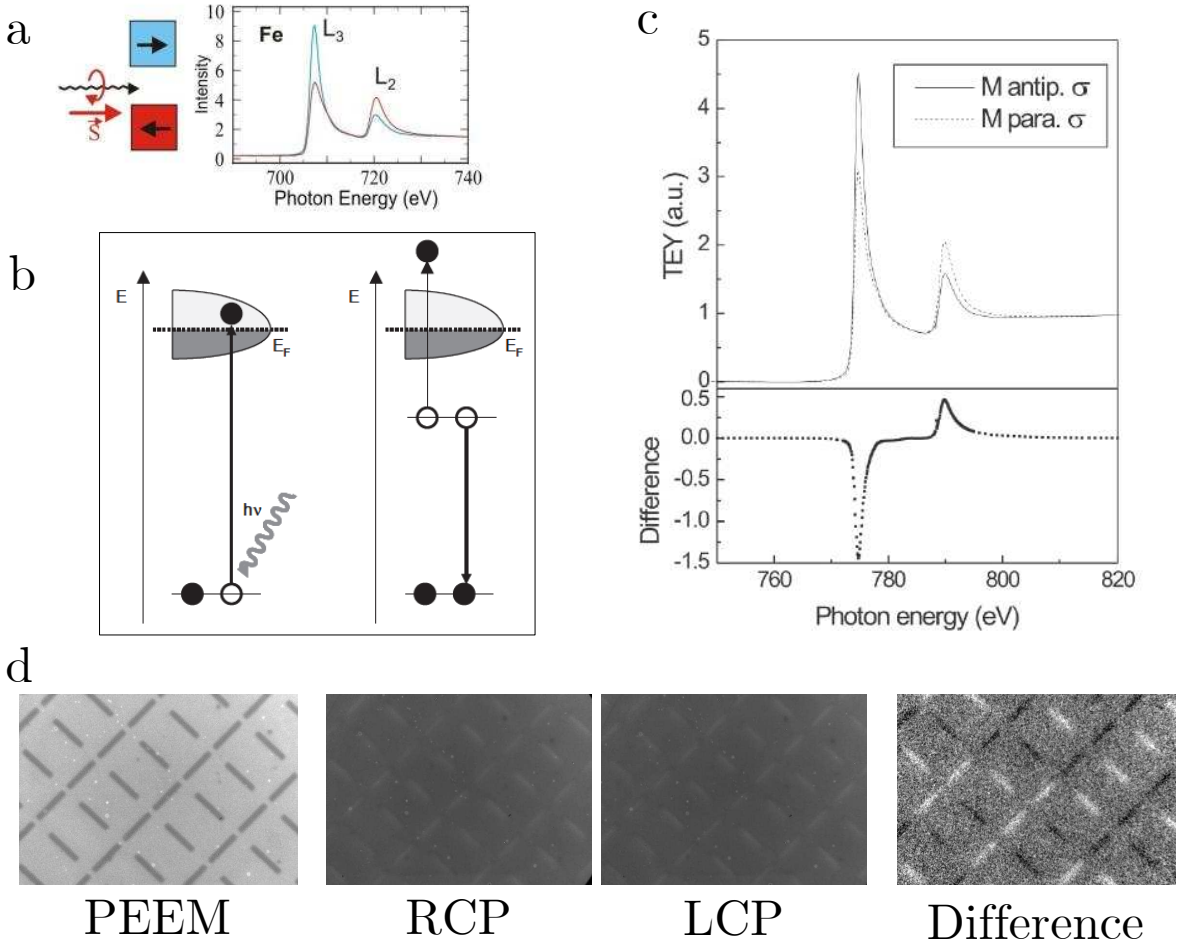

Figure 16.4: **a.** Scheme of magnetic dichroism effects. The XMCD effect is large only in cases where the absorption edge exhibits multiplet structure. Adapted from [328]. **b.** Absorption shceme of x-rays by the core level of an atom (left) and Auger decay (right) and the ejection of a secondary electron. Extracted from [326]. **c.** Cobalt XMCD spectra acquired for a magnetization M parallel (dotted line) and antiparallel (solid line) to the X-ray polarization σ. At the bottom the difference spectrum is shown. Extracted from [326]. **d.** PEEM image of one of the measured structures of this work. XMCD-PEEM measurement of the sample. The right and left circularly polarized measurements are shown, by taking the difference between them a dark and bright contrast appear, due to the difference of magnetic orientation in each island, as in the case of **c**.

16.2.3 MOKE

The Magneto optical Kerr Effect (MOKE) is an optical technique to determine the orientation of a magnetic moment near the surface of a reflecting magnetic sample . It is based on the Kerr effect, observed by John Kerr in 1887. A similar effect was first observed by Faraday in 1845 where he found that polarization of light transmitted through a magnetic sample was rotated.

MOKE It is based on the interaction of a linearly polarized light reflects in a magnetized material, becoming eliptically polarized. This elliptical polarization of light results when the two orthogonal components of electric field vector from the light wave experience a phase difference. The rotation of the polarization is due to the interaction of the light with the unpaired valence

electron spins of the magnetized sample. MOKE measurements can give a the response to the material with an external field, by giving the magnetic hysteresis loop of the material [334].

If the electric field is polarised in the plane of incidence, it is called as p-polarised light as shown in Figure 2.2 and if the electric field is polarised perpendicular to the plane of incidence, then it is referred to as s-polarised light. The plane of incidence is also known as the scattering plane, the plane which contains the incident and reflected light beam. The reflected light ellipticity changes when the magnetization of the sample is reversed. The measured rotation is given by the Kerr angle (θ_K) and the ellipticity is $E_K = tan(S'/P')$, as defined in Figure 16.5.

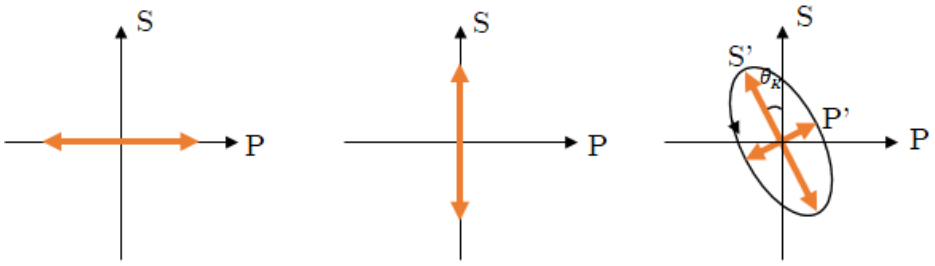

Figure 16.5: E-field vector of light in the plane transverse to the direction of propagation for linearly polarized light **a.**, as for incident p and s polarized light. **b.** Elliptically polarized light which is the general case for light reflected from a Kerr-active surface.

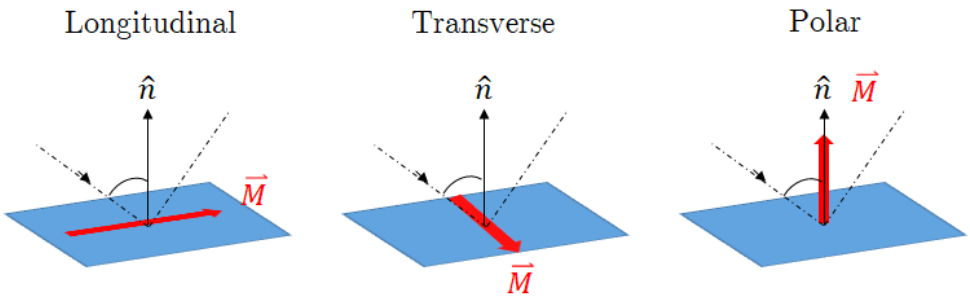

Figure 16.6: Longitudinal, transverse and polar MOKE geometries.

There are principally three Kerr effects which are classified depending on the geometry being employed between the sample plane and the magnetization. These are shown inFigure 16.6. The longitudinal and transverse Kerr effects are generally used to study the in-plane magnetic anisotropy, whereas the polar configuration is used to study thin films, which exhibit perpendicular anisotropy. In the longitudinal and polar geometries, the s or p polarized light will generally become elliptically polarised with its major axis rotated (Kerr rotation). This is a consequence of an orthogonal electric field component being induced because of the Lorentz force.

A schematic of the measurement setup is given in Figure 16.7. A beam of light (provided by a 15mW He-Ne laser ($\lambda = 640nm$)) passes through a polariser, that will define the s or

p polarization. A frequency modulation is used to improve the signal-to-noise ratio when the signal is driven to a lock-in amplifier (that can extract a signal with a known carrier wave from an extremely noisy environment). This modulation can be done by using a mechanical chopper (frequency up to 1 kHz) or photoelastic modulator (f $\approx$ 50 khz). The measurement area was determined by the size of the laser spot, that can be controlled by a set of lenses in the path between the chopper and the sample. The reflected light beam was passed through a second polariser (analyser) and is directed to a photo-diode, where the reflected intensity was measured. The output signal from the photo-diode previously minimized by rotating the analyser. The differences in the intensity gives the signal collected by the lock-in. The control of the equipments and data acquisition were made with LabView.

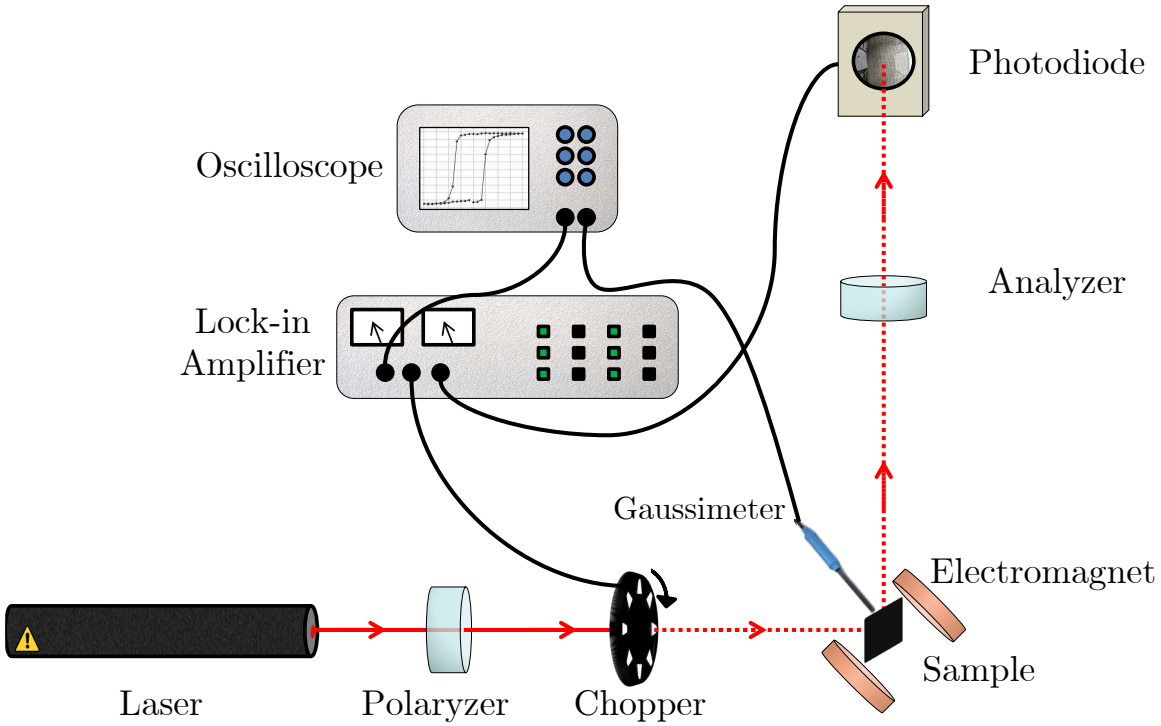

Figure 16.7: Schematics of the MOKE mounting. Adapted from [172]

A mathematical approach for the Kerr effect theory was first described macroscopically by using a dielectric tensor theory [335]. For a more complete description, see [172, 336–338].

16.2.4 Monte Carlo Simulation

Monte Carlo (MC) is a computational method that uses statistical modeling and probably density functions to estimate mathematical function and simulate complex systems by use of simulated random numbers to estimate some functions of a probability distribution. A more complete approach for the MC method can be found in [309, 339].

The problem is then solved by estimating the expected value of a quantity from the distribution of the random variable. In the thermal equilibrium, the expected value of an observable quantity is given by

$$\langle A \rangle = \frac{1}{\mathcal{Z}} \sum_i A_i e^{-\beta E_i} \tag{16.2}$$

where $\mathcal{Z} = \sum_\sigma e^{-\beta E_\sigma}$ is the canonical partition function. $\beta = 1/K_B T$ for K_B the Boltzmann constant and T the temperature. $\langle A \rangle$ is the expected value of the quantity A at an energy state E_i. The sum in i is done in all microstates of the system. The MC method consists in consider only the most relevant states in each temperature and calculate the the physical quantities of interest.

From a microstate $\mu(t = 0)$, the algorithm turns into a new state $\nu(t)$. The probability of the transition is $W_{\mu \to \nu}$. This procedure guarantee that, any other state can be found from a previous one by a finite number of steps. The stochastic process of the transition of states can be understood as the microscopical evolution of the system, being the probability $\mathcal{P}_\mu(t)$ to find the system in the state $\mu(t)$ in a given time t is:

$$\frac{\partial \mathcal{P}_\mu(t)}{\partial t} = \sum_{\mu \neq \nu} (\mathcal{P}_\mu W_{\mu \to \nu} - \mathcal{P}_\nu W_{\nu \to \mu}) \tag{16.3}$$

The dynamics of configurations is obtained by the transition rules in the algorithm to create a new configuration $\mu(t + \Delta t)$ from a previous $\mu(t)$. In the equilibrium,

$$\frac{\partial \mathcal{P}_\mu(t)}{dt} = 0 \tag{16.4}$$

and the probability of a $\mu(t)$-state be found in a classical system is

$$\mathcal{P}_\mu(t) = \frac{e^{-\beta E_\mu}}{\mathcal{Z}} \tag{16.5}$$

The Metropolis algorithm is used for calculate the transition probability of the spin flips in the simulations for a MC step (a computational measure of time) and updated after the system realize $2L^2$ attempts of flips in a single spin following the steps:

- Choose an initial configuration (random, for example)
- Choose a i site of the system
- Calculate the energy variation ΔE to flip a spin S_i
- Generate a random number n, from 0 to 1

- if $n < e^{-\beta \Delta E}$, the spin is flipped, otherwise stay in the previous configuration
- return to step 2

If this procedure is repeated N times (where N is the number of sites in the lattice), a MC step is done. The first configurations have to be discarded, it's the thermalization time. The determination of this time is important to ensure the system is in equilibrium and the results are trustable.

17 - Results

Some of artificial spin ices (ASI) magnetic properties (as a function of temperature T) are observed by Photoemission Electron Microscopy ($PEEM$) [340] combined with X-ray Magnetic Circular Dichroism ($XMCD$) measurements. We demonstrate here, theoretically (by Monte Carlo simulations) and experimentally that the geometry of the planar arrays may be an additional ingredient to transform an ASI material in a thermal system. Theoretically, it is done by deforming continuously the square lattice in a rectangular one. We experimentally focus on rectangular artificial spin ices ($RASI$) with horizontal and vertical lattice parameters given by a and b respectively. Our samples match in three classes of $RASI$, appropriately designed to illustrate what we interpret as a geometrothermodynamic effect. They are heated from room temperature until a temperature near $800K$ (just below the Curie Temperature of the permalloy, which is $T_C = 873K$).

For all kinds of planar ASI geometries, with ground states obeying the familiar 'two-in, two-out' ice rule in each vertex, the nanomagnets spin will experience less restriction to flip precisely in a kind of rhombic lattice. This can be observed by analysing only three types of rectangular artificial spin ices ($RASI$) described by its aspect ratio $\gamma \equiv a/b$.

By comparing the impact of thermal effects on the spin flips in these three appropriate different $RASI$ arrays, it is possible to find the phenomenon we call ASI **geometrothermodynamic**. The comparison is done among $RASI$ with $\gamma = \sqrt{2}$, $\gamma = \sqrt{3}$ and $\gamma = \sqrt{4}$.

Theoretical calculations [290] concerning the rectangular artificial systems have shown that the ice regime (with the required degenerate ground state) could be observed when the aspect ratio of the lattice ($\gamma \equiv a/b$) is equal to $\sqrt{3}$ (the rhombic lattice). On the other hand, the ground states of $RASI$ compounds with $1 < \gamma < \sqrt{3}$ and $\gamma > \sqrt{3}$ are not degenerate, but they have very distinct magnetic properties: in the first case ($1 < \gamma < \sqrt{3}$), there are residual magnetic charges at each vertex, alternating from positive to negative along the neighbor vertices. In the second case ($\gamma > \sqrt{3}$), there are alternating residual magnetic moments along the neighbor vertices. Again, looking the vertical and horizontal lines of spins, it can be characterized as a ferromagnetic state. At $\gamma = \sqrt{3}$, these two distinct types of states have the same energy and the

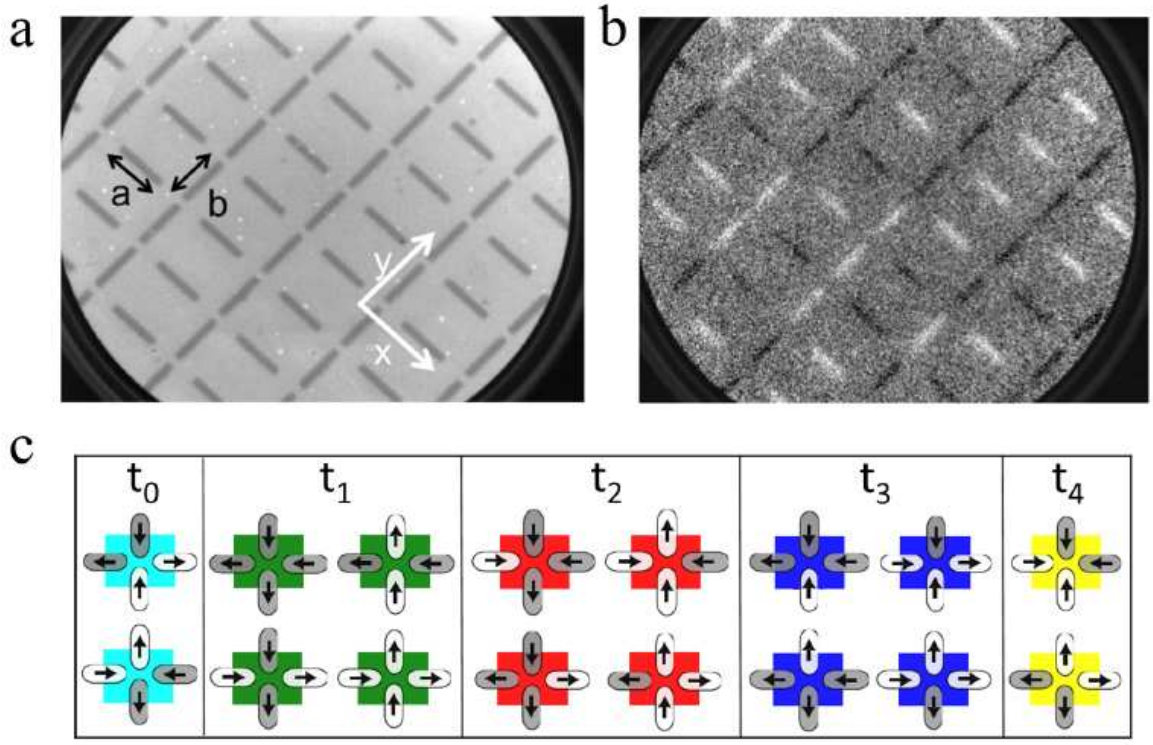

Figure 17.1: **a.** 30 μm x 30 μm $PEEM$ image of $\gamma = \sqrt{3}$ $RASI$ lattice. The Permalloy nanoislands have 2800 nm x 400 nm x 10 nm. **b.** Typical $XMCD$ measurement for the same area of (a) with the clear and dark contrast representing the orientation of the islands domains, in each direction. The measurement was taken with the array rotated 45 degrees from the X-ray sensitivity to resolve x and y direction at the same time. **c.** Topologies for each vertex, where red and blue arrows represents the orientation of the island, related to $XMCD$ pattern.

ground state becomes degenerated [301].

Figure 17.1a shows an image of a $RASI$ with $\gamma = \sqrt{3}$ obtained by $PEEM$ measurements combined with $XMCD$ technique (Figure 17.1b) showing the magnetic domais of the nanoislands. Figure 1c shows the five possible topologies of these structures. Topologies t_0 and t_1 obey the ice rule (two-in, two-out) while the other three (t_2, t_3 and t_4) represent excited states singly (t_2 and t_3) and doubly (t_4) charged magnetic monopoles [290]. Here, the t_2 and t_3 states, with $3in - 1out$ or vice versa are separated if compared with the T_3 topology of Figure 15.4 due to differences of energy. The energy of all these topologies depends on γ. For $\gamma = \gamma_R = \sqrt{3}$ (γ_R is the rhombic lattice), the t_0 and t_1 topologies have the same energy, yielding to a degenerate ground state.

17.1 Theoretical Approach

The thermodynamic results for $RASI$ obtained by MC simulations [1] are shown in Figure 17.2. For the usual artificial square ice, Silva *et al.* [268] have suggested the existence of a phase transition at a critical temperature $T_P \sim 7.2D/k_B = 7.2 \times 10^4 K$, where D is the coupling constant of the dipolar interaction. Indeed, the specific heat exhibits a sharp peak at T_P, whereas the amplitude diverges logarithmically with the system size L.

This phase transition was first attributed to the vanishing of the string tension between monopoles of opposite charges: below T_P, the monopoles are bonded by an energetic (and observable) string (Nambu monopoles [288]); above T_P, the string tension should vanish and some monopoles become almost free to move (actually, they may not be completely free because a monopole pair is subjected to an entropic force that exhibits, in two dimensions, a logarithmic distance dependence).

Concerning the specific heat, our MC calculations lead to similar behaviors for the $RASI$ materials. Figure 17.2 shows the specific heat as a function of temperature for the three different cases considered here. As expected, the critical temperature ($T_{\sqrt{n}}$, $n = 2, 3, 4$), at which the peaks occur is a function of the aspect ratio γ. Initially, as γ is increased from 1 (square ice), the critical temperature decreases [301].

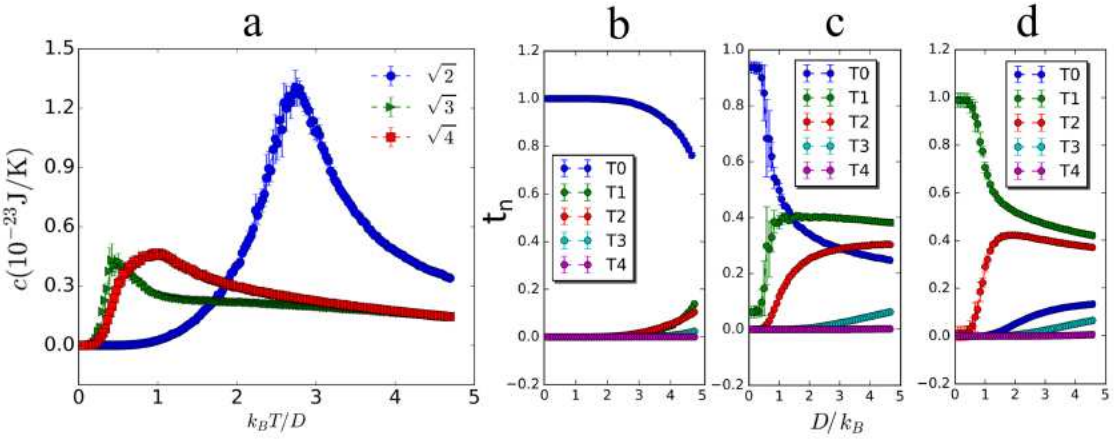

Figure 17.2: a. Specific heat of RASI with different values of γ obtained by Monte Carlo simulations. Parts **b**($\gamma = \sqrt{2}$), **c**($\gamma = \sqrt{3}$) and **d**($\gamma = \sqrt{4}$) shows the density of states for each topology in the lattices respectively, as a function of temperature.

This difference in the specific heats were expected because the coupling between nanoislands becomes weaker as the array becomes more stretched and islands are far from each other. How-

[1] The MC simulations were made in collaboration with Prof. Fabio S. Nascimento and Prof. Afrânio R. Pereira.

ever, we report that the minimum specific heat occurs when $\gamma = \sqrt{3}$, apart from this case, the idea of the critical temperature decrease with increasing γ works well. In this special $\gamma = \sqrt{3}$, the ground state is degenerated, as discussed above in the beginning of this section.

The rectangular ice magnets $\gamma = \sqrt{2}$ and $\sqrt{4}$ start (at T = 0) with all vertices in their respective natural ground states (the topologies t_0 and t_1, respectively). In all situations, as T is increased from zero, the other topologies start slowly to arise in the lattice. It occurs in different manners as γ changes. For $\gamma = \sqrt{2}$ the system practically remains entirely in its ground state for a large range of temperatures, in such a way that, the topology t_0 begins to really decrease only for high temperatures ($T > 3D/K_b$) almost like the square ice, this high temperature value for the emergence of excitations indicates that systems with relatively small aspect ratio ($\gamma \approx \sqrt{1}$ [341]) tend to be athermal, as frequently found in literature.

For the special case of $\gamma = \sqrt{3}$ the initial state (with most vertices in the topology t_0) reduces rapidly as T increases and, simultaneously, the density of the t_1 topology increases considerably. It suggests an immediate activity in the spin fluctuations, even at relatively low temperatures. For this particular case, any mixture of the states t_0 and t_1, if it is possible to occur, would also be a ground state. Note that the density of the ground state topologies (t_0 and t_1) starts to change just at the critical temperature (the peak on the Figure 17.2a). The t_2 and t_3 topologies start to be excited at higher temperatures, where it starts to indicate the emergence of monopoles with tensionless strings.

The basic differences are the ground states and the fact that the t_2 monopoles (red circles) are more easily excited in the array with $\gamma = \sqrt{3}$ conducting the system a lower transition temperature. The above theoretical calculations are very suggestive: the critical temperature of $\gamma = \sqrt{3}$ is about 15 times smaller than T_p, which means that the rhombic ice exhibits, at much lower temperatures, a richer dynamics than the square ice.

17.2 Experimental Results

With these indicative theoretical results in mind, we now consider experimental arrangements in which the temperature of the three types of RASI systems varies from 300K to 750K. This range of T is, in principle, about 10 - 100 times smaller than the temperature scale of the most theoretical calculations presented above, but it is below the Curie temperature (TC) of the permalloy.

The XMCD measurements (as discussed in Figure 16.4) were performed at PGM beamline of the Brazilian Synchrotron Light Laboratory [2]. The images were taken on the Nickel $L_{2,3}$ edge

[2] lnls.cnpem.br/en/

with a photon energy of 850eV. The islands array was placed rotated 45° related to the X-ray sensitivity in order to fully resolve both x and y directions (as shown in Figure 17.1). MOKE measurements were made in a custom built optical path with an special sample holder capable to heat the sample during the measurement under a low vacuum environment, to avoid degradation of the sample and possible smoke, which can interfere in the laser intensity. The measurements were made using a p-polarized source in a longitudinal geometry. The islands array were placed rotated 45° related to the scattering plane to fully resolve both x and y directions. The MOKE signal was recorded by varying the temperature in the sample.

The samples were fabricated with a size of 3000 nm x 400 nm x 10 nm to ensure that the orientation in each island is still a monodomain, even if it's bigger than the usual nanoislands in the literature. This size is due to the spacial sensitivity of the PEEM microscope as shown in Figure 17.3.

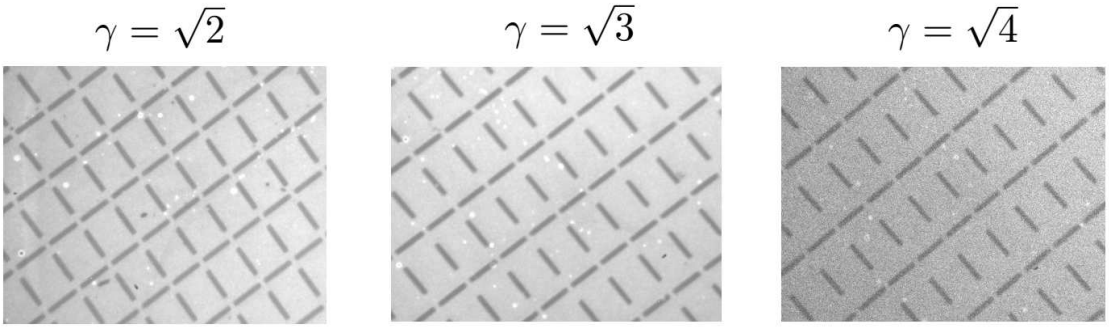

Figure 17.3: PEEM images for the $\gamma = \sqrt{2}$, $\gamma = \sqrt{3}$ and $\gamma = \sqrt{4}$ samples.

Figure 17.4a shows the snapshots of $\gamma = \sqrt{4}$ sample with the vertices mapping done following the scheme on Figure 17.2c. The images were obtained with samples initially at room temperature (RT) and heated to 473K, 573K, 623K and 673K. According to the theoretical calculations, the ground state of this array should have all vertices in the topology t_1, at T = 0 but At room temperature we can see that the t_1 topology is dominant. It is shown in this figure the temperature can actuate to generate fluctuations, creating and destroying all possible low energy excitations into the system, including monopole pairs with t_3 and t_4 topologies with the t_3 configuration density, the lowest energy monopole excitations increasing with T. To emphasize and illustrate the role of the thermal effects on the creation of excitations in RASI materials, we investigate experimentally how magnetized samples will be affected as the temperature is increased. Figure 17.4b present a comparison of vertex topologies for different RASI ratio at same temperature. Those measurements corroborate the prediction of higher density of high energetic topologies for the orthorhombic $\gamma = \sqrt{3}$ specially if compared to $\gamma = \sqrt{2}$ that show more low energy configurations, as discussed in Figure 17.2.

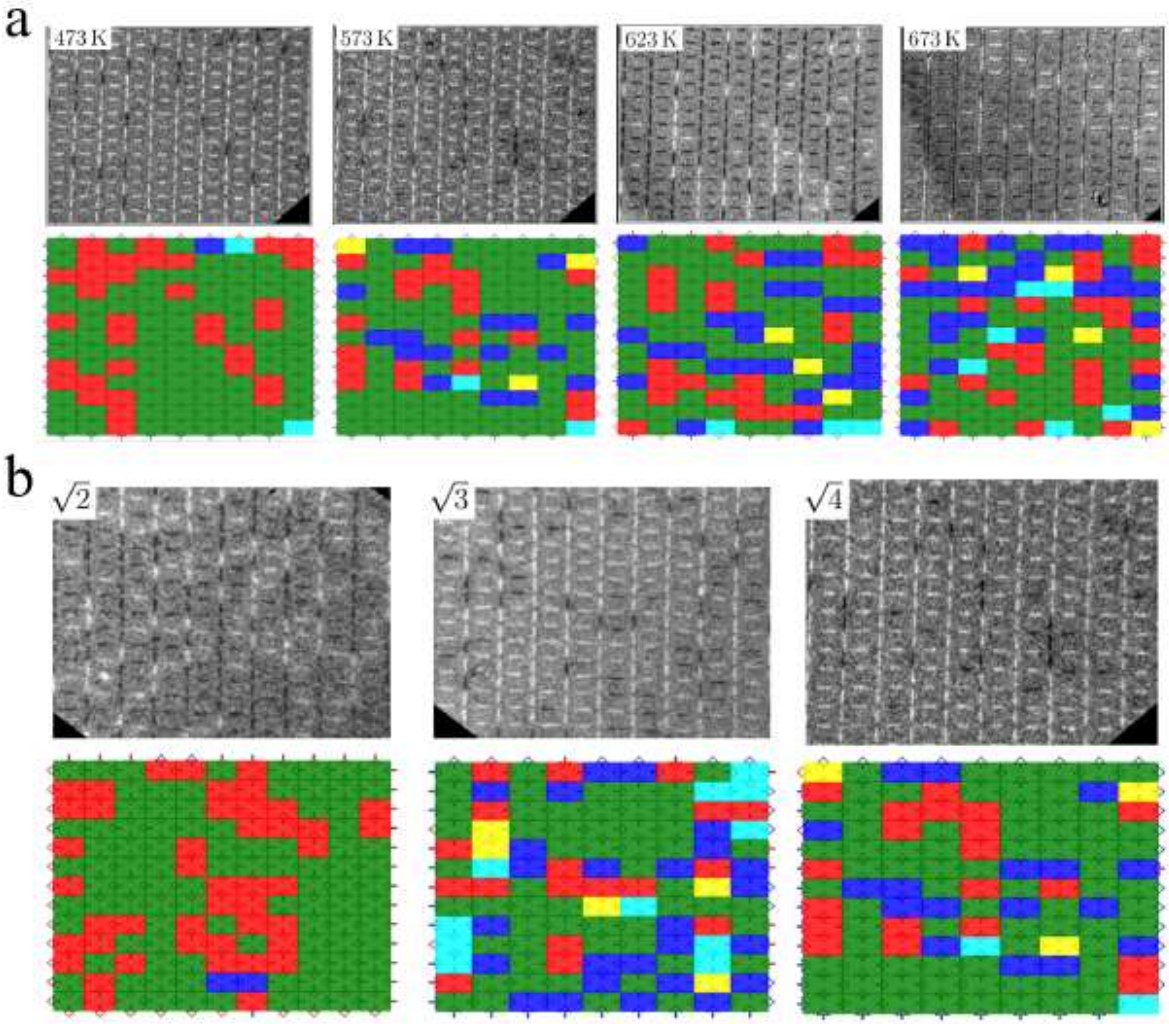

Figure 17.4: (**a.** 100 μm x 100 μm $XMCD$ images of $\gamma = \sqrt{4}$ $RASI$ at different temperatures. The respective magnetic configuration is shown below according to the color configuration shown in Figure 17.1. **b.** Images and vertices mapping for $\gamma = \sqrt{2}$, $\gamma = \sqrt{3}$ and$\gamma = \sqrt{4}$ for the same temperature of 573K.

Figure 17.5 shows the magnetization and the vertex population for each γ from the XMCD measurements taken, as shown in Figure 17.4. All samples were initially prepared (at RT) with normalized magnetization along one direction (Mx or My equal to 1), in such a way that the total normalized magnetization M_{tot} is around 0.8 (see red squares in the left side of Figure 17.5a). As the temperature is increased, the total magnetization decreases for the three cases but with different behaviors. Note that for the $\gamma = \sqrt{2}$ and $\sqrt{4}$ the magnetization in the x direction shows a maximum value, but for $\gamma = \sqrt{3}$, the magnetization in the y direction is maximum. In the $\gamma = \sqrt{2}$ the magnetization decreases very slowly as T increases. Meanwhile, there is a slow increasing of the monopoles number (t_2 and t_3 topologies). Such a behavior reveals that this system, like the square ice, is essentially athermal in the range of temperatures compatible with experiments in artificial spin ices. The magnetic moments of the nanoislands

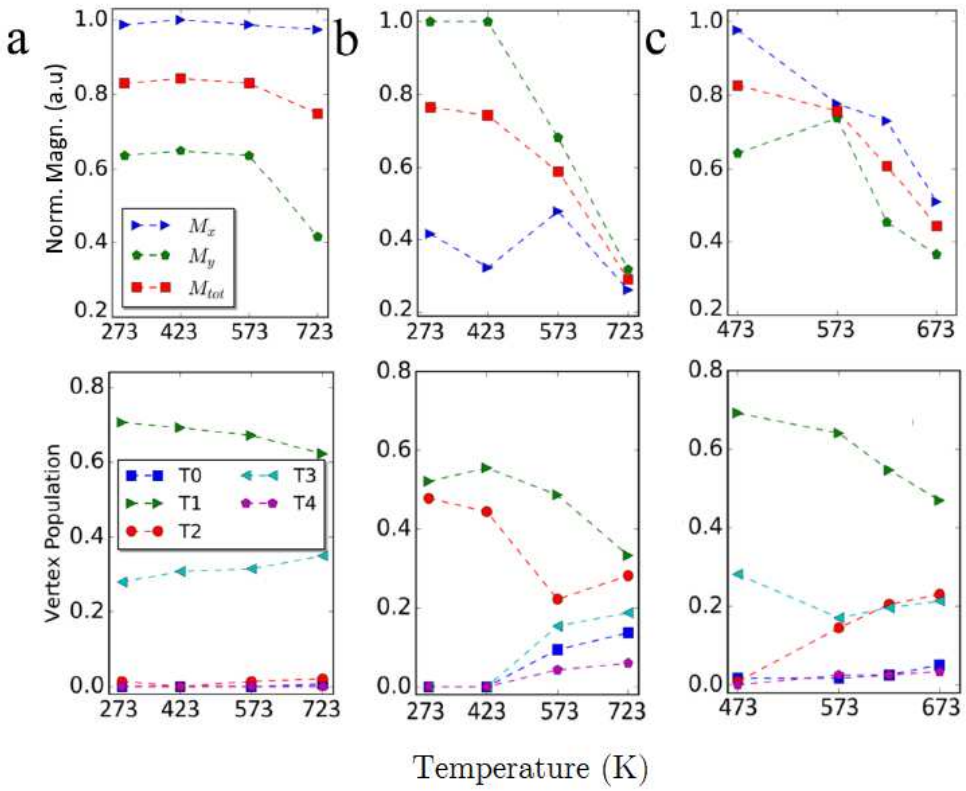

Figure 17.5: Normalized magnetization and population of topologies for lattices with **a.** $\gamma = \sqrt{2}$, **b.** $\gamma = \sqrt{3}$ and **c.** $\gamma = \sqrt{4}$ The magnetization and topologies are calculated from the XMCD measurements as shown in Figure 17.4

do not flip easily and the magnetization remains practically unchanged during all interval of temperatures studied. If the temperature is increased at higher values than the measured ones, the system will reach the Curie temperature for permalloy and individual nanoislands would turn to paramagnetic.

On the other hand, for the special case of $\gamma = \sqrt{3}$, the magnetization decreases very rapidly as T increases and seems to vanish even at a temperature below the Curie temperature of permalloy, while the monopoles population (including also doubly charged monopoles in t_4 topologies) increases considerably as T increases, mainly for T > 550K (right side of Figure 17.5).

This example shows clearly that the geometry may produce favourable conditions to flip the magnetic moments, making the system to exhibit its thermodynamic properties at temperatures lower than the material Curie' temperature. To confirm this fact, we have also investigated the case $\gamma = \sqrt{4}$ and it suggests that, for $\gamma > \sqrt{3}$, the magnetization decreases slower as T increases, similar for $\gamma < \sqrt{3}$, but it falls much more quickly.

We then notice that the experimental data obtained for the magnetization can be connected with the theoretical calculations for the specific heat in the way that the temperature in which M_{tot} goes to zero and the specific heat presents a peak is a minimum for the same $\gamma = \sqrt{3}$. These

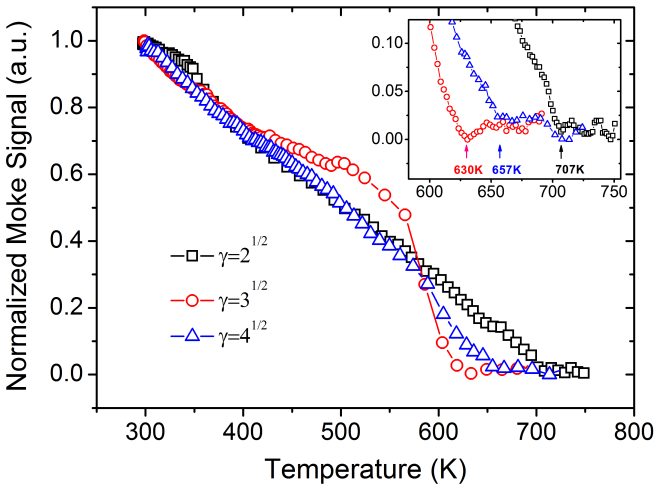

Figure 17.6: $MOKE$ signal as function of temperature for the three lattices compared. Here $T_{\sqrt{2}} \approx 707K$, $T_{\sqrt{3}} \approx 630K$ and $T_{\sqrt{4}} \approx 657K$.

thermodynamical features are caused by purely geometrical effects, since in our measurements, no other parameter was changed, emphasizing the idea that the string tension tends to vanish for the $\gamma = \sqrt{3}$ RASI.

Another way to confirm our predictions is to measure the total magnetization of the system while the temperature was increased. For this we built a MOKE system (as discussed in Figure 16.7) with a sample holder capable to increase the temperature in the sample without destroying it. A low vacuum environment with a glass chamber was built to allow the light to pass through by using a pyrex glass, that can hold high temperatures. The sample was then saturated with the islands rotated 45° rotated in relation to the magnetic field and the scattering plane to fully saturate both directions. The MOKE signal was recorded while the temperature was increased. The sample was placed in a metal plate, connected to a Tungsten connected to a current source, responsible to the heating. The sample was placed in such a way that all in-plane contributions of the magnetic field, generated by the heating filament, were removed.

The MOKE results are shown in Figure 17.6. These results also confirm the geometrothermodynamic effect observed in the MC simulations and XMCD measurements while the total magnetization turns to zero in the $\gamma = \sqrt{3}$ at lower temperatures than other γ also below permalloy Curie temperature. Note that, even the $\gamma = \sqrt{2}$, considered to be athermal have a critical temperature below permalloy T_c.

18 - Discussion and Perspectives

Despite possible small deviations in theory, since $\gamma = \sqrt{3}$ is not a rational number and, therefore, any calculation of the specific heat is not done exactly at the correct value in which the system degenerates, the smooth bump presented in the specific heat of $\gamma = \sqrt{3}$ lattice instead of sharp peak in the other configurations, is due to the absence of phase transition to the ice state, being present just a crossover. This is a strong evidence that the orthorombic geometry allows the ice state. Such imprecision are also present in experiments, because the measurements of distances between islands have the errors of the instruments and, in addition, the nanoislands are not point dipoles, although they are monodomains.

So, all results concerning the lattices analysed are close approximations. Despite these difficulties, our results show clearly (theoretically as well as experimentally) some roles of geometry on the thermodynamic properties of these systems.

For the simulations, the use of any rational number r very close to $\sqrt{3}$ will imply that the system is only near to the ice regime, but it still keeps some features of the antiferromagnetic (if r is immediately below $\sqrt{3}$ or ferromagnetic phase if r is immediately above $\gamma = \sqrt{3}$).

Here, we have demonstrated experimentally that the lattice geometry can be an important ingredient to transform the usually 'solid' (a phase whereas the ASI constituent spins are almost inflexible) artificial spin ice compounds into a 'liquid' (the islands magnetization are governed by the dipolar interaction with less trouble, fluctuating even for practical laboratory tempera-

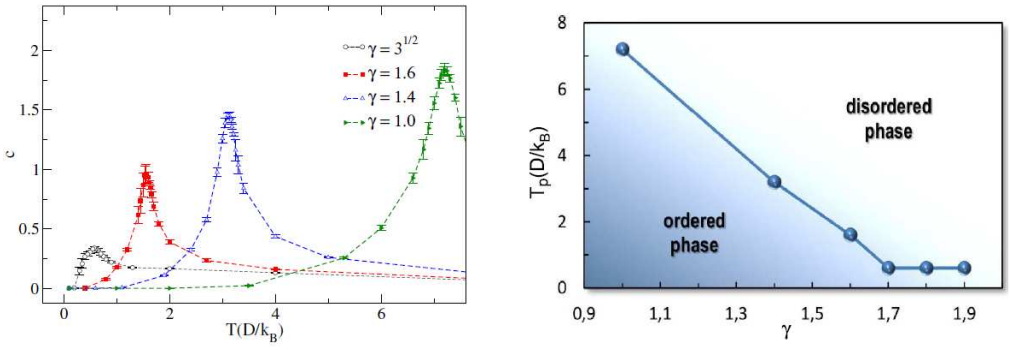

Figure 18.1: Specific heat in function of temperature calculated by Fabio Nascimento [290, 301] for different γ and the temperature of the specific heat peak in function of γ.

tures) system, just by changing one of the components of the lattice parameter, in other words, stretching an square lattice in one direction.

Normally, ASI materials are athermal ('solid') and the spins do not flip easily because a nanoisland contains a large number of atoms. On the other hand, it has been shown that an unambiguous stretching of the square ice may take the system to the ice regime.

Part IV

Conclusion

This thesis covers three important and extensively research topics of magnetism and topology, with proposal of its application in spintronics devices.

Regarding the fisrt part of this work, as the geometries and materials parameters utilized in this work are similar to the skyrmion imprinting proposed and experimentally demonstrated [66–68], this method for the creation of the RMS is expected to work at room temperature. Additionally, the advantage of this new feature is the increase in the integration density, once there is no need of a third electrode to apply perpendicular current for the spin texture creation as in the most skyrmion-based devices proposed so far and being faster to transport than the usual domain walls systems.

The electric currents necessary for RMS generation and motion are consistent with those utilized in DW racetrack memories. The proposed method and device are promising for applications in future racetrack memories with controlled RMS density for creation and high tunnel magnetoresistance signal for detection. We have also presented an alternative to storage data, since the RMS is not stable without electrical current, by converting into an domain wall by an constriction junction.

This new proposed device is suitable for new kinds of memory devices and also with works related to topological structures. Since this kind of structure requires an spin polarized current, researches are necessary to improve this electrical polarization with more efficient spin injection device, like spin pumpin process in topological insulatores as we have published in Phys. Rev. B 96, 180415(R) [342]. Spin pumping can be bettter described in [343, 344].

It's important to notice that this system is free from skyrmion hall effect. It can happens in our system if we include a small DMI ($\approx 0.1mJ/m^2$). For practical applications in racetracks, the moving structure should travel along a straight line and systems free from skyrmion hall effect are already being researched for the realization of skyrmion dynamics without SkHE.

In the second part we have demonstrated the conversion of a spin current into a charge current in the topological insulator $(Bi_{0.22}Sb_{0.78})_2Te_3$ at room temperature. The spin currents were generated in a thin layer of permalloy by two different processes, the spin pumping effect (SPE) and the spin Seebeck effect (SSE). The TI surface was used to detection because of the spin-momentum locking of the surface states and we believe the IEE will be very useful for electrical detection of spin current and spin accumulation in future spintronics devices.

From the third part, we can see that only a change in geometry must be responsible for the different behaviors of these $RASI$ systems. The rhombic lattice makes equidistant the four spins meeting at a vertex, similar to the three-dimensional natural and even artificial spin ices. This geometric effect has shown to be more effective in inducing spin fluctuations than the usual

way of purely increasing the lattice spacing among the nanoislands. Although all the evidences obtained here suggest that the $\gamma = \sqrt{3}$ is in the ice regime, we must be very careful in stating that.

The dynamics of those systems in function of geometrical parameters show that the change in the geometry can be a simple way to control the dynamics and the ground state of this systems, in this case, by stretching the square lattice. Such systems could be more appropriate for magnetronics application, once the monopoles connection have no energy, so they would have more freedom in the lattice.

In conclusion, topology physics and its related effects are at the front of the newest researches on “spintronics”, where devices that operate with spin (rather than charge) currents, “skyrmionics”, where the information can be carried by magnetic excitations or “magnetricity” where magnetic charges (monopoles) can be used as an analogue to electrical charge carriers. Those elements alone or integrated will require a lot of research, as happened with the semiconductor technology few decades ago, leading to a new generation of quantum materials devices.

A - Publications

Journal of Magnetism and Magnetic Materials 455 (2018) 25–31

Contents lists available at ScienceDirect

Journal of Magnetism and Magnetic Materials

journal homepage: www.elsevier.com/locate/jmmm

Research articles

Creation, transport and detection of imprinted magnetic solitons stabilized by spin-polarized current

R.P. Loreto [a], W.A. Moura-Melo [a], A.R. Pereira [a], X. Zhang [b], Y. Zhou [b], M. Ezawa [c], C.I.L. de Araujo [a,*]

[a] Departamento de Física, Universidade Federal de Viçosa, Viçosa, 36570-900 Minas Gerais, Brazil
[b] School of Science and Engineering, The Chinese University of Hong Kong, Shenzhen 518172, China
[c] Department of Applied Physics, The University of Tokyo, 7-3-1 Hongo, Tokyo 113-8656, Japan

ARTICLE INFO

Article history:
Received 25 February 2017
Received in revised form 17 April 2017
Accepted 27 April 2017
Available online 29 April 2017

Keywords:
Magnetic soliton
Skyrmion
Bubble
Racetrack memory
Spintronics

ABSTRACT

With the recent proposition of skyrmion utilization in racetrack memories at room temperature, skyrmionics has become a very attractive field. However, for the stability of skyrmions, it is essential to incorporate the Dzyaloshinskii–Moriya interaction (DMI) and the out-of-plane magnetic field into the system. In this work, we explore a system without these interactions. First, we propose a controlled way for the creation of magnetic skyrmions and skyrmioniums imprinted on a ferromagnetic nanotrack via a nanopatterned nanodisk with the magnetic vortex state. Then we investigate the detachment of the imprinted spin textures from the underneath of the nanodisk, as well as its transport by the spin-transfer torque imposed by spin-polarized current pulses applied in the nanotrack. A prominent feature of the moving imprinted spin texture is that its topological number Q is oscillating around the averaged value of $Q = 0$ as if it is a resonant state between the skyrmions with $Q = \pm 1$ and the bubble with $Q = 0$. We may call it a resonant magnetic soliton (RMS). A RMS moves along a straight line since it is free from the skyrmion Hall effect. In our studied device, the same electrodes are employed to realize the imprinted spin texture detachment and its transport. In addition, we have investigated the interaction between the RMS and a magnetic tunnel junction sensor, where the passing of the RMS in the nanotrack can be well detected. Our results would be useful for the development of novel spintronic devices based on moveable spin textures.

1. Introduction

The magnetic skyrmion [1,2], a sort of soliton with protected structural stability assured by its topological configuration, was recently observed in chiral magnetic materials [3–8] with the Dzyaloshinskii–Moriya interaction (DMI) [9,10] at low temperatures. Moreover, experimental observations performed at room temperature, in materials with both perpendicular magnetic anisotropy (PMA) and DMI [11–13], together with the topological protection and fast transport [14,15], have pointed out skyrmions as the most prominent magnetic structures to be exploited for building magnetic storage devices, such as the racetrack memories [16]. The magnetic domain wall-based racetrack memory is an established technique [17–20]. The merit of the skyrmion compared with the domain wall is that the skyrmion is not easy to be pinned by defects or impurities [21]. The manipulation of a single isolated skyrmion is a key for skyrmionics [22–26]. The logic computing application and electric devices based on skyrmions make skyrmionics future promising spintronic devices [27–30].

Recent experimental works have demonstrated new methods for the generation of single isolated skyrmion [31], skyrmions form on a nanotrack with PMA using protocol of out-of-plane magnetic saturation and successive magnetic field reversion. Another promising experimental method [32] is the transformation of skyrmions from chiral domain walls in a nanotrack with the geometrical constriction. However, in all these experimental works carried out so far, an out-of-plane magnetic field is required to maintain the stability of skyrmions.

In this work, using full micromagnetic simulations, we propose to transport a new type of magnetic spin textures through a nanotrack where both the DMI and the out-of-plane magnetic field are absent. First, we create a skyrmion or a skyrmionium by the interaction between a magnetic nanotrack with PMA and a soft magnetic nanodisk with vortex state attached to it, as shown in Fig. 1. This method of creating a skyrmion imprinted by a nanopatterned nanodisk on a CoPt thin film has already been investigated by numerical simulations [33] as well as experiments demonstrated at

* Corresponding author.
E-mail address: dearaujo@ufv.br (C.I.L. de Araujo).

http://dx.doi.org/10.1016/j.jmmm.2017.04.074
0304-8853/

PHYSICAL REVIEW B **96**, 180415(R) (2017)

Dirac-surface-state-dominated spin to charge current conversion in the topological insulator $(Bi_{0.22}Sb_{0.78})_2Te_3$ films at room temperature

J. B. S. Mendes,[1,*] O. Alves Santos,[2] J. Holanda,[2] R. P. Loreto,[1] C. I. L. de Araujo,[1] Cui-Zu Chang,[3,4] J. S. Moodera,[3,5] A. Azevedo,[2] and S. M. Rezende[2]

[1]*Departamento de Física, Universidade Federal de Viçosa, 36570-900 Viçosa, MG, Brazil*

[2]*Departamento de Física, Universidade Federal de Pernambuco, 50670-901 Recife, PE, Brazil*

[3]*Francis Bitter Magnet Laboratory, Massachusetts Institute of Technology, Cambridge, Massachusetts 02139, USA*

[4]*Department of Physics, The Pennsylvania State University, University Park, Pennsylvania 16802, USA*

[5]*Department of Physics, Massachusetts Institute of Technology, Cambridge, Massachusetts 02139, USA*

(Received 16 August 2017; published 28 November 2017)

We report the spin-to-charge current conversion in an intrinsic topological insulator (TI) $(Bi_{0.22}Sb_{0.78})_2Te_3$ film at room temperature. The spin currents are generated in a thin layer of permalloy (Py) by two different processes, the spin pumping effect (SPE) and the spin Seebeck effect (SSE). In the first, we use microwave-driven ferromagnetic resonance of the Py film to generate a SPE spin current that is injected into the TI $(Bi_{0.22}Sb_{0.78})_2Te_3$ layer in direct contact with Py. In the second, we use the SSE in the longitudinal configuration in Py without contamination by the anomalous Nernst effect, which was made possible with a thin NiO layer between the Py and $(Bi_{0.22}Sb_{0.78})_2Te_3$ layers. The spin-to-charge current conversion is dominated by the TI surface states and is attributed to the inverse Edelstein effect (IEE), which is made possible by the spin-momentum locking in the electron Fermi contours due to the Rashba field. The measurements by the two techniques yield very similar values for the IEE parameter, which are larger than the reported values in the previous studies on topological insulators.

DOI: 10.1103/PhysRevB.96.180415

Topological insulators (TIs) constitute a novel state of matter, which have been the subject of intensive investigations in condensed matter physics in the last decade. They are a new class of quantum materials that present insulating bulk, but metallic, dissipationless surface states topologically protected by time reversal symmetry, opening several possibilities for practical applications in many scientific arenas including spintronics, quantum computation, magnetic monopoles, and highly correlated electron systems [1–4]. More recently, it has been shown that TI particles behave as optically induced oscillators in optical tweezers [5]. The surface states are characterized by a single gapless Dirac cone and exhibit remarkable spin-momentum locking: The charge carriers move in such a way that their momenta are always perpendicular to their spin [4,6]. In addition, topological insulators have strong spin-orbit coupling (SOC) and as well as have a large spin torque, which are essential for efficient spin-charge conversion [7–9].

In turn, the conversion of charge currents into spin currents, and vice versa, are key phenomena for encoding and decoding information carried by electron spins in the active field of spintronics. Until recently, the only known mechanisms for conversion in both directions were the spin Hall effect (SHE) and its Onsager reciprocal, the inverse spin Hall effect (ISHE), which rely on electron scattering processes with spin-orbit interactions in three-dimensional (3D) materials [10–14]. Studies of the spin-to-charge conversion by the ISHE have been conducted in metallic films with heavy elements, such as paramagnetic Pt, Pd, and Ta [15–27], ferromagnetic Py [28], antiferromagnetic materials such as IrMn and PtMn [29,30], and semiconductors [31–37]. Recent developments in thin-film growth techniques have made possible the fabrication of samples with atomically flat surfaces and interfaces that have led to the observation of new phenomena induced by SOC in two-dimensional (2D) systems [38–40]. Among them are the Edelstein effect, predicted some time ago [41], and its Onsager reciprocal, the inverse Edelstein effect, that enable new means to convert charge currents into spin currents, and vice versa.

The direct Edelstein effect and the inverse Edelstein effect (IEE) are made possible by the Rashba effect that arises from SOC and broken inversion symmetry at material surfaces and interfaces [42–45]. The Rashba field produces spin-momentum locking in the electron Fermi contours that enables the conversion between spin and charge currents. The conversion of spin currents produced by ferromagnetic resonance (FMR) spin pumping into charge currents due to the IEE has been observed at Bi/Ag interfaces [46], single-layer graphene [47], and in a few TIs [8,48–50]. In this Rapid Communication, we report the observation of spin-to-charge current conversion by means of the IEE in the topological insulator $(Bi_{0.22}Sb_{0.78})_2Te_3$ at room temperature. The spin currents are generated by two different arrangements, microwave-driven spin pumping and the spin Seebeck effect.

The experiments were carried out with two sample structures, (i) one consisting of a TI grown on a 0.5-mm-thick sapphire (0001) substrate and with a $Ni_{81}Fe_{19}$ (permalloy-Py) top layer, and (ii) a trilayer in which a NiO layer is grown between the TI and the Py layers. In both, we have used a commercial 0.5-mm-thick (0001) sapphire substrate onto which the TI is grown as follows. After high-temperature annealing ($\sim$800 °C) of the sapphire substrate, a six-quintuple layer (QL)-thick $(Bi_xSb_{1-x})_2Te_3$ film is grown on top at a temperature $\sim$230 °C in a custom-built ultrahigh vacuum molecular beam epitaxy (MBE) system and capped by a 3-nm-thick epitaxial Te layer. X-ray diffraction patterns confirm the

*Corresponding author: joaquim.mendes@ufv.br

Geometrothermodynamics in planar artificial spin ices

R. P. Loreto,[1] F.S. Nascimento,[2] J. Borme,[3] J. C. Cezar,[4] C. Nisoli,[5] A. R. Pereira,[1,*] and C.I.L. de Araujo[1,†]

[1]*Laboratory of Spintronics and Nanomagnetism (LabSpiN), Departamento de Física, Universidade Federal de Viçosa, 36570-000 - Viçosa - Minas Gerais - Brazil.*
[2]*Departamento de Física, Universidade Federal de Ouro Preto, 35931-008 - João Monlevade - Minas Gerais - Brazil.*
[3]*INL-International Iberian Nanotechnology Laboratory, 4715-330, Braga, Portugal*
[4]*Laboratório Nacional de Luz Síncrotron-LNLS, CP 6192, 13083-970 Campinas, Brazil*
[5]*Theoretical Division and Institute for Materials Science, Los Alamos National Laboratory, Los Alamos, New Mexico 87545, USA*

(Dated: March 7, 2018)

Geometry induced dynamics yields remarkable physical phenomena. In the macrocosms, the curvature of spacetime (geometrodynamics) tells matter how to move (gravity). In the microcosms, an example is the geometrical frustration in magnetic materials, whereas under certain conditions, can lead to the formation of spin liquids, in which the constituent spins still fluctuate strongly down to a temperature of absolute zero. In this work, we would like to explore a geometrical effect in artificial spin ices (ASI). It is well known that, in general, such artificial materials are athermal because they are constructed with elongated nanomagnets containing a large number of atomic spins, generating a big net magnetic moment that need a great amount of energy to flip. Therefore, recently, thermally driven dynamics in ASI materials became an important subject of investigation. We then expand this picture by showing that geometrically driven dynamics in ASI can open up the panorama of exploring distinct ground states and thermally magnetic monopole excitations. Here, it is shown that a particular ASI lattice, whereas four spins meet at every vertex, will provide a richer thermodynamics only due to its geometry. Indeed, for all kinds of planar ASI geometries, with ground states obeying the familiar 'two-in, two-out' ice rule in each vertex, the nanomagnets spin will experience less restriction to flip precisely in a kind of rhombic lattice. This can be observed by analysing only three types of rectangular artificial spin ices ($RASI$). Denoting the horizontal and vertical lattice spacings by a and b, respectively, then, a $RASI$ material can be described by its aspect ratio $\gamma \equiv a/b$. The rhombic lattice emerges when $\gamma = \sqrt{3}$. So, by comparing the impact of thermal effects on the spin flips in these three appropriate different $RASI$ arrays, it is possible to find the phenomenon we call ASI geometrothermodynamic. The comparison is done among $RASI$ with $\gamma = \sqrt{2}$, $\gamma = \gamma_R = \sqrt{3}$ and $\gamma = \sqrt{4}$. The experimental data and the direct imaging of individual nanomagnets and their magnetization are obtained, as a function of temperature, by using Photoemission Electron Microscopy ($PEEM$) combined with X-ray Magnetic Circular Dichroism ($XMCD$) and Magneto-optic Kerr effect ($MOKE$) measurements. Our experimental data corroborates the unusual behavior of the critical temperatures in the $RASI$ materials investigated here, as predicted by our Monte Carlo simulations.

INTRODUCTION

Arrays of nanomagnets designed to resemble the spin ice materials (disordered magnetic states) are known as artificial spin ices (ASI). Nowadays, with the advances of the nanotechnology and nanofabrication, ASI systems have become so famous as well as their natural counterparts, with the advantage that they can be constructed with desirable geometries and properties. The first ASI was built in 2006 and it consists of a two-dimensional ($2d$) square array of $80,000$ elongated magnetic nanoislands, each a few hundred nanometers long[1]. The net magnetic moment (spin) of each individual nanoisland is aligned parallel to its longest axis (like in a bar magnet), and is coupled to all other nanoislands of the planar array by the ubiquitous dipolar interaction. Then, in its original configuration, ASI tiles a square lattice of vertices, with four nanoislands meeting at each vertex. The ground state of this artificial square ice obeys the ice rule, which remains the familiar two-in, two-out (two spins must point in, while the other two must point out in each vertex). However, in two dimensions, the standard ice rule is no longer degenerate[1–3]. This trouble comes together with the fact that this peculiar material is also athermal. Indeed, the magnetic moments involved are roughly a million times bigger than those of the ions forming the natural spin ices and, therefore, they interact much more strongly, having less tendency to flip. Therefore, to anneal the material into its ground state, the usual approach is not available because the kinetic barriers of individual islands are on the order of $10^4 K$. Hence, ASI compounds have almost always been found in frozen at room temperature. So, to advance our understanding (by studying ASI materials) of how geometrical frustration operates to produce new states of matter, at least, two initial difficulties should be experimentally overcome: first, it would be essential to construct arrays with degenerate ground states and, second, it would be important to develop methods to investigate the thermal fluctuations and dynamics of the nanoislands magnetic moment. Probably, these two points must be connected in some way. Recently, several works have given attention to certain thermal properties of ASI compounds in diverse types of planar lattices[4–12]. However, the $2d$ lattice obeying the usual two-in, two-out ice rule with a degenerated ground state did

* apereira@ufv.br.
† dearaujo@ufv.br

References

[1] B. Dieny *et al.*, "Giant magnetoresistive in soft ferromagnetic multilayers," *Phys. Rev. B*, **43**: 1297–1300 (1991).

[2] M. N. Baibich *et al.*, "Giant Magnetoresistance of (001)Fe/(001)Cr Magnetic Superlattices," *Phys. Rev. Lett.*, **61**: 2472–2475 (1988).

[3] G. Binasch, P. Grünberg, F. Saurenbach and W. Zinn, "Enhanced magnetoresistance in layered magnetic structures with antiferromagnetic interlayer exchange," *Phys. Rev. B*, **39**: 4828–4830 (1989).

[4] J. S. Moodera, L. R. Kinder, T. M. Wong and R. Meservey, "Large magnetoresistance at room temperature in ferromagnetic thin film tunnel junctions," *Physical Review Letters*, **74** (16): 3273–3276 (1995).

[5] S. S. Parkin *et al.*, "Exchange-biased magnetic tunnel junctions and application to nonvolatile magnetic random access memory (invited)," *Journal of Applied Physics*, **85** (8): 5828–5833 (1999).

[6] I. L. Prejbeanu *et al.*, "Thermally assisted MRAMs: ultimate scalability and logic functionalities," *Journal of Physics D: Applied Physics*, **46** (7): 074002 (2013).

[7] J. Slonczewski, "Current-driven excitation of magnetic multilayers," *Journal of Magnetism and Magnetic Materials*, **159** (1-2): L1–L7 (1996).

[8] L. Berger, "Emission of spin waves by a magnetic multilayer traversed by a current," *Phys. Rev. B*, **54**: 9353–9358 (1996).

[9] Y. Tserkovnyak, A. Brataas and G. E. W. Bauer, "Enhanced Gilbert Damping in Thin Ferromagnetic Films," *Phys. Rev. Lett.*, **88**: 117601 (2002).

[10] W. H. Rippard, M. R. Pufall and S. E. Russek, "Comparison of frequency, linewidth, and output power in measurements of spin-transfer nanocontact oscillators," *Phys. Rev. B*, **74**: 224409 (2006).

[11] A. V. Nazarov *et al.*, "Spin transfer stimulated microwave emission in MgO magnetic tunnel junctions," *Applied Physics Letters*, **88** (16): 162504 (2006).

[12] C. Boone *et al.*, "Experimental test of an analytical theory of spin-torque-oscillator dynamics," *Phys. Rev. B*, **79**: 140404 (2009).

[13] M. Asorey, "Space, matter and topology," *Nature Physics*, **12** (7): 616 (2016).

[14] Editorial, "Topology on top," *Nature Physics*, **12** (7) (2016).

[15] Editorial, "Stranger things," *Nature Materials*, **16** (11) (2017).

[16] S. C. Zhang, "Topological states of quantum matter," *Physics*, **1**: 6 (2008).

[17] N. Nagaosa and Y. Tokura, "Topological properties and dynamics of magnetic skyrmions," *Nature Nanotechnology*, **8** (12): 899–911 (2013).

[18] P. Milde *et al.*, "Unwinding of a skyrmion lattice by magnetic monopoles," *Science*, **340** (6136): 1076–1080 (2013).

[19] B. Keimer and J. E. Moore, "The physics of quantum materials," *Nature Physics*, **13** (11): 1045–1055 (2017).

[20] Editorial, "The rise of the quantum materials," *Nature Physics*, **12** (7) (2016).

[21] S. Parkin, M. Hayashi and L. Thomas, "Magnetic domain-wall racetrack memory," *Science*, **320** (5873): 190–194 (2008).

[22] A. Fert, V. Cros and J. Sampaio, "Skyrmions on the track," *Nature Nanotechnology*, **8** (3): 152–156 (2013).

[23] A. R. Mellnik *et al.*, "Spin-transfer torque generated by a topological insulator," *Nature*, **511** (7510): 449–451 (2014).

[24] C. H. Li *et al.*, "Electrical detection of charge-current-induced spin polarization due to spin-momentum locking in Bi2Se3," *Nature Nanotechnology*, **9** (3): 218–224 (2014).

[25] A. Dankert *et al.*, "Room temperature electrical detection of spin polarized currents in topological insulators," *Nano Letters*, **15** (12): 7976–7981 (2015).

[26] H. Wang *et al.*, "Surface-State-Dominated Spin-Charge Current Conversion in Topological-Insulator-Ferromagnetic-Insulator Heterostructures," *Physical Review Letters*, **117** (7): 2–6 (2016).

[27] Y. Fan *et al.*, "Electric-field control of spin-orbit torque in a magnetically doped topological insulator," *Nature Nanotechnology*, **11** (4): 352–359 (2016).

[28] C. H. Li *et al.*, "Direct comparison of current-induced spin polarization in topological insulator Bi 2 Se 3 and InAs Rashba states," *Nature Communications*, **7**: 1–8 (2016).

[29] D. Singleton, "Topological electric charge," *International Journal of Theoretical Physics*, **34** (12): 2453–2466 (1995).

[30] R. C. O´ Handley, Modern Soft Magnetic Materials, John Wiley & Sons (2000).

[31] A. Aharoni, Introduction to the Theory of Ferromagnetism, Oxford University Press (1996).

[32] C. Kittel, Introdução à física do estado sólido, LTC (2006).

[33] E. A. da Silva Oliveira, A influência da Interação entre Segundos Vizinhos na Termodinâmica e na Dinâmica de Redes de Skyrmions, Ph.D. thesis, Universidade Federal de Viçosa (2017).

[34] N. Spaldin, Magnetic Materials: Fundamentals and Applications, Cambridge University Press (2010).

[35] N. D. Mermin and H. Wagner, "Absence of Ferromagnetism or Antiferromagnetism in One- or Two-Dimensional Isotropic Heisenberg Models," *Phys. Rev. Lett.*, **17**: 1307–1307 (1966).

[36] I. Dzyaloshinsky, "A thermodynamic theory of weak ferromagnetism of antiferromagnetics," *Journal of Physics and Chemistry of Solids*, **4** (4): 241–255 (1958).

[37] T. Moriya, "Anisotropic superexchange interaction and weak ferromagnetism," *Physical Review*, **120** (1): 91–98 (1960).

[38] V. Fedorov *et al.*, "Interaction between the spin chirality and the elastic torsion," *Physics Letters A*, **224** (6): 372–378 (1997).

[39] L. M. Sandratskii, "Insight into the Dzyaloshinskii-Moriya interaction through first-principles study of chiral magnetic structures," *Physical Review B*, **96** (2): 1–13 (2017).

[40] S. W. Cheong and M. Mostovoy, "Multiferroics: A magnetic twist for ferroelectricity," *Nature Materials*, **6** (1): 13–20 (2007).

[41] M. T. Johnson, P. J. H. Bloemen, F. J. A. den Broeder and J. J. de Vries, "Magnetic anisotropy in metallic multilayers," *Reports on Progress in Physics*, **59** (11): 1409–1458 (1996).

[42] F. J. den Broeder, W. Hoving and P. J. Bloemen, "Magnetic anisotropy of multilayers," *Journal of Magnetism and Magnetic Materials*, **93** (C): 562–570 (1991).

[43] "The Moore's Law of Big Data," http://www.ni.com/newsletter/51649/en/, accessed: March, 1^{st}, 2018.

[44] https://datascience.berkeley.edu/moores-law-processing-power/, accessed: March, 1^{st}, 2018.

[45] https://datascience.berkeley.edu/big-data-infographic, accessed: March, 1^{st}, 2018.

[46] S. Tehrani *et al.*, "Progress and Outlook for MRAM Technology," *IEEE Trans. Mag.*, **35** (5): 6 (1999).

[47] V. Uhlíř *et al.*, "Dynamic switching of the spin circulation in tapered magnetic nanodisks," *Nature Nanotechnology*, **8** (5): 341–346 (2013).

[48] C. I. De Araujo, S. G. Alves, L. D. Buda-Prejbeanu and B. Dieny, "Multilevel Thermally Assisted Magnetoresistive Random-Access Memory Based on Exchange-Biased Vortex Configurations," *Physical Review Applied*, **6** (2): 1–9 (2016).

[49] J. G. Zhu, "Magnetoresistive random access memory: The path to competitiveness and scalability," *Proceedings of the IEEE*, **96** (11): 1786–1798 (2008).

[50] J. P. Liu, Z. Zhang and G. Zhao, Skyrmions: Topological Structures, Properties, and Applications, CRC Press (2016).

[51] M. Hayashi *et al.*, "Current-Controlled Magnetic Domain-Wall Nanowire Shift Register," *Science*, **320** (5873): 209–211 (2008).

[52] S.-H. Yang, K.-S. Ryu and S. Parkin, "Domain-wall velocities of up to 750 ms^{-1} driven by exchange-coupling torque in synthetic antiferromagnets," *Nature Nanotechnology*, **10** (3): 221–226 (2015).

[53] T. Skyrme, "A unified field theory of mesons and baryons," *Nuclear Physics*, **31**: 556–569 (1962).

[54] D. Cortés-Ortuño *et al.*, "Thermal stability and topological protection of skyrmions in nanotracks," *Scientific Reports*, **7** (1): 1–13 (2017).

[55] I. Kézsmárki *et al.*, "Néel-type skyrmion lattice with confined orientation in the polar magnetic semiconductor GaV4S8," *Nature Materials*, **14** (11): 1116–1122 (2015).

[56] S. Mühlbauer *et al.*, "Skyrmion Lattice in a Chiral Magnet," *Science*, **323** (5916): 915–919 (2009).

[57] A. Neubauer *et al.*, "Topological Hall Effect in the A Phase of MnSi," *Phys. Rev. Lett.*, **102**: 186602 (2009).

[58] F. Jonietz *et al.*, "Spin Transfer Torques in MnSi at Ultralow Current Densities," *Science*, **330** (6011): 1648–1651 (2010).

[59] X. Z. Yu *et al.*, "Real-space observation of a two-dimensional skyrmion crystal," *Nature*, **465** (7300): 901–904 (2010).

[60] W. Münzer *et al.*, "Skyrmion lattice in the doped semiconductor $Fe_{1-x}Co_xSi$," *Phys. Rev. B*, **81**: 041203 (2010).

[61] C. Pfleiderer *et al.*, "Skyrmion lattices in metallic and semiconducting B20 transition metal compounds," *Journal of Physics Condensed Matter*, **22** (16) (2010).

[62] X. Z. Yu *et al.*, "Near room-temperature formation of a skyrmion crystal in thin-films of the helimagnet FeGe," *Nature Materials*, **10** (2): 106–109 (2011).

[63] X. Yu *et al.*, "Skyrmion flow near room temperature in an ultralow current density," *Nature Communications*, **3**: 988 (2012).

[64] G. Chen, A. Mascaraque, A. T. N'Diaye and A. K. Schmid, "Room temperature skyrmion ground state stabilized through interlayer exchange coupling," *Applied Physics Letters*, **106** (24): 242404 (2015).

[65] Y. Tokunaga *et al.*, "A new class of chiral materials hosting magnetic skyrmions beyond room temperature," *Nature Communications*, **6** (May): 1–7 (2015).

[66] L. Sun *et al.*, "Creating an artificial two-dimensional skyrmion crystal by nanopatterning," *Physical Review Letters*, **110** (16): 1–5 (2013).

[67] B. F. Miao *et al.*, "Experimental realization of two-dimensional artificial skyrmion crystals at room temperature," *Physical Review B - Condensed Matter and Materials Physics*, **90** (17): 1–5 (2014).

[68] D. A. Gilbert *et al.*, "Realization of ground-state artificial skyrmion lattices at room temperature," *Nature Communications*, **6** (May): 8462 (2015).

[69] Y. Y. Dai *et al.*, "Skyrmion ground state and gyration of skyrmions in magnetic nanodisks without the Dzyaloshinsky-Moriya interaction," *Physical Review B - Condensed Matter and Materials Physics*, **88** (5): 1–8 (2013).

[70] R. P. Cowburn *et al.*, "Single-Domain Circular Nanomagnets," *Phys. Rev. Lett.*, **83**: 1042–1045 (1999).

[71] J. Sampaio *et al.*, "Nucleation, stability and current-induced motion of isolated magnetic skyrmions in nanostructures." *Nature nanotechnology*, **8** (11): 839–44 (2013).

[72] N. Romming *et al.*, "Writing and Deleting Single Magnetic Skyrmions," *Science*, **341** (6146): 636–639 (2013).

[73] J. Iwasaki, M. Mochizuki and N. Nagaosa, "Universal current-velocity relation of skyrmion motion in chiral magnets," *Nature Communications*, **4**: 1463–1468 (2013).

[74] R. Tomasello *et al.*, "A strategy for the design of skyrmion racetrack memories," *Scientific Reports*, **4**: 1–7 (2014).

[75] S.-Z. Lin, C. Reichhardt, C. D. Batista and A. Saxena, "Particle model for skyrmions in metallic chiral magnets: Dynamics, pinning, and creep," *Phys. Rev. B*, **87**: 214419 (2013).

[76] X. Zhang *et al.*, "Skyrmion-skyrmion and skyrmion-edge repulsions in skyrmion-based racetrack memory." *Scientific reports*, **5**: 7643 (2015).

[77] S. Woo *et al.*, "Observation of room-temperature magnetic skyrmions and their current-driven dynamics in ultrathin metallic ferromagnets," *Nature Materials*, **15** (5): 501–506 (2016).

[78] X. Zhang, M. Ezawa and Y. Zhou, "Magnetic skyrmion logic gates: Conversion, duplication and merging of skyrmions," *Scientific Reports*, **5** (2015).

[79] W. Kang *et al.*, "Complementary Skyrmion Racetrack Memory with Voltage Manipulation," *IEEE Electron Device Letters*, **37** (7): 924–927 (2016).

[80] X. Xing, P. W. Pong and Y. Zhou, "Skyrmion domain wall collision and domain wall-gated skyrmion logic," *Physical Review B*, **94** (5): 1–11 (2016).

[81] X. Zhang *et al.*, "Magnetic skyrmion transistor: Skyrmion motion in a voltage-gated nanotrack," *Scientific Reports*, **5**: 1–8 (2015).

[82] D. Wei, "Maxwell Equations and Landau–Lifshitz Equations," in "Micromagnetics and Recording Materials," (edited by D. Wei), volume 1, pp. 21–52, Springer, Berlin, Heidelberg (2012).

[83] A. N, "Zur Atomtheorie des Ferromagnetismus," *Zeitschrift für Physik*, **54** (7): 582 (1929).

[84] A. N, "Zur Theorie der Magnetisierungskurve," *Zeitschrift für Physik*, **62** (3): 253 (1929).

[85] F. Bloch, "Zur Theorie des Austauschproblems und der Remanenzerscheinung der Ferromagnetika," *Zeitschrift für Physik*, **74** (5): 295 (1932).

[86] L. Landau and E. Lifshits, "on the Theory of the Dispersion of Magnetic Permeability in Ferromagnetic Bodies," *Phys. Zeitsch. der Sow.*, **169** (14): 14–22 (1935).

[87] W. F. Brown and A. E. LaBonte, "Structure and Energy of One –Dimensional Domain Walls in Ferromagnetic Thin Films," *Journal of Applied Physics*, **36** (4): 1380–1386 (1965).

[88] T. Gilbert, "Classics in Magnetics A Phenomenological Theory of Damping in Ferromagnetic Materials," *IEEE Transactions on Magnetics*, **40** (6): 3443–3449 (2004).

[89] C. H. Back, K. Perzlmaier and M. Buess, "Dynamic Aspects of Magnetism," in "Magnetism: A Synchrotron Radiation Approach," (edited by E. Beaurepaire, H. Bulou, F. Scheurer and J.-P. Kappler), volume 697, pp. 321–343, Springer, Berlin, Heidelberg (2006).

[90] S. Zhang, P. M. Levy and A. Fert, "Mechanisms of Spin-Polarized Current-Driven Magnetization Switching," *Phys. Rev. Lett.*, **88**: 236601 (2002).

[91] P. Chureemart, R. F. L. Evans and R. W. Chantrell, "Dynamics of domain wall driven by spin-transfer torque," *Phys. Rev. B*, **83**: 184416 (2011).

[92] S. Petit *et al.*, "Spin-Torque Influence on the High-Frequency Magnetization Fluctuations in Magnetic Tunnel Junctions," *Phys. Rev. Lett.*, **98**: 077203 (2007).

[93] A. M. Deac *et al.*, "Bias-driven high-power microwave emission from MgO-based tunnel magnetoresistance devices," *Nature Physics*, **4** (10): 803–809 (2008).

[94] M. A. Zimmler *et al.*, "Current-induced effective magnetic fields in CoCuCo nanopillars," *Phys. Rev. B*, **70**: 184438 (2004).

[95] S. Urazhdin, N. O. Birge, W. P. Pratt and J. Bass, "Current-Driven Magnetic Excitations in Permalloy-Based Multilayer Nanopillars," *Phys. Rev. Lett.*, **91**: 146803 (2003).

[96] Y. Zhou, Spin momentum transfer effects for spintronic device applications, Ph.D. thesis, KTH Royal Institute of Technology of Stockholm (2009).

[97] J. Xiao, A. Zangwill and M. D. Stiles, "Boltzmann test of Slonczewski's theory of spin-transfer torque," *Phys. Rev. B*, **70**: 172405 (2004).

[98] D. Pinna, Spin-Torque Driven Macrospin Dynamics subject to Thermal Noise, Ph.D. thesis, New York University (2015).

[99] M. D. Stiles and A. Zangwill, "Anatomy of spin-transfer torque," *Physical Review B - Condensed Matter and Materials Physics*, **66** (1): 144071–1440714 (2002).

[100] D. C. Ralph and M. D. Stiles, "Spin transfer torques," *Journal of Magnetism and Magnetic Materials*, **320** (7): 1190–1216 (2008).

[101] S. Zhang and Z. Li, "Roles of Nonequilibrium Conduction Electrons on the Magnetization Dynamics of Ferromagnets," *Phys. Rev. Lett.*, **93**: 127204 (2004).

[102] Z. Li and S. Zhang, "Magnetization dynamics with a spin-transfer torque," *Phys. Rev. B*, **68**: 024404 (2003).

[103] Y. Liu and Z. Zhang, "Micromagnetic modeling of magnetization dynamics driven by spin-transfer torque in magnetic nanostructures," *Science China: Physics, Mechanics and Astronomy*, **56** (1): 184–195 (2013).

[104] Z. D. Li, P. B. He and W. M. Liu, "Dynamics of magnetization in ferromagnet with spin-transfer torque," *Chinese Physics B*, **23** (11) (2014).

[105] A. Vansteenkiste and B. Van de Wiele, "MuMax: a new high-performance micromagnetic simulation tool," *Journal of Magnetism and Magnetic Materials*, **323** (21): 2585–2591 (2011).

[106] J. H. Conway and N. J. A. Sloane, Sphere Packings, Lattices, and Groups, Springer, New York, 2 edition (1993).

[107] G. Bertotti, Hysteresis in Magnetism, Elsevier (1998).

[108] A. Makarov, Modeling of Emerging Resistive Switching Based Memory Cells, Ph.D. thesis, Technischen Universität Wien (2017).

[109] S. Rohart and A. Thiaville, "Skyrmion confinement in ultrathin film nanostructures in the presence of Dzyaloshinskii-Moriya interaction," *Physical Review B - Condensed Matter and Materials Physics*, **88** (18): 1–8 (2013).

[110] G. Chen, "Spin-orbitronics: Skyrmion Hall effect," *Nature Physics*, **13** (2): 112–113 (2017).

[111] X. Zhang, Y. Zhou and M. Ezawa, "Magnetic bilayer-skyrmions without skyrmion Hall effect," *Nature Communications*, **7**: 1–7 (2016).

[112] J. Barker and O. A. Tretiakov, "Static and Dynamical Properties of Antiferromagnetic Skyrmions in the Presence of Applied Current and Temperature," *Physical Review Letters*, **116** (14): 1–5 (2016).

[113] J. Zang, M. Mostovoy, J. H. Han and N. Nagaosa, "Dynamics of Skyrmion crystals in metallic thin films," *Physical Review Letters*, **107** (13): 1–5 (2011).

[114] W. Jiang *et al.*, "Direct observation of the skyrmion Hall effect," *Nature Physics*, **13** (2): 162–169 (2016).

[115] K. Litzius *et al.*, "Skyrmion Hall effect revealed by direct time-resolved X-ray microscopy," *Nature Physics*, **13** (2): 170–175 (2017).

[116] A. A. Thiele, "Steady-State Motion of Magnetic Domains," *Phys. Rev. Lett.*, **30**: 230–233 (1973).

[117] C. Schütte, J. Iwasaki, A. Rosch and N. Nagaosa, "Inertia, diffusion, and dynamics of a driven skyrmion," *Physical Review B - Condensed Matter and Materials Physics*, **90** (17) (2014).

[118] A. Fert, V. Cros and J. Sampaio, "Skyrmions on the track," *Nature Nanotechnology*, **8** (3): 152–156 (2013).

[119] Y. Zhou and M. Ezawa, "A reversible conversion between a skyrmion and a domain-wall pair in junction geometry," *Nature Communications*, **5**: 1–8 (2014).

[120] M. Finazzi *et al.*, "Laser-induced magnetic nanostructures with tunable topological properties," *Physical Review Letters*, **110** (17): 1–5 (2013).

[121] Y. Zhou *et al.*, "Dynamically stabilized magnetic skyrmions," *Nature Communications*, **6**: 8193 (2015).

[122] R. Rajaraman, Solitons and Instantons: An Introduction to Solitons and Instantons in Quantum Field Theory, North Holland (1987).

[123] K. Everschor, Current-Induced Dynamics of Chiral Magnetic Structures: Skyrmions, Emergent Electrodynamics and Spin-Transfer Torques, Ph.D. thesis, University of Cologne (2012).

[124] X. Zhang *et al.*, "Control and manipulation of a magnetic skyrmionium in nanostructures," *Physical Review B*, **94** (9) (2016).

[125] M. Shen *et al.*, "Motion of a skyrmionium driven by spin wave," *Applied Physics Letters*, **112** (6): 062403 (2018).

[126] S. Zhang, F. Kronast, G. van der Laan and T. Hesjedal, "Real-Space Observation of Skyrmionium in a Ferromagnet Magnetic Topological Insulator Heterostructure," *Nano Letters*, **18** (2): 1057–1063 (2018).

[127] J. Zang, M. Mostovoy, J. H. Han and N. Nagaosa, "Dynamics of Skyrmion crystals in metallic thin films," *Physical Review Letters*, **107** (13): 1–5 (2011).

[128] G. Tatara *et al.*, "Threshold current of domain wall motion under extrinsic pinning, β-term and non-adiabaticity," *Journal of the Physical Society of Japan*, **75** (6): 1–7 (2006).

[129] N. Romming *et al.*, "Field-dependent size and shape of single magnetic Skyrmions," *Physical Review Letters*, **114** (17): 1–5 (2015).

[130] C. Moreau-Luchaire *et al.*, "Additive interfacial chiral interaction in multilayers for stabilization of small individual skyrmions at room temperature," *Nature Nanotechnology*, **11** (5): 444–448 (2016).

[131] O. Heinonen *et al.*, "Generation of magnetic skyrmion bubbles by inhomogeneous spin Hall currents," *Physical Review B*, **93** (9): 1–6 (2016).

[132] W. Jiang *et al.*, "Blowing magnetic skyrmion bubbles," *Science*, **349** (6245): 283–286 (2015).

[133] E. Y. Tsymbal and I. Zutic, Handbook of spin transport and magnetism, CRC press (2011).

[134] O. V. Pylypovskyi, D. D. Sheka and Y. Gaididei, "Bloch point structure in a magnetic nanosphere," *Physical Review B - Condensed Matter and Materials Physics*, **85** (22): 1–8 (2012).

[135] A. B. Shevchenko and M. Y. Barabash, "The Bloch point in uniaxial ferromagnets as a quantum mechanical object," *Nanoscale Research Letters*, **9** (1): 1–6 (2014).

[136] F. Willems *et al.*, "Probing ultrafast spin dynamics with high-harmonic magnetic circular dichroism spectroscopy," *Physical Review B - Condensed Matter and Materials Physics*, **92** (22): 1–5 (2015).

[137] H. Yang *et al.*, "Anatomy of Dzyaloshinskii-Moriya Interaction at Co/Pt Interfaces," *Physical Review Letters*, **115** (26): 1–5 (2015).

[138] R. M. Rowan-Robinson *et al.*, "The interfacial nature of proximity-induced magnetism and the Dzyaloshinskii-Moriya interaction at the Pt/Co interface," *Scientific Reports*, **7** (1): 1–11 (2017).

[139] L. Néel, "Magnetic surface anisotropy and superlattice formation by orientation." *J. Phys. Radium*, **15** (4): 225 – 239 (1954).

[140] M. Nakayama *et al.*, "Spin transfer switching in TbCoFe/CoFeB/MgO/CoFeB/TbCoFe magnetic tunnel junctions with perpendicular magnetic anisotropy," *J. Appl. Phys.*, **103** (7): 101–104 (2008).

[141] S. Ikeda *et al.*, "A perpendicular-anisotropy CoFeB-MgO magnetic tunnel junction," *Nat. Mater.*, **9** (9): 721–724 (2010).

[142] T. Nozaki *et al.*, "Large Voltage-Induced Changes in the Perpendicular Magnetic Anisotropy of an MgO-Based Tunnel Junction with an Ultrathin Fe Layer," *Phys. Rev. Appl.*, **5** (4): 044006 (2016).

[143] B. D. Dmytro Apalkov and J. M. Slaughter, "Magnetoresistive Random Access Memory (invited)," *Proc. IEEE*, **104** (10): 685–697 (2016).

[144] M. Gottwald *et al.*, "Magnetoresistive effects in perpendicularly magnetized Tb-Co alloy based thin films and spin valves," *J. Appl. Phys.*, **111** (8): 083904 (2012).

[145] C. F. Pai, M. Mann, A. J. Tan and G. S. Beach, "Determination of spin torque efficiencies in heterostructures with perpendicular magnetic anisotropy," *Phys. Rev. B*, **93** (14): 144409 (2016).

[146] Y. C. Lau *et al.*, "Spin-orbit torque switching without an external field using interlayer exchange coupling," *Nat. Nanotechnol.*, **11** (9): 758–762 (2016).

[147] C. O. Avci *et al.*, "torques in a perpendicular anisotropy magnetic insulator / Pt bilayer Fast switching and signature of efficient domain wall motion driven by spin-orbit torques in a perpendicular anisotropy magnetic insulator / Pt bilayer," *Appl. Phys. Lett.*, **111** (7): 072406 (2017).

[148] P. Sethi *et al.*, "Bi-directional high speed domain wall motion in perpendicular magnetic anisotropy Co/Pt double stack structures," *Sci. Rep.*, **7** (1): 4964 (2017).

[149] C. Y. You, "Switching current density reduction in perpendicular magnetic anisotropy spin transfer torque magnetic tunneling junctions," *J. Appl. Phys.*, **115** (4): 043914 (2014).

[150] S. Peng *et al.*, "Interfacial Perpendicular Magnetic Anisotropy of 1x nm Tunnel Junctions for Large-Capacity STT-MRAMs," *IEEE Magn. Lett.*, **7** (2016): 3105805 (2017).

[151] A. A. Timopheev *et al.*, "Inhomogeneous free layer in perpendicular magnetic tunnel junctions and its impact on the effective anisotropies and spin transfer torque switching efficiency," *Phys. Rev. B*, **96** (1): 014412 (2017).

[152] S. Iwasaki and K. Ouchi, "Co-Cr recording films with perpendicular magnetic anisotropy," *IEEE Transactions on Magnetics*, **14** (5): 849–851 (1978).

[153] P. F. Carcia, A. D. Meinhaldt and A. Suna, "Perpendicular magnetic anisotropy in Pd/Co thin film layered structures," *Applied Physics Letters*, **47** (2): 178–180 (1985).

[154] F. J. A. Den Broeder, H. C. Donkersloot, H. J. G. Draaisma and W. J. M. De Jonge, "Magnetic properties and structure of Pd/Co and Pd/Fe multilayers," *Journal of Applied Physics*, **61** (8): 4317–4319 (1987).

[155] P. F. Carcia, "Perpendicular magnetic anisotropy in Pd/Co and Pt/Co thin-film layered structures," *Journal of Applied Physics*, **63** (10): 5066–5073 (1988).

[156] W. B. Zeper, F. J. A. M. Greidanus, P. F. Carcia and C. R. Fincher, "Perpendicular magnetic anisotropy and magneto-optical Kerr effect of vapor-deposited Co/Pt-layered structures," *Journal of Applied Physics*, **65** (12): 4971–4975 (1989).

[157] F. J. A. Den Broeder, D. Kuiper, A. P. Van De Mosselaer and W. Hoving, "Perpendicular magnetic anisotropy of Co-Au multilayers induced by interface sharpening," *Physical Review Letters*, **60** (26): 2769–2772 (1988).

[158] H. X. Yang *et al.*, "First-principles investigation of the very large perpendicular magnetic anisotropy at Fe/MgO and Co/MgO interfaces," *Phys. Rev. B*, **84** (5): 054401 (2011).

[159] H. Sato *et al.*, "Perpendicular-anisotropy CoFeB-MgO magnetic tunnel junctions with a MgO/CoFeB/Ta/CoFeB/MgO recording structure," *Appl. Phys. Lett.*, **101** (2): 022414 (2012).

[160] J. M. Shaw *et al.*, "Perpendicular Magnetic Anisotropy and Easy Cone State in Ta/Co 60 Fe 20 B 20 /MgO," *IEEE Magn. Lett.*, **6**: 3500404 (1–4) (2015).

[161] B. Dieny and M. Chshiev, "Perpendicular magnetic anisotropy at transition metal/oxide interfaces and applications," *Rev. Mod. Phys.*, **89** (2): 025008 (2017).

[162] M. Yoshikawa *et al.*, "Tunnel magnetoresistance over 100% in MgO-based magnetic tunnel junction films with perpendicular magnetic L10-FePt electrodes," *IEEE Trans. Magn.*, **44** (11 PART 2): 2573–2576 (2008).

[163] G. Kim *et al.*, "Tunneling magnetoresistance of magnetic tunnel junctions using perpendicular magnetization L10-CoPt electrodes," *Appl. Phys. Lett.*, **92** (17): 172502 (2008).

[164] Z. Shan and D. Sellmyer, "Magnetism of rare-earth-transition-metal nanoscale multilayers. I. Experiments on y/Co, Dy/Fe, and Tb/Fe," *Phys. Rev. B*, **42** (16): 10434 (1990).

[165] S. Mangin *et al.*, "Engineered materials for all-optical helicity-dependent magnetic switching," *Nat. Mater.*, **13** (3): 286–292 (2014).

[166] Y. Suzuki, S. Takayama, F. Kirino and N. Ohta, "Single ION model for perpendicular magnetic anisotropy in RE-TM amorphous films," *IEEE Trans. Magn.*, **23** (5): 2275–2277 (1987).

[167] Z. Zhao *et al.*, "Spin Hall switching of the magnetization in Ta / TbFeCo structures with bulk perpendicular anisotropy Spin Hall switching of the magnetization in Ta / TbFeCo structures with bulk perpendicular anisotropy," *Appl. Phys. Lett.*, **132404** (2015): 132404 (2015).

[168] K. Ueda *et al.*, "Spin-orbit torques in Ta/TbxCo100-x ferrimagnetic alloy films with bulk perpendicular magnetic anisotropy," *Appl. Phys. Lett.*, **109** (23): 232403 (2016).

[169] J. Finley and L. Liu, "Spin-Orbit-Torque Efficiency in Compensated Ferrimagnetic Cobalt-Terbium Alloys," *Phys. Rev. Appl.*, **6** (5): 1–6 (2016).

[170] M. Schwartz, N. V. Myung and K. Nobe, "Electrodeposition of Iron Group-Rare Earth Alloys from Aqueous Media," *J. Electrochem. Soc.*, **151** (7): C468 (2004).

[171] A. Mallik and B. C. Ray, "Evolution of Principle and Practice of Electrodeposited Thin Film: A Review on Effect of Temperature and Sonication," *Int. J. Electrochem.*, **2011**: 1–16 (2011).

[172] J. R. de Toledo, Estudo da Magnetização Estática e Dinâmica de Clussters de Fe-Ni Obtidos via Eletrodeposição, Master's thesis, Universidade Federal de Viçosa (2017).

[173] R. Mishra and E. J. Podlaha, "Coupled Partial Current Density Behavior of Cobalt-Terbium Alloy Codeposition," *Journal of The Electrochemical Society*, **153** (6): C422 (2006).

[174] K. Freitas *et al.*, "Static and Dynamic Magnetization Investigation in Permalloy Electrodeposited onto High Resistive N-Type Silicon Substrates," *Coatings*, **7** (2): 33 (2017).

[175] M. Tang *et al.*, "Manipulation of perpendicular exchange bias effect in [Co/Ni]N/(Cu, Ta)/TbCo multilayer structures," *AIP Advances*, **5**: 087153 (2015).

[176] A. Hassdenteufel *et al.*, "Thermally Assisted All-Optical Helicity Dependent Magnetic Switching in Amorphous Fe 100- x Tb x Alloy Films," *Advanced Materials*, **25** (22): 3122–3128 (2013).

[177] C. D. Stanciu *et al.*, "All-optical magnetic recording with circularly polarized light," *Physical Review Letters*, **99** (4): 1–4 (2007).

[178] P. Bessarab *et al.*, "Stability and Lifetime of Antiferromagnetic Skyrmions," *arXiv preprint arXiv:1709.04454* (2017).

[179] B. Göbel, A. Mook, J. Henk and I. Mertig, "Antiferromagnetic skyrmion crystals: Generation, topological Hall, and topological spin Hall effect," *Physical Review B*, **96** (6): 060406 (2017).

[180] H. Y. Hwang, S.-W. Cheong, N. P. Ong and B. Batlogg, "Spin-Polarized Intergrain Tunneling in $\mathrm{La_{2/3}Sr_{1/3}MnO_3}$," *Phys. Rev. Lett.*, **77**: 2041–2044 (1996).

[181] J. M. De Teresa *et al.*, "Inverse Tunnel Magnetoresistance in $\mathrm{Co/SrTiO_3/La_{0.7}Sr_{0.3}MnO_3}$: New Ideas on Spin-Polarized Tunneling," *Phys. Rev. Lett.*, **82**: 4288–4291 (1999).

[182] M. Bowen *et al.*, "Nearly total spin polarization in La2/3Sr1/3MnO3from tunneling experiments," *Applied Physics Letters*, **82** (2): 233–235 (2003).

[183] Y. Sakuraba *et al.*, "Huge spin-polarization of L21-ordered Co2MnSi epitaxial heusler alloy film," *Japanese Journal of Applied Physics, Part 2: Letters*, **44** (33-36) (2005).

[184] T. M. Nakatani *et al.*, "Structure, magnetic property, and spin polarization of Co2 FeAlx Si1-x Heusler alloys," *Journal of Applied Physics*, **102** (3): 1–8 (2007).

[185] V. Ko, G. Han and Y. P. Feng, "Electronic band structure matching for half- and full-Heusler alloys," *Journal of Magnetism and Magnetic Materials*, **322** (20): 2989–2993 (2010).

[186] M. N. Rasool, A. Hussain, A. Javed and M. A. Khan, "Study of the structural, electronic and magnetic properties of ScFeCrT (T=Si, Ge) Heusler alloys by first principles approach," *Journal of Magnetism and Magnetic Materials*, **426** (October 2016): 421–428 (2017).

[187] R. Ooka *et al.*, "Magnetization and Spin Polarization of Heusler Alloys Co2TiSn and Co2TiGa0.5Sn0.5," *IEEE Magnetics Letters*, **8**: 5–9 (2017).

[188] B. L. Zink *et al.*, "Efficient spin transport through native oxides of nickel and permalloy with platinum and gold overlayers," *Physical Review B*, **93** (18): 1–16 (2016).

[189] S. A. Wolf *et al.*, "Spintronics: A spin-based electronics vision for the future," *Science*, **294** (5546): 1488–1495 (2001).

[190] Y. K. Kato, R. C. Myers, A. C. Gossard and D. D. Awschalom, "Current-Induced Spin Polarization in Strained Semiconductors," *Phys. Rev. Lett.*, **93**: 176601 (2004).

[191] Y. K. Kato, R. C. Myers, A. C. Gossard and D. D. Awschalom, "Observation of the spin hall effect in semiconductors," *Science*, **306** (5703): 1910–1913 (2004).

[192] B. D. Cullity and C. D. Graham, Introduction to Magnetic Materials, Wiley (2008).

[193] N. Ashcroft and N. Mermin, Solid state physics, Saunders College (1976).

[194] M. Z. Hasan and C. L. Kane, "Colloquium: Topological insulators," *Reviews of Modern Physics*, **82** (4): 3045–3067 (2010).

[195] K. v. Klitzing, G. Dorda and M. Pepper, "New Method for High-Accuracy Determination of the Fine-Structure Constant Based on Quantized Hall Resistance," *Phys. Rev. Lett.*, **45**: 494–497 (1980).

[196] M. Z. Hasan and C. L. Kane, "Topological Insulators," *Annual Review of Condensed Matter Physics*, **2** (1): 55–78 (2010).

[197] J. E. Moore, "The birth of topological insulators," *Nature*, **464** (7286): 194–198 (2010).

[198] C. L. Kane and E. J. Mele, "Z_2 Topological Order and the Quantum Spin Hall Effect," *Phys. Rev. Lett.*, **95**: 146802 (2005).

[199] J. E. Moore and L. Balents, "Topological invariants of time-reversal-invariant band structures," *Phys. Rev. B*, **75**: 121306 (2007).

[200] J. M. Fonseca, Algumas Contribuiç ões ao Estudo do Grafeno e dos Isolantes Topológicos , Ph.D. thesis, Universidade Federal de Viçosa (2012).

[201] R. Mong, Classi

cation and characterization of topological insulators and superconductors , Ph.D. thesis, University of California, Berkeley (2012).

[202] N. S. Virk, A Theoretical Investigation of Topological Insulator Nanostructures, Ph.D. thesis, École Polytechnique Fédérale de Lausanne (2016).

[203] B. A. Bernevig, T. L. Hughes and S.-C. Zhang, "Quantum spin Hall effect and topological phase transition in HgTe quantum wells," *Science*, **314** (5806): 1757–1761 (2006).

[204] M. König *et al.*, "Quantum spin hall insulator state in HgTe quantum wells," *Science*, **318** (5851): 766–770 (2007).

[205] A. Roth *et al.*, "Nonlocal transport in the quantum spin hall state," *Science*, **325** (5938): 294–297 (2009).

[206] X. L. Qi and S. C. Zhang, "The quantum spin Hall effect and topological insulators," *Physics Today*, **63** (1): 33–38 (2010).

[207] X. L. Qi and S. C. Zhang, "Topological insulators and superconductors," *Reviews of Modern Physics*, **83** (4) (2011).

[208] L. Fu, C. L. Kane and E. J. Mele, "Topological Insulators in Three Dimensions," *Phys. Rev. Lett.*, **98**: 106803 (2007).

[209] R. Roy, "Topological phases and the quantum spin Hall effect in three dimensions," *Phys. Rev. B*, **79**: 195322 (2009).

[210] D. Hsieh *et al.*, "A topological Dirac insulator in a quantum spin Hall phase," *Nature*, **452** (7190): 970–974 (2008).

[211] D. Hsieh *et al.*, "Observation of Unconventional Quantum Spin Textures in Topological Insulators," *Science*, **323** (5916): 919–922 (2009).

[212] Y. Xia *et al.*, "Observation of a large-gap topological-insulator class with a single Dirac cone on the surface," *Nature Physics*, **5** (6): 398–402 (2009).

[213] Y. L. Chen *et al.*, "Experimental realization of a three-dimensional topological insulator, Bi2Te3," *Science*, **325** (5937): 178–181 (2009).

[214] H. Zhang *et al.*, "Topological insulators in Bi2Se3, Bi2Te3 and Sb2Te3 with a single Dirac cone on the surface," *Nature Physics*, **5** (6): 438–442 (2009).

[215] A. H. Castro Neto *et al.*, "The electronic properties of graphene," *Rev. Mod. Phys.*, **81**: 109–162 (2009).

[216] U. Ebels, L. D. Buda, K. Ounadjela and P. E. Wigen, "Small Amplitude Dynamics of Nonhomogeneous Magnetization Distributions: The Excitation Spectrum of Stripe Domains," in "Spin Dynamics in Confined Magnetic Structures," (edited by Burkard Hillebrands and Kamel Ounadjela), pp. 167–217, Springer, Berlin (2002).

[217] O. A. Santos, Investigação do processo de spin pumping em bicamadas magníticas e filmes simples, Master's thesis, Universidade Federal de Pernambuco (2014).

[218] E. H. Hall, "On a New Action of the Magnet on Electric Currents," *American Journal of Mathematics*, **2** (3): 287 (1879).

[219] S. Maekawa, "Magnetism: A flood of spin current," *Nature Materials*, **8** (10): 777–778 (2009).

[220] G. Tatara and S. Mizukami, "Consistent microscopic analysis of spin pumping effects," *Physical Review B*, **96** (6): 1–23 (2017).

[221] Y. Tserkovnyak, A. Brataas and G. E. Bauer, "Spin pumping and magnetization dynamics in metallic multilayers," *Physical Review B*, **66** (22): 1–10 (2002).

[222] J. Yue *et al.*, "The influence of interface on spin pumping effect in Ni ₈₀ Fe ₂₀ âĂŁ/Tb bilayer," *AIP Advances*, **6** (5): 056120 (2016).

[223] M. Balinsky *et al.*, "Spin Pumping and the Inverse Spin-Hall Effect via Magnetostatic Surface Spin-Wave Modes in YttriumIron Garnet/Platinum Bilayers," *IEEE Magnetics Letters*, **6**: 0–3 (2015).

[224] S. Watanabe *et al.*, "Generation of megahertz-band spin currents using nonlinear spin pumping," *Scientific Reports*, **7** (1): 3–8 (2017).

[225] S. Maekawa *et al.*, "Spin Current: Experimental and Theoretical Aspects," *Journal of the Physical Society of Japan*, **82** (10): 102002 (2013).

[226] J. Sinova *et al.*, "Spin Hall effects," *Reviews of Modern Physics*, **87** (4): 1213–1260 (2015).

[227] A. Hoffmann, "Spin hall effects in metals," *IEEE Transactions on Magnetics*, **49** (10): 5172–5193 (2013).

[228] K. Ando *et al.*, "Inverse spin-Hall effect induced by spin pumping in metallic system," *Journal of Applied Physics*, **109** (10) (2011).

[229] K. Uchida *et al.*, "Observation of the spin Seebeck effect," *Nature*, **455** (7214): 778–781 (2008).

[230] S. Bosu *et al.*, "Spin Seebeck effect in thin films of the Heusler compound Co_2MnSi," *Phys. Rev. B*, **83**: 224401 (2011).

[231] C. Jaworski *et al.*, "Observation of the spin-Seebeck effect in a ferromagnetic semiconductor," *Nature materials*, **9** (11): 898 (2010).

[232] K. Uchida *et al.*, "Spin seebeck insulator," *Nature materials*, **9** (11): 894 (2010).

[233] D. Qu *et al.*, "Intrinsic spin Seebeck effect in Au/YIG," *Physical review letters*, **110** (6): 067206 (2013).

[234] J. Sinova, "Spin Seebeck effect: Thinks globally but acts locally," *Nature Materials*, **9** (11): 880–881 (2010).

[235] H. Adachi, K. I. Uchida, E. Saitoh and S. Maekawa, "Theory of the spin Seebeck effect," *Reports on Progress in Physics*, **76** (3) (2013).

[236] J. Zhang *et al.*, "Band structure engineering in (Bi1âĹŠxSbx)2Te3 ternary topological insulators," *Nature Communications*, **2**: 574 (2011).

[237] C. Z. Chang *et al.*, "High-precision realization of robust quantum anomalous Hall state in a hard ferromagnetic topological insulator," *Nature Materials*, **14** (5): 473–477 (2015).

[238] Z. Jiang *et al.*, "Structural and proximity-induced ferromagnetic properties of topological insulator-magnetic insulator heterostructures," *AIP Advances*, **6** (5) (2016).

[239] Y. Zhang *et al.*, "Crossover of the three-dimensional topological insulator Bi2Se3to the two-dimensional limit," *Nature Physics*, **6** (8): 584–588 (2010).

[240] M. Li *et al.*, "Dirac-electron-mediated magnetic proximity effect in topological insulator/magnetic insulator heterostructures," *Phys. Rev. B*, **96**: 201301 (2017).

[241] O. Mosendz *et al.*, "Quantifying Spin Hall Angles from Spin Pumping: Experiments and Theory," *Phys. Rev. Lett.*, **104**: 046601 (2010).

[242] A. Azevedo *et al.*, "Spin pumping and anisotropic magnetoresistance voltages in magnetic bilayers: Theory and experiment," *Phys. Rev. B*, **83**: 144402 (2011).

[243] A. Azevedo *et al.*, "Electrical detection of ferromagnetic resonance in single layers of permalloy: Evidence of magnonic charge pumping," *Phys. Rev. B*, **92**: 024402 (2015).

[244] J. C. Sánchez *et al.*, "Spin-to-charge conversion using Rashba coupling at the interface between non-magnetic materials," *Nature Communications*, **4**: 1–7 (2013).

[245] Y. Shiomi *et al.*, "Spin-electricity conversion induced by spin injection into topological insulators," *Physical Review Letters*, **113** (19): 7–11 (2014).

[246] S. Zhang and A. Fert, "Conversion between spin and charge currents with topological insulators," *Physical Review B*, **94** (18): 1–5 (2016).

[247] J. C. Rojas-Sánchez *et al.*, "Spin to Charge Conversion at Room Temperature by Spin Pumping into a New Type of Topological Insulator: α -Sn Films," *Physical Review Letters*, **116** (9): 1–6 (2016).

[248] K. Kondou *et al.*, "Fermi-level-dependent charge-to-spin current conversion by Dirac surface states of topological insulators," *Nature Physics*, **12** (11): 1027–1031 (2016).

[249] H. Geng *et al.*, "Theory of Inverse Edelstein Effect of the Surface States of A Topological Insulator," *Scientific Reports*, **7** (1): 1–7 (2017).

[250] K. Shen, G. Vignale and R. Raimondi, "Microscopic theory of the inverse Edelstein effect," *Physical Review Letters*, **112** (9): 1–5 (2014).

[251] G. E. Bauer, E. Saitoh and B. J. Van Wees, "Spin caloritronics," *Nature Materials*, **11** (5): 391–399 (2012).

[252] C. Hahn *et al.*, "Conduction of spin currents through insulating antiferromagnetic oxides," *Epl*, **108** (5) (2014).

[253] H. Wang, C. Du, P. C. Hammel and F. Yang, "Antiferromagnonic Spin Transport from $\mathrm{Y_3Fe_5}O_{12}$ into NiO," *Physical Review Letters*, **113** (9): 097202 (2014).

[254] J. Holanda *et al.*, "Spin Seebeck effect in the antiferromagnet nickel oxide at room temperature," *Applied Physics Letters*, **111** (17): 172405 (2017).

[255] J. Holanda *et al.*, "Longitudinal spin Seebeck effect in permalloy separated from the anomalous Nernst effect: Theory and experiment," *Physical Review B*, **95** (21): 1–8 (2017).

[256] T. Kikkawa *et al.*, "Separation of longitudinal spin Seebeck effect from anomalous Nernst effect: Determination of origin of transverse thermoelectric voltage in metal/insulator junctions," *Physical Review B - Condensed Matter and Materials Physics*, **88** (21) (2013).

[257] T. Taniguchi, "Phenomenological spin transport theory driven by anomalous nernst effect," *Journal of the Physical Society of Japan*, **85** (7): 1–8 (2016).

[258] A. D. Avery, M. R. Pufall and B. L. Zink, "Observation of the planar nernst effect in permalloy and Nickel thin films with in-plane thermal gradients," *Physical Review Letters*, **109** (19): 1–5 (2012).

[259] W. Zhang *et al.*, "Spin pumping and inverse Rashba-Edelstein effect in NiFe/Ag/Bi and NiFe/Ag/Sb," *Journal of Applied Physics*, **117** (17): 13–17 (2015).

[260] S. Sangiao *et al.*, "Control of the spin to charge conversion using the inverse Rashba-Edelstein effect," *Applied Physics Letters*, **106** (17): 3–7 (2015).

[261] M. Isasa *et al.*, "Origin of inverse Rashba-Edelstein effect detected at the Cu/Bi interface using lateral spin valves," *Physical Review B*, **93** (1): 23–27 (2016).

[262] P. Deorani and H. Yang, "Role of spin mixing conductance in spin pumping: Enhancement of spin pumping efficiency in Ta/Cu/Py structures," *Applied Physics Letters*, **103** (23): 0–4 (2013).

[263] A. A. Baker *et al.*, "Spin pumping in Ferromagnet-Topological Insulator-Ferromagnet Heterostructures," *Scientific Reports*, **5**: 1–5 (2015).

[264] B. A. Bassett, S. Liberati, C. Molina-París and M. Visser, "Geometrodynamics of variable-speed-of-light cosmologies," *Phys. Rev. D*, **62**: 103518 (2000).

[265] K. Y. Bliokh, A. Niv, V. Kleiner and E. Hasman, "Geometrodynamics of spinning light," *Nature Photonics*, **2** (12): 748–753 (2008).

[266] R. Moessner and A. P. Ramirez, "Geometrical frustration," *Physics Today*, **59** (2): 24–29 (2006).

[267] L. Balents, "Spin liquids in frustrated magnets," *Nature*, **464** (7286): 199–208 (2010).

[268] R. C. Silva *et al.*, "Thermodynamics of elementary excitations in artificial magnetic square ice," *New Journal of Physics*, **14**: 015008 (2012).

[269] M. J. Harris *et al.*, "Geometrical frustration in the ferromagnetic pyrochlore Ho2Ti2O7," *Physical Review Letters*, **79** (13): 2554–2557 (1997).

[270] A. P. Ramirez *et al.*, "Zero-point entropy in 'spin ice'," *Nature*, **399** (6734): 333–335 (1999).

[271] S. T. Bramwell and M. J. P. Gingras, "Spin Ice State in Frustrated Magnetic Pyrochlore Materials," *Science*, **294** (5546): 1495–1501 (2001).

[272] S. T. Bramwell *et al.*, "Spin Correlations in $\mathrm{Ho_2Ti_2}O_7$: A Dipolar Spin Ice System," *Phys. Rev. Lett.*, **87**: 047205 (2001).

[273] R. F. Wang *et al.*, "Artificial 'spin ice' in a geometrically frustrated lattice of nanoscale ferromagnetic islands," *Nature*, **439** (7074): 303–306 (2006).

[274] C. Castelnovo, R. Moessner and S. L. Sondhi, "Magnetic monopoles in spin ice," *Nature*, **451** (7174): 42–45 (2008).

[275] A. P. Ramirez, "Strongly Geometrically Frustrated Magnets," *Annual Review of Materials Science*, **24** (1): 453–480 (1994).

[276] C. Nisoli, R. Moessner and P. Schiffer, "Colloquium: Artificial spin ice: Designing and imaging magnetic frustration," *Reviews of Modern Physics*, **85** (4): 1473–1490 (2013).

[277] P. G. Wolynes, "Symmetry and the energy landscapes of biomolecules." *Proceedings of the National Academy of Sciences of the United States of America*, **93** (25): 14249–14255 (1996).

[278] H. M. Harreis, C. N. Likos and H. Löwen, "Azimuthal frustration and bundling in columnar DNA aggregates," *Biophysical Journal*, **84** (6): 3607–3623 (2003).

[279] S. Krishna, S. Semsey and M. H. Jensen, "Frustrated bistability as a means to engineer oscillations in biological systems," *Physical Biology*, **6** (3) (2009).

[280] M. W. Long, "Topological frustration can lead to superconductivity," *Journal of Physics: Condensed Matter*, **3** (33): 6387 (1991).

[281] M. Hanawa *et al.*, "Superconductivity at 1 K in $\mathrm{Cd_2Re_2}O_7$," *Phys. Rev. Lett.*, **87**: 187001 (2001).

[282] T. Yildirim, "Origin of the 150-K Anomaly in LaFeAsO: Competing Antiferromagnetic Interactions, Frustration, and a Structural Phase Transition," *Phys. Rev. Lett.*, **101**: 057010 (2008).

[283] Y. Yamamoto, H. Tanaka and T. Kawai, "The Control of Cluster-Glass Transition Temperature in Spinel-Type ZnFe 2 O 4-Îť Thin Film," *Japanese Journal of Applied Physics*, **40** (6A): L545 (2001).

[284] G. H. Wannier, "Antiferromagnetism. The Triangular Ising Net," *Phys. Rev.*, **79**: 357–364 (1950).

[285] X. Ke *et al.*, "Tuning magnetic frustration of nanomagnets in triangular-lattice geometry," *Applied Physics Letters*, **93** (25): 252504 (2008).

[286] Y. Li *et al.*, "Geometry effect on the magnetic ordering of geometrically frustrated rectangular and triangular magnets," *Physics Letters A*, **375** (13): 1548 – 1551 (2011).

[287] P. Dirac, "Quantised singularities in the electromagnetic field," *Proceedings of the Royal Society of London A: Mathematical, Physical and Engineering Sciences*, **133** (821): 60–72 (1931).

[288] Y. Nambu, "Strings, monopoles, and gauge fields," *Physical Review D*, **10** (12): 4262–4268 (1974).

[289] L. A. Mól *et al.*, "Magnetic monopole and string excitations in two-dimensional spin ice," *Journal of Applied Physics*, **106** (6): 6–11 (2009).

[290] F. S. Nascimento, L. A. Mól, W. A. Moura-Melo and A. R. Pereira, "From confinement to deconfinement of magnetic monopoles in artificial rectangular spin ices," *New Journal of Physics*, **14** (2012).

[291] S. T. Bramwell *et al.*, "Measurement of the charge and current of magnetic monopoles in spin ice," *Nature*, **461** (7266): 956–959 (2009).

[292] S. Ladak *et al.*, "Direct observation of magnetic monopole defects in an artificial spin-ice system," *Nature Physics*, **6** (5): 359–363 (2010).

[293] H. D. Zhou *et al.*, "High pressure route to generate magnetic monopole dimers in spin ice," *Nature Communications*, **2** (1): 6–10 (2011).

[294] S. J. Blundell, "Monopoles, Magnetricity, and the Stray Field from Spin Ice," *Phys. Rev. Lett.*, **108**: 147601 (2012).

[295] W. R. Branford *et al.*, "Emerging Chirality in Artificial Spin Ice," *Science*, **335** (6076): 1597–1600 (2012).

[296] R. P. Loreto *et al.*, "Emergence and mobility of monopoles in a unidirectional arrangement of magnetic nanoislands," *Nanotechnology*, **26** (29) (2015).

[297] W. F. Giauque and M. F. Ashley, "Molecular Rotation in Ice at 10K. Free Energy of Formation and Entropy of Water," *Phys. Rev.*, **43**: 81–82 (1933).

[298] W. F. Giauque and J. W. Stout, "The Entropy of Water and the Third Law of Thermodynamics. The Heat Capacity of Ice from 15 to 273K," *Journal of the American Chemical Society*, **58** (7): 1144–1150 (1936).

[299] L. Pauling, "The Structure and Entropy of Ice and of Other Crystals with Some Randomness of Atomic Arrangement," *Journal of the American Chemical Society*, **57** (12): 2680–2684 (1935).

[300] J. D. Bernal and R. H. Fowler, "A theory of water and ionic solution with particular reference to hydrogen and hydroxyl ions," *The Journal of Chemical Physics*, **1** (8): 515–548 (1933).

[301] F. S. Nascimento, Estudo das Propriedades Térmicas e Magnéticas de Gelos de Spin Retangulares, Ph.D. thesis, Universidade Federal de Viçosa (2014).

[302] O. Benton, O. Sikora and N. Shannon, "Classical and quantum theories of proton disorder in hexagonal water ice," *Physical Review B*, **93** (12) (2016).

[303] S. T. Bramwell and M. J. Harris, "Frustration in Ising-type spin models on the pyrochlore lattice," *Journal of Physics: Condensed Matter*, **10** (14): L215 (1998).

[304] K. Matsuhira, Y. Hinatsu, K. Tenya and T. Sakakibara, "Low temperature magnetic properties of frustrated pyrochlore ferromagnets Ho2Sn2O7 and Low temperature magnetic properties of frustrated pyrochlore ferromagnets Ho 2 Sn 2 O 7 and Ho 2 Ti 2 O 7," *Journal of Physics: Condensed Matter*, **12**: L649 – L656 (2000).

[305] H. Kadowaki, Y. Ishii, K. Matsuhira and Y. Hinatsu, "Neutron scattering study of dipolar spin ice $Ho_2Sn_2O_7$: Frustrated pyrochlore magnet," *Phys. Rev. B*, **65**: 144421 (2002).

[306] G. W. Chern, S. Maiti, R. M. Fernandes and P. Wölfle, "Electronic transport in the coulomb phase of the pyrochlore spin ice," *Physical Review Letters*, **110** (14): 1–5 (2013).

[307] M. J. P. Gingras, "Observing monopoles in a magnetic analog of ice," *Science*, **326** (5951): 375–376 (2009).

[308] R. Siddharthan *et al.*, "Ising pyrochlore magnets: Low-temperature properties, âĂIJice rules,âĂİ and beyond," *Physical Review Letters*, **83** (9): 1854–1857 (1999).

[309] R. da Costa Silva, Contribuições ao Estudo de Sistemas Magnéticos Frustrados: Efeitos Termodinâmicos e de Defeitos Estruturais em Gelos de Spin Artificiais, Ph.D. thesis, Universidade Federal de Viçosa (2014).

[310] J. Li *et al.*, "Comparing artificial frustrated magnets by tuning the symmetry of nanoscale permalloy arrays," *Physical Review B - Condensed Matter and Materials Physics*, **81** (9): 1–4 (2010).

[311] E. Mengotti *et al.*, "Building blocks of an artificial kagome spin ice: Photoemission electron microscopy of arrays of ferromagnetic islands," *Phys. Rev. B*, **78**: 144402 (2008).

[312] E. Mengotti *et al.*, "Real-space observation of emergent magnetic monopoles and associated Dirac strings in artificial kagome spin ice," *Nature Physics*, **7** (1): 68–74 (2011).

[313] L. A. S. Mól, A. R. Pereira and W. A. Moura-Melo, "Extending spin ice concepts to another geometry: The artificial triangular spin ice," *Phys. Rev. B*, **85**: 184410 (2012).

[314] M. J. Morrison, T. R. Nelson and C. Nisoli, "Unhappy vertices in artificial spin ice: New degeneracies from vertex frustration," *New Journal of Physics*, **15** (2013).

[315] G. W. Chern, M. J. Morrison and C. Nisoli, "Degeneracy and criticality from emergent frustration in artificial spin ice," *Physical Review Letters*, **111** (17): 1–5 (2013).

[316] J. P. Morgan, A. Stein, S. Langridge and C. H. Marrows, "Thermal ground-state ordering and elementary excitations in artificial magnetic square ice," *Nature Physics*, **7** (1): 75–79 (2011).

[317] C. Nisoli *et al.*, "Effective Temperature in an Interacting Vertex System: Theory and Experiment on Artificial Spin Ice," *Phys. Rev. Lett.*, **105**: 047205 (2010).

[318] G. Möller and R. Moessner, "Artificial square ice and related dipolar nanoarrays," *Physical Review Letters*, **96** (23): 1–4 (2006).

[319] H. Bethge and M. Klaua, "Photo-electron emission microscopy of work function changes," *Ultramicroscopy*, **11** (2): 207 – 214 (1983).

[320] B. P. Tonner and G. R. Harp, "Photoelectron microscopy with synchrotron radiation," *Review of Scientific Instruments*, **59** (6): 853–858 (1988).

[321] J. Stohr *et al.*, "Element-Specific Magnetic Microscopy with Circularly Polarized X-Rays," *Science*, **259** (5095): 658–661 (1993).

[322] S. Anders *et al.*, "Photoemission electron microscope for the study of magnetic materials," *Review of Scientific Instruments*, **70** (10): 3973–3981 (1999).

[323] A. Scholl *et al.*, "X-ray photoemission electron microscopy, a tool for the investigation of complex magnetic structures (invited)," *Review of Scientific Instruments*, **73** (3): 1362–1366 (2002).

[324] L. J. Heyderman, F. Nolting and C. Quitmann, "X-ray photoemission electron microscopy investigation of magnetic thin film antidot arrays," *Applied Physics Letters*, **83** (9): 1797–1799 (2003).

[325] D.-H. Wei *et al.*, "Photoelectron Microscopy Projects at SRRC," *Surface Review and Letters*, **10** (04): 617–624 (2003).

[326] Jun Feng and Andreas Scholl, "Photoemission ElectronMicroscopy (PEEM)," in "Science of Microscopy," (edited by Peter Hawkes and John C.H. Spence), volume 1, p. 657, Springer, New York (2007).

[327] http://xraysweb.lbl.gov/peem2/webpage/Project/TutorialPEEM.shtml, accessed: March, 1^{st}, 2018.

[328] ssrl.slac.stanford.edu/stohr/xmcd.htm, accessed: March, 1^{st}, 2018.

[329] G. Van Der Laan, "Applications of soft x-ray magnetic dichroism," in "Journal of Physics: Conference Series," volume 430 (2013).

[330] P. Fischer, "Magnetic imaging with polarized soft x-rays," in "Magnetism and Synchrotron Radiation: Towards the Fourth Generation Light Sources," (edited by E. Beaurepaire, H. Bulou, L. Joly and F. Scheurer), volume 1, p. 155, Springer (2012).

[331] C. T. Chen, F. Sette, Y. Ma and S. Modesti, "Soft-x-ray magnetic circular dichroism at the L2,3 edges of nickel," *Physical Review B*, **42** (11): 7262–7265 (1990).

[332] Stohr J., "Exploring the microscopic origin of magnetic anisotropies with X-ray magnetic circular dichroism (XMCD) spectroscopy - Condens. Matter," *Journal of Magnetism and Magnetic Materials*, **200** (1): 28 (1999).

[333] V. Y. Irkhin and M. I. Katsnelson, "Sum rules for X-ray magnetic circular dichroism spectra in strongly correlated ferromagnets," *Eur. Phys. Journal B*, **4**: 1–4 (2005).

[334] C. R. Brundle, C. A. Evans Jr and S. Wilson, Encyclopedia of Materials Characterization, Butterworth-Heinemann (Elsevier), Boston (1992).

[335] J. Zak, E. R. Moog, C. Liu and S. D. Bader, "Fundamental magneto-optics," *Journal of Applied Physics*, **68** (8): 4203–4207 (1990).

[336] T. Haider, "A Review of Magneto-Optic Effects and Its Application," *International Journal of Electromagnetics and Applications*, **7** (1): 17–24 (2017).

[337] U. Tiwari, R. Ghosh and P. Sen, "Theory of magneto-optic Kerr effects," *Physical Review B*, **49** (3): 2159–2162 (1994).

[338] Z. Q. Qiu and S. D. Bader, "Surface magneto-optic Kerr effect (SMOKE)," *Journal of Magnetism and Magnetic Materials*, **200** (1-3): 664–678 (1999).

[339] L. A. da Silva Mól, Transições de fase em modelos magnéticos bi-dimensionais com interações dipolares, Ph.D. thesis, Universidade Federal de Viçosa (2009).

[340] A. Farhan *et al.*, "Thermodynamics of emergent magnetic charge screening in artificial spin ice," *Nature Communications*, **7**: 1–6 (2016).

[341] Y. Perrin, B. Canals and N. Rougemaille, "Extensive degeneracy, Coulomb phase and magnetic monopoles in artificial square ice," *Nature*, **540** (7633): 410–413 (2016).

[342] J. B. S. Mendes *et al.*, "Dirac-surface-state-dominated spin to charge current conversion in the topological insulator $(Bi_{0.22}Sb_{0.78})_2Te_3$ films at room temperature," *Phys. Rev. B*, **96**: 180415 (2017).

[343] J. B. S. Mendes *et al.*, "Spin-Current to Charge-Current Conversion and Magnetoresistance in a Hybrid Structure of Graphene and Yttrium Iron Garnet," *Phys. Rev. Lett.*, **115**: 226601 (2015).

[344] O. Alves-Santos *et al.*, "Giant spin-charge conversion driven by nanoscopic particles of Ag in Pt," *Phys. Rev. B*, **96**: 060408 (2017).